nature neuroscience

Article

https://doi.org/10.1038/s41593-026-02515-6

The identity gene *Fezf2* is repurposed postnatally to specify inhibitory input in an activity-dependent manner

Received: 30 November 2023

Accepted: 13 October 2026

Published online: 26 November 2026

Check for updates

Tim Kroon[1,2], Stella Sanalidou[1,2], Patricia Maeso[1,2], Han Yang[1,2], Teresa Garces[1,2], Noorya Ahmed[1,2], Rafael Alis[3,4], Yaiza Dominguez-Canterla[3,4], Sergio Niñerola[5], Keagan Dunville[1,2], Beatriz del Blanco[5], Angel Barco[5], Nuria Flames[3,4] & Beatriz Rico[1,2]

The development and function of cortical circuits require an appropriate balance of excitation and inhibition. Pyramidal cells, the principal excitatory cells in the cerebral cortex, recruit inhibitory synapses in proportion to their activity. How each pyramidal cell subtype achieves the cell-type-specific levels of inhibition it requires is unknown. Here we show in mice that a neuronal identity gene is repurposed postnatally to regulate inhibitory connectivity. *Fezf2*, which encodes a transcription factor that establishes the identity of extratelencephalic pyramidal cells in layer 5 during embryonic development, is regulated by activity after birth only in those neurons. Activity-dependent FEZF2 controls the number of inhibitory synapses formed by parvalbumin-expressing interneurons through regulation of the cell-surface protein Cadherin-22. Our findings reveal that a gene specifying neuronal subtype identity is redeployed to control how activity refines wiring, giving activity-dependent circuit development its cell-type specificity.

The function of the cerebral cortex relies on the precise interplay between two neuronal populations—excitatory glutamatergic principal or pyramidal cells and inhibitory γ-aminobutyric acid (GABAergic)-expressing interneurons. The connectivity motifs established between these two neuronal populations are highly specialized and crucial for the function of cortical circuits. For example, different types of inhibitory interneurons have been shown to target specific subcellular compartments of principal cells, enhancing the computational power of cortical circuitry[1,2].

A remarkable diversity of molecular programs supports the exquisite variety of cortical inhibitory connectivity that emerges during development. The prevailing view conveys that synaptic development has the following two components: (1) a genetically determined process sustained by specific molecular codes and (2) an activity-dependent mechanism that fine-tunes circuitry[3–5]. Several cell-surface molecule complexes are required for the development of GABAergic synapses, including Neuroligin-2, NRG1/NRG3-ErbB4 and neurexin2αβ-IgSF21 (refs. 6–9). Moreover, the specific cellular and subcellular targeting of pyramidal cells by interneurons is also regulated by cell-surface molecules[7]. The development of inhibitory synapses in the cerebral cortex unfolds over a protracted period of postnatal development[10–12] and activity sculpts the inhibitory cortical circuitry until it reaches the mature state[10,13,14].

In the adult brain, activity-dependent mechanisms are fundamental to maintaining reliable coding during fluctuating activity patterns, such as those caused by sensory experience[15]. Pyramidal

[1]Centre for Developmental Neurobiology, Institute of Psychiatry, Psychology and Neuroscience, King's College London, London, UK. [2]MRC Centre for Neurodevelopmental Disorders, King's College London, London, UK. [3]Developmental Neurobiology Unit, Instituto de Biomedicina de Valencia IBV-CSIC, Valencia, Spain. [4]Valencia Biomedical Research Foundation, Centro de Investigación Príncipe Felipe (CIPF)—Associated Unit to the Instituto de Biomedicina de Valencia (IBV), Valencia, Spain. [5]Instituto de Neurociencias, Universidad Miguel Hernández—Consejo Superior de Investigaciones Científicas, Sant Joan d'Alacant, Spain. e-mail: beatriz.rico@kcl.ac.uk

https://doi.org/10.1038/s41593-026-02515-6

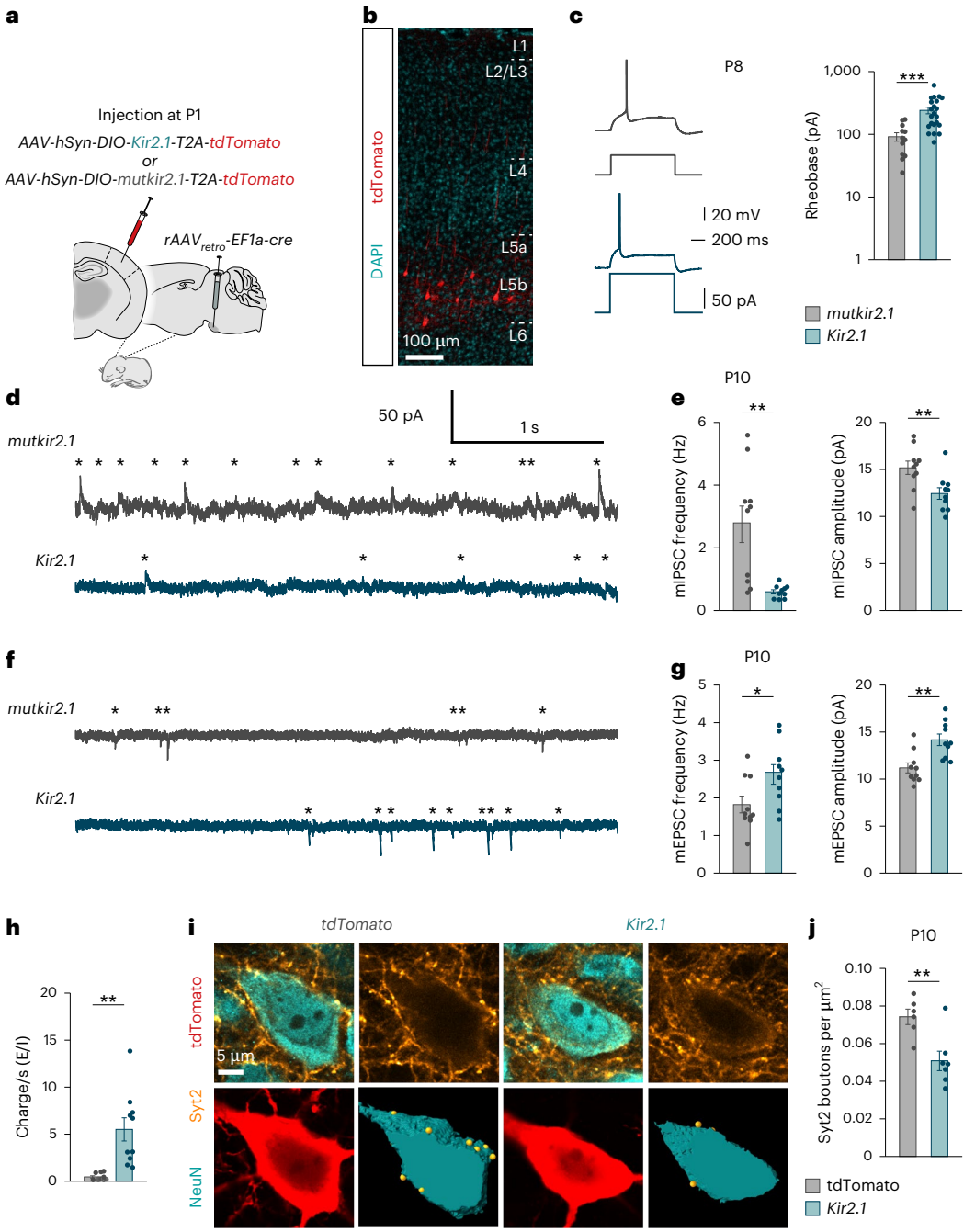

Fig. 1 | Decreased neuronal activity reduces inhibitory inputs during development. a, Experimental design for decreasing activity by expressing Kir2.1 specifically in L5 ET cells. **b**, Expression of tdTomato in AAV-infected cells in deep L5, consistent across 367 replicates. Scale bar = 100 µm. **c**, Electrophysiological measurement of excitability of mutKir2.1-expressing versus Kir2.1-expressing L5 ET cells. Left, example traces of the first current injection to elicit an action potential. Right, quantification of rheobase (mutKir2.1, $n = 12$ cells from four mice; Kir2.1, $n = 22$ cells from seven mice, two-tailed Welch's t-test, $^{***}P = 0.0008$). **d**, Example traces of mIPSCs recorded from mutKir2.1-expressing and Kir2.1-expressing cells. Asterisks indicate the onset of mIPSC events. **e**, Quantification of mIPSC frequency (mutKir2.1, $n = 10$ cells from five mice; Kir2.1, $n = 10$ cells from three mice, two-tailed Welch's t-test, $^{**}P = 0.0048$) and amplitude (mutKir2.1, $n = 10$ cells from 5 mice; Kir2.1, $n = 10$ cells from 3 mice, two-tailed Student's t-test, $^{**}P = 0.0097$). **f**, Example traces of mEPSCs recorded from mutKir2.1-expressing and Kir2.1-expressing cells. Asterisks indicate the onset of mEPSC events. **g**, Quantification of mEPSC frequency (mutKir2.1, $n = 10$ cells from five mice; Kir2.1, $n = 10$ cells from three mice, two-tailed Student's t-test, $^{*}P = 0.0317$) and amplitude (mutKir2.1, $n = 10$ cells from five mice; Kir2.1, $n = 10$ cells from three mice, two-tailed Student's t-test, $^{**}P = 0.0018$). **h**, Quantification of the ratio of the charge per second of mEPSCs to mIPSCs (mutKir2.1, $n = 10$ cells from five mice; Kir2.1, $n = 10$ cells from three mice, two-tailed Welch's t-test, $^{**}P = 0.0027$). **i**, Single-plane confocal images showing presynaptic Syt2 puncta (yellow), NeuN (cyan) and tdTomato (red). Bottom-right, three-dimensional Imaris reconstruction of the soma and Syt2 puncta. Scale bar = 5 µm. **j**, Quantification of the density of Syt2 puncta onto the soma (tdTomato, $n = 6$ mice; Kir2.1, $n = 7$ mice, two-tailed Student's t-test, $^{**}P = 0.0057$). Data are mean ± s.e.m. See Supplementary Table 2.

neurons also regulate the inhibition they receive through homeostatic mechanisms[3,16–18]. Synaptic and cell-intrinsic changes underlying homeostatic plasticity are mediated through the activity-dependent expression of immediate early genes (IEGs). Cortical inhibitory synapses onto pyramidal cells undergo a steady increase in number during the first month of development[11,12], probably matching the progressive surge in excitatory inputs and activity of pyramidal cells[19,20]. Consistent with this, in vitro experiments revealed that the formation of inhibitory

synapses onto excitatory neurons is regulated by activity[10,21], and in the hippocampus requires *Npas4*, an IEG[21]. In adults, these transcription factors have been shown to promote the subsequent expression of late response genes (LRGs), which often encode secreted molecules or proteins with synaptic localization[22]. However, despite the relevance of inhibitory synapses and activity in the maturation of cortical circuitry, the molecular programs used by pyramidal cells to respond to temporally specific and cell-type-specific activity patterns during development remain unknown.

Here we address this question in layer 5 (L5) extratelencephalic (ET) pyramidal cells, the most excitable cortical pyramidal neurons[23–25], which receive remarkably more inhibitory inputs from parvalbumin-expressing (PV^+) basket cells than other pyramidal cells from early postnatal development[26]. By combining the manipulation of neuronal activity with ribosome-associated mRNA profiling, we find that *Fezf2*, the selector gene that specifies L5 ET identity in the embryo[27–30], is regulated by neuronal activity postnatally in these same neurons, but not in other pyramidal cell types. Activity-dependent changes in *Fezf2* expression determine the density of PV^+ inhibitory synapses received by L5 ET pyramidal cells, acting through the cell adhesion molecule Cadherin-22 (*Cdh22*), which we identify as a downstream effector. Our findings reveal a gene that first establishes a neuron's subtype identity and is repurposed after birth to determine how activity affects its inhibitory input, providing cell-type specificity to the activity-dependent assembly of cortical circuits.

Results

Neuronal activity regulates the development of inhibitory inputs onto pyramidal cells

L5 ET pyramidal cells receive a high density of perisomatic inhibition that increases steadily during the first month of postnatal life in mice[26]. To investigate whether activity regulates the formation of PV^+ perisomatic inhibitory synapses onto these neurons, we reduced the excitability of L5 ET pyramidal cells during early postnatal development by expressing the inwardly rectifying potassium channel Kir2.1 (ref. 31). We used an intersectional strategy to label L5 ET pyramidal cells in the primary somatosensory cortex (S1). In brief, we simultaneously injected a retrograde adeno-associated virus (AAV) expressing Cre recombinase ($rAAV_{retro}$-*cre*) into the pontine nuclei of postnatal day (P) 1 wild-type mice and a Cre-dependent AAV into S1 ipsilateral to the pons injection that expressed tdTomato and Kir2.1 or, in control experiments, a mutated version of Kir2.1 encoding a nonconducting channel (mutKir2.1 (ref. 17); Fig. 1a,b). We used this approach in all subsequent experiments to label L5 ET neurons unless stated otherwise.

To confirm that Kir2.1 expression lowers the excitability of L5 ET cells before the initial surge of inhibitory synapse formation around P10 (ref. 11), we prepared acute slices from mice at P8 expressing Kir2.1 or mutKir2.1. We then performed electrophysiological recordings of infected L5 ET pyramidal cells. Compared with mutKir2.1-expressing cells or uninfected cells, Kir2.1-expressing cells showed a hyperpolarized membrane potential and decreased input resistance, leading to a marked increase in rheobase that denoted a decrease in excitability (Fig. 1c and Extended Data Fig. 1a,b).

To establish whether the observed reduction in excitability led to a functional change in inhibitory inputs, we measured miniature inhibitory postsynaptic currents (mIPSCs). We found a reduction in the frequency and amplitude of mIPSCs of 78% and 18%, respectively, in Kir2.1-expressing L5 ET pyramidal cells compared with mutKir2.1-expressing L5 ET pyramidal cells at P10 (Fig. 1d,e). In addition, we observed an increased frequency (+44%) and amplitude (+27%) of miniature excitatory postsynaptic currents (mEPSCs) in the same cells (Fig. 1f,g). Thus, the ratio of the charge per second of excitatory to inhibitory miniature postsynaptic currents (mPSCs) was increased (Fig. 1h). Control experiments revealed that the reduction in mIPSCs in Kir2.1-expressing cells was not solely due to a network effect, as expression of Kir2.1 reduces the frequency and amplitude of mIPSCs compared with neighboring uninfected cells (Extended Data Fig. 1c,d). As a further control to ensure that this phenotype is not only due to the viral infection, we also compared mutKir2.1-expressing cells with neighboring uninfected cells and did not find a reduction in mIPSC frequency or amplitude (Extended Data Fig. 1e–h). Therefore, we conclude that the phenotype we see is due specifically to the action of Kir2.1 and is at least in part cell autonomous.

We then asked whether the decrease in inhibition was due to a reduction in the number of PV^+ presynaptic inputs, the primary source of perisomatic inhibition of L5 ET neurons[26,32,33]. To this end, we labeled control and Kir2.1-expressing L5 ET cells with tdTomato and quantified the density of perisomatic PV^+ boutons using the presynaptic marker synaptotagmin-2 (Syt2), which is specifically expressed in PV^+ basket cells[34]. We observed a reduction of 32% in the density of $Syt2^+$ boutons contacting the soma of L5 ET neurons expressing Kir2.1 compared with control neurons at P10 (Fig. 1i,j). Altogether, our results demonstrate that neuronal activity during development regulates the number of PV^+ basket-cell inputs that L5 ET pyramidal cells receive and changes the balance of excitatory and inhibitory input.

Fezf2 is regulated by neuronal activity in a cell-type-specific manner

To identify the activity-dependent molecular mechanisms regulating the development of PV^+ perisomatic inhibition onto L5 ET pyramidal neurons, we analyzed changes in the translatome of L5 ET neurons following the modulation of their activity during postnatal development. To this end, we used viral translating ribosome affinity purification (vTRAP)[35] to isolate ribosome-associated mRNA from pontine-projecting ET neurons expressing Kir2.1 or mutKir2.1. In brief, we generated Cre-dependent AAVs expressing a hemagglutinin (HA)-tagged ribosomal protein (RPL10A) and either Kir2.1 (Kir2.1-vTRAP) or mutKir2.1 (mutKir2.1-vTRAP; Extended Data Fig. 2a). To verify that Kir2.1-vTRAP decreases the excitability of L5 ET cells, we injected Kir2.1-vTRAP and mutKir2.1-vTRAP AAVs into $Rbp4^{cre/+}$ mice[36], in which Cre is expressed in most L5 pyramidal cells (Extended Data Fig. 2b). We then assessed excitability using electrophysiology, and filled recorded cells with neurobiotin to verify post hoc that they expressed the corresponding virus using immunohistochemistry against the HA-tag (Extended Data Fig. 2c). As expected, the excitability of cells expressing Kir2.1-vTRAP was decreased, as was the density of PV^+ basket-cell inputs they received, compared with neurons expressing mutKir2.1-vTRAP (Extended Data Fig. 2d–h).

To identify activity-dependent transcriptional programs, we isolated ribosome-associated mRNAs from L5 ET pyramidal cells expressing the Kir2.1-vTRAP or mutKir2.1-vTRAP at P10 and performed RNA sequencing (RNA-seq; Fig. 2a and Extended Data Fig. 3). We identified 673 differentially expressed genes (DEGs) between mutKir2.1-expressing and Kir2.1-expressing ET neurons (Fig. 2b, Supplementary Table 1 and Extended Data Fig. 3). Gene Ontology (GO) analysis of DEGs revealed enrichment in synaptic processes (Extended Data Fig. 3d). We focused on transcription factors and genes directly involved in synaptic assembly and synaptic maintenance by selecting specific PANTHER GO terms (Methods). We then ranked the selected genes using the following three criteria: (1) fold-change (FC) differential expression between Kir2.1-expressing and mutKir2.1-expressing neurons; (2) gene expression level; and (3) enrichment in ET cells compared with intratelencephalic (IT) cells (Fig. 2c; see Methods for details). Top-ranking genes from this analysis include those encoding several cell-surface adhesion molecules and the zinc-finger transcription factor *Fezf2*, most of which were downregulated in Kir2.1-expressing cells, as assessed by single-molecule RNA in situ hybridization (single-molecule fluorescence in situ hybridization (smFISH)), compared with control (*Cdh22* = −44%, *Cntn6* = −41%, *Fezf2* = −32%; Fig. 2c–f). In contrast, *Igsf21* expression did not change

https://doi.org/10.1038/s41593-026-02515-6

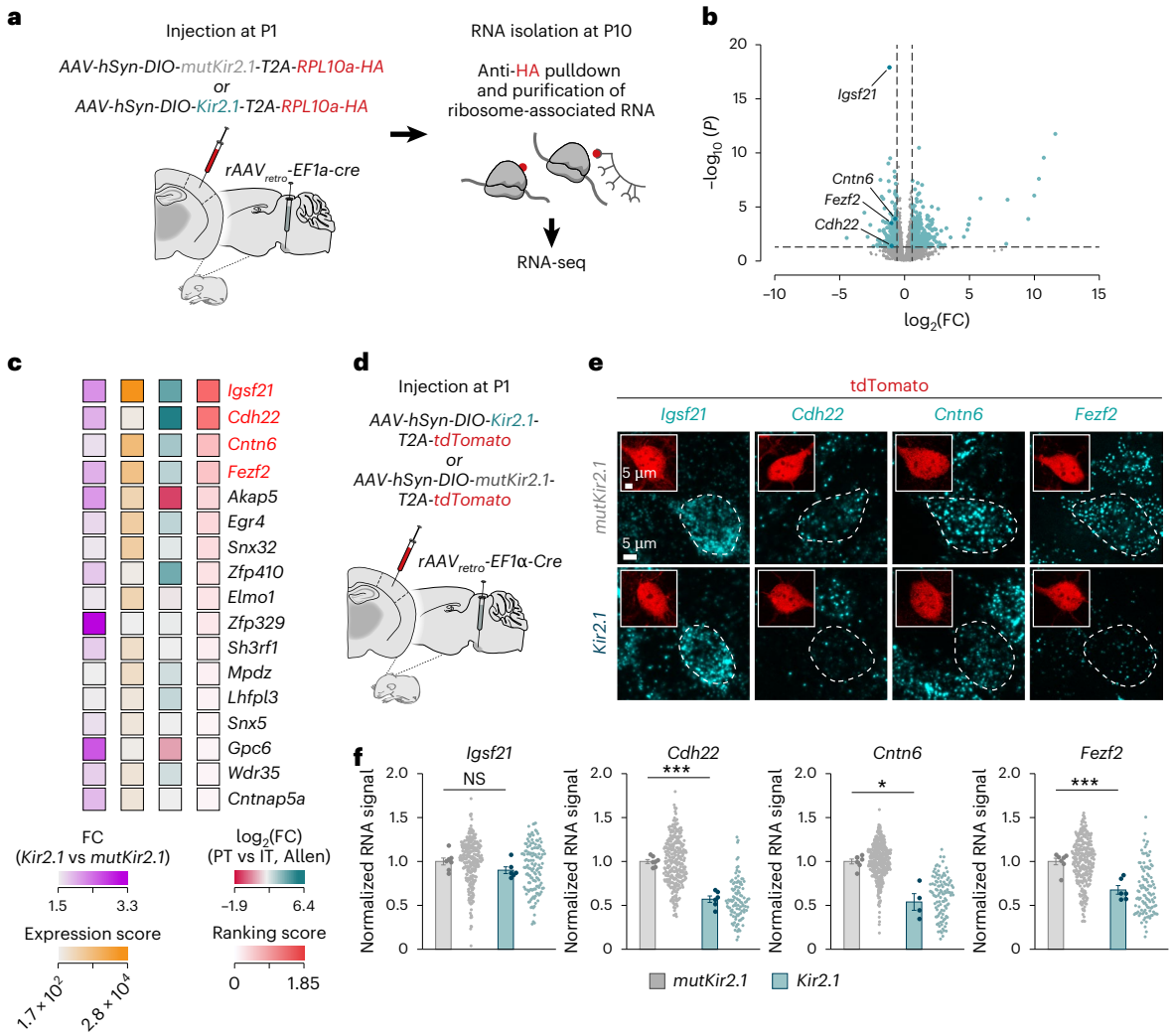

Fig. 2 | Transcriptional programs regulated by activity in L5 ET cells. **a**, Experimental design for the profiling of ribosome-associated mRNA from L5 ET cells. **b**, Volcano plot displaying significantly differentially expressed ribosome-associated RNAs (teal) in L5 ET cells expressing Kir2.1 compared with mutKir2.1 controls. Each dot represents one gene. Criteria—FC > 1.5, adjusted *P* (FDR, two sided) < 0.05. **c**, Heatmaps showing gene selection criteria. Top genes are labeled in red. **d**, Experimental design for decreasing activity by expressing Kir2.1 in L5 ET cells. **e**, Confocal images showing target gene by single-molecule RNA expression (cyan) in Kir2.1-expressing and mutKir2.1-expressing L5 ET cells (tdTomato, red). Dotted lines indicate the outlines of somata, drawn from the tdTomato signal. Scale bars = 5 µm. **f**, Quantification of RNA signal in Kir2.1-expressing ET cells compared with controls for *Igsf21* (mutKir2.1, $n = 7$ mice; Kir2.1, $n = 6$ mice, two-tailed Student's *t*-test, $P = 0.10$), *Cdh22* (mutKir2.1, $n = 7$ mice; Kir2.1, $n = 6$ mice, two-tailed Student's *t*-test, $^{***}P < 0.0001$), *Cntn6* (mutKir2.1, $n = 7$ mice; Kir2.1, $n = 4$ mice, two-tailed Welch's *t*-test, $^{*}P = 0.0129$) and *Fezf2* (mutKir2.1, $n = 7$ mice; Kir2.1, $n = 6$ mice, two-tailed Student's *t*-test, $^{***}P = 0.0002$). RNA levels are normalized to the mean of the control group. The dotted line indicates the soma outline, drawn from the tdTomato signal. Data are mean ± s.e.m. See Supplementary Table 2. NS, not significant; FDR, false discovery rate.

in these experiments, suggesting that this gene may be a false positive in our screen or that activity regulates its translation rather than its transcription. *Fezf2* is a selector gene that is enriched in L5 ET neurons compared with other pyramidal cells during development and is well known for its involvement in the early specification of L5 ET pyramidal cells[27–30]. Therefore, we were intrigued by the observation that the expression of *Fezf2* might be controlled in an activity-dependent manner in the postnatal cortex.

To confirm these observations, we transiently increased the excitability of L5 ET neurons using a chemogenetic approach based on Designer Receptors Exclusively Activated by Designer Drugs (DREADDs). In brief, we injected *rAAV$_{retro}$-cre* in the pons and AAVs encoding excitatory DREADDs (hM3Dq) in the S1 of P1 mice. A single injection of clozapine *N*-oxide (CNO) at P8 induced the expression of c-Fos, specifically in hM3Dq-expressing neurons (Extended Data Fig. 4). We then injected CNO twice daily between P8 and P10 and examined the expression of *Fezf2* at P10 (Fig. 3a). We found that the expression of *Fezf2* was increased (+24%) in hM3Dq-infected L5 ET cells in mice treated with CNO compared with vehicle (Fig. 3b,c). These experiments confirmed a bidirectional link between the activity of L5 ET pyramidal cells and *Fezf2* expression.

To investigate whether the activity-dependent expression of *Fezf2* was cell-type specific or could be triggered by changes in activity in other types of pyramidal cells, we expressed hM3Dq in the other primary type of pyramidal neurons in L5 (IT neurons). To this end, we used *Tlx3-cre* mice, in which Cre expression is specific to L5 IT pyramidal cells[37]. We found that increasing the activity of L5 IT neurons between P8 and P10 does not change the expression of *Fezf2* in these cells (Fig. 3d–f). To explore more broadly whether other cortical neurons showed an activity-dependent upregulation of *Fezf2*, we used a simultaneous injection of AAV expressing Cre and activating DREADDs in S1. We overcame potential network effects by sparsely activating neurons across cortical

https://doi.org/10.1038/s41593-026-02515-6

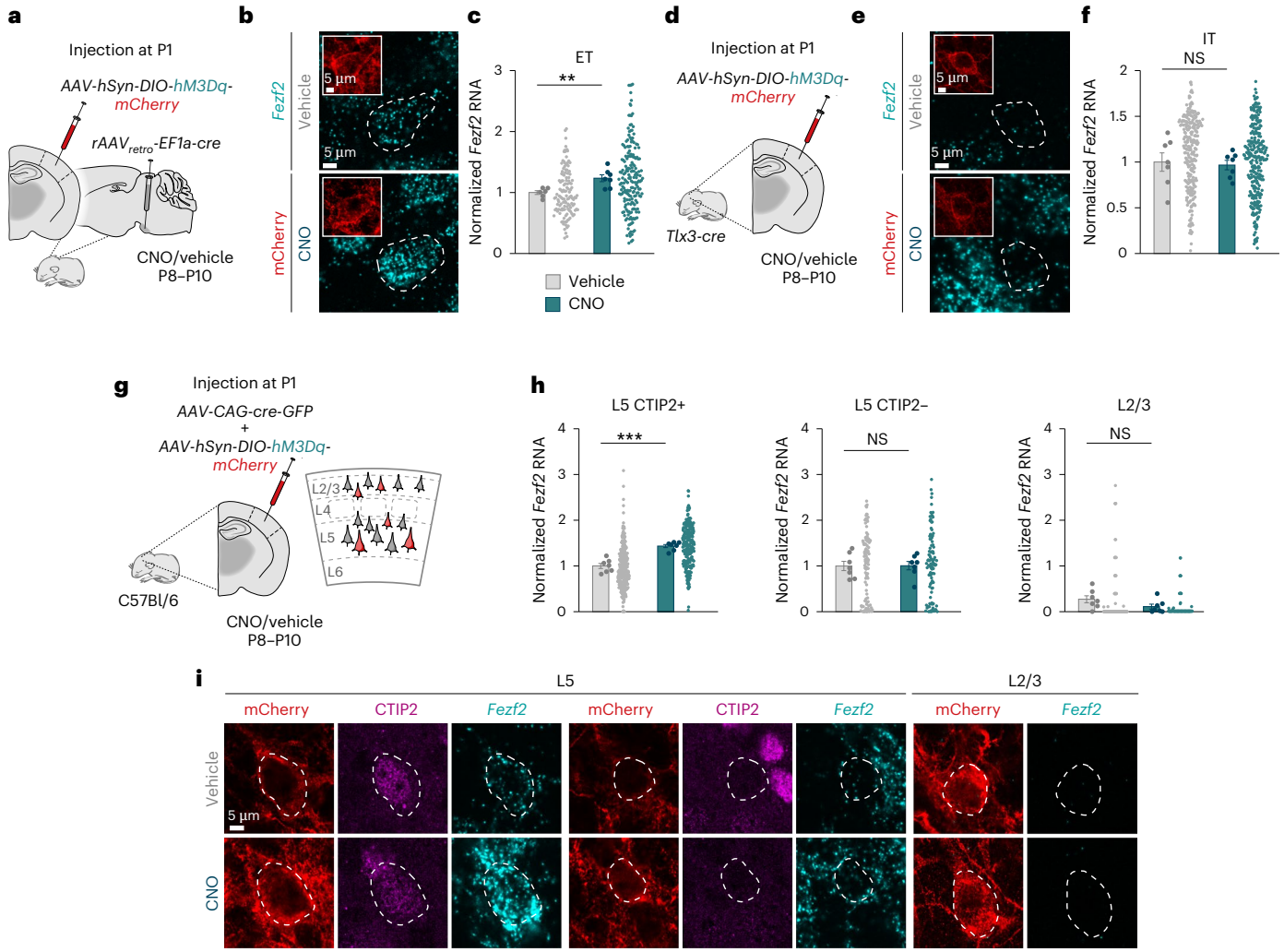

Fig. 3 | Activity regulation of *Fezf2* is cell-type specific. a, Experimental design for increasing activity by expressing hM3Dq in L5 ET cells. **b**, Confocal images showing *Fezf2* RNA (cyan) in hM3Dq-expressing L5 ET cells (mCherry, red). Scale bar = 5 µm. **c**, Quantification of *Fezf2* RNA signal in hM3Dq-expressing ET cells from mice injected with CNO compared with controls (vehicle, $n = 6$ mice; CNO, $n = 7$ mice, two-tailed Student's t-test, $^{**}P = 0.005$). **d**, Experimental design for increasing activity by expressing hM3Dq in IT pyramidal cells. **e**, Confocal images showing *Fezf2* RNA (cyan) in hM3Dq-expressing IT pyramidal cells (mCherry, red). Scale bar = 5 µm. **f**, Quantification of *Fezf2* RNA signal in hM3Dq-expressing IT cells from mice injected with CNO compared with controls (vehicle, $n = 7$ mice; CNO, $n = 7$ mice, two-tailed Student's t-test, $P = 0.78$). **g**, Experimental design for increasing activity by expressing hM3Dq in sparsely infected neurons throughout layer 2 of layers 3 and 5. **h**, Quantification of *Fezf2* RNA signal in hM3Dq-expressing CTIP2$^+$ L5 cells from mice injected with CNO compared with controls (vehicle, $n = 7$ mice; CNO, $n = 7$ mice, two-tailed Student's t-test, $^{***}P < 0.0001$), hM3Dq-expressing CTIP2$^-$ L5 cells from mice injected with CNO compared with controls (vehicle, $n = 7$ mice; CNO, $n = 7$ mice, two-tailed Student's t-test, $P = 0.97$) and hM3Dq-expressing layers 2 of 3 cells from mice injected with CNO compared with controls (vehicle, $n = 7$ mice; CNO, $n = 7$ mice, two-tailed Student's t-test, $P = 0.11$). Dotted lines indicate the outlines of somata, drawn from the mCherry signal. **i**, Confocal images relating to **h** showing *Fezf2* RNA expression (cyan) and CTIP2 (magenta) in hM3Dq-expressing pyramidal cells (mCherry, red). Scale bar = 5 µm. Replicates quantified in **h**. RNA levels are normalized per condition. Data are mean ± s.e.m. See Supplementary Table 2.

layers with a cocktail of low-titer AAVs expressing Cre and high-titer AAVs expressing hM3Dq. We distinguished L5 ET and IT cells by the presence or absence of the ET neuron marker CTIP2. Consistent with the results above, increasing neuronal activity increased *Fezf2* expression in CTIP2 + L5 neurons (+43%) but not in CTIP2−L5 neurons (Fig. 3g–i,n and Extended Data Fig. 5). In addition, L2/L3 neurons rarely expressed *Fezf2* in either vehicle or CNO conditions, with 74% and 81% of L2/L3 neurons not expressing any detectable *Fezf2* RNA, respectively (Fig. 3g–i). These observations show that *Fezf2* activity-dependent regulation is cell-type specific rather than universal across neuronal types.

We hypothesized that, as a cell-type-specific activity-regulated gene, *Fezf2* could function as an LRG and be activated by IEGs. To assess whether IEGs, including *Fos*, can activate the *Fezf2* promoter, we searched for putative binding sites of the AP-1 complex, which comprises a heterodimer of Fos/Jun family member proteins, within the *Fezf2* promoter region. We identified two putative AP-1 binding sites within the 2.7 kb region upstream of the transcription start site that was previously reported to drive *Fezf2* expression reliably across the developing cortex[38,39]. This region also contains a binding site for the IEG EGR1 (Extended Data Fig. 6a). We engineered a luciferase reporter fused to the 2.7 kb *Fezf2* promoter and cotransfected this construct with a combination of plasmids expressing the full-length *Fos*, *Jun* or *Egr1* cDNAs into HEK293 cells. Coexpression of Fos and Jun resulted in more than a twofold increase in luciferase activity compared with the promoter alone, while the combination of *Fos*, *Jun* and *Egr1* produced the highest activation of the promoter with a sixfold increase over control (Extended Data Fig. 6a,b). These results suggest that the *Fezf2* promoter can be activated by members of the FOS and JUN transcription factor families, as well as EGR1. To investigate whether FOS binds the *Fezf2* promoter in vivo, as a proof of concept, we examined chromatin

https://doi.org/10.1038/s41593-026-02515-6

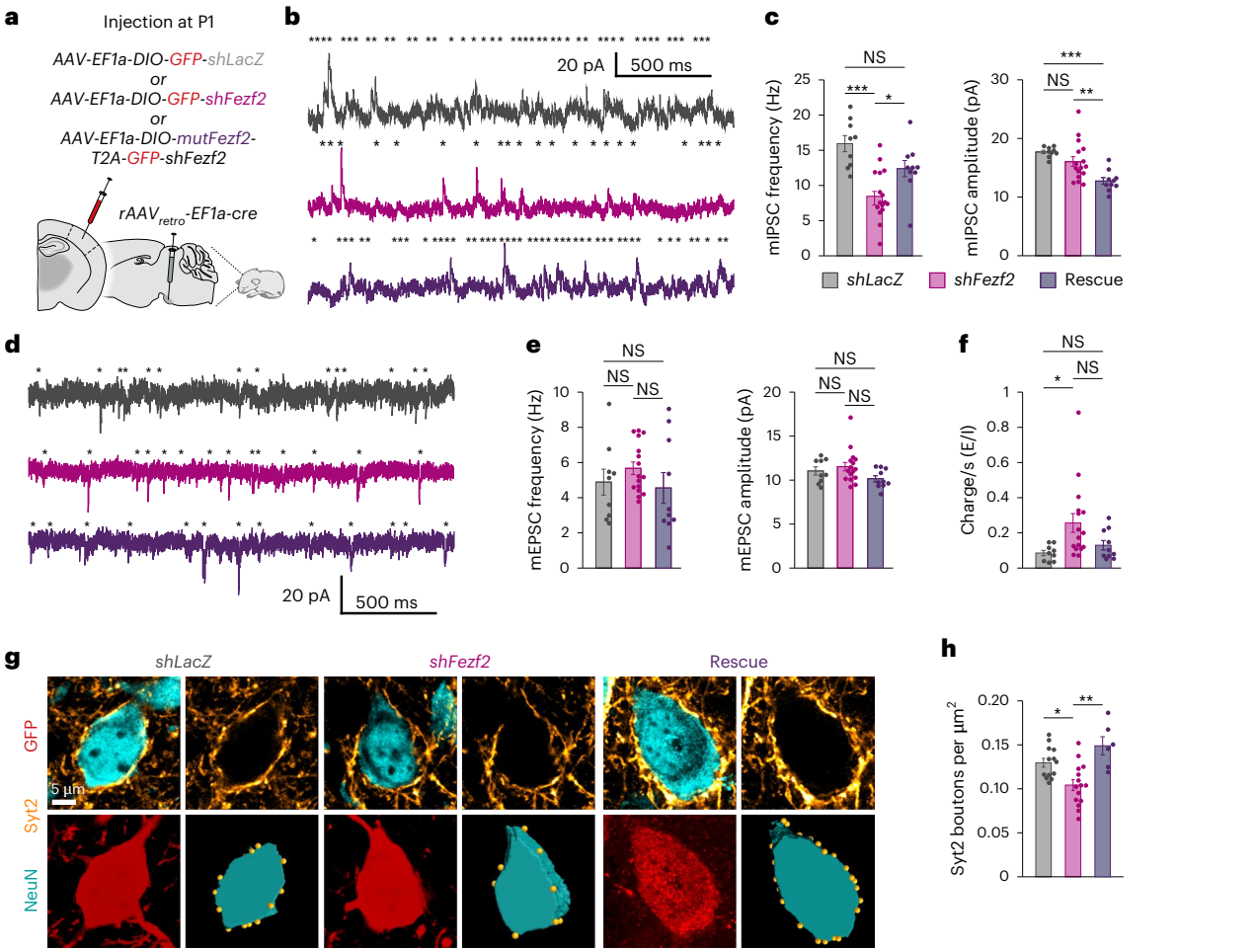

Fig. 4 | *Fezf2* regulates perisomatic inhibition onto L5 ET neurons. **a**, Experimental design for knockdown and subsequent rescue of *Fezf2* expression in L5 ET cells. **b**, Example traces showing mIPSCs recorded in L5 ET cells infected with either *shLacZ-GFP* (top), *shFezf2-GFP* (middle) or *shFezf2-mutFezf2* (rescue; bottom). Asterisks indicate the onset of mIPSC events. **c**, Quantification of mIPSC frequency (*shLacZ*, $n = 9$ cells from five mice; *shFezf2*, $n = 16$ cells from eight mice; rescue, $n = 10$ cells from four mice, one-way ANOVA, $P < 0.0001$; Tukey post hoc tests—*shLacZ* versus *shFezf2*, $^{***}P < 0.0001$; *shLacZ* versus rescue, $P = 0.09$; *shFezf2* versus rescue, $^{*}P = 0.0367$), and amplitude (*shLacZ*, $n = 9$ cells from five mice; *shFezf2*, $n = 16$ cells from eight mice; rescue, $n = 10$ cells from four mice, one-way ANOVA, $P = 0.0005$; Tukey post hoc tests—*shLacZ* versus *shFezf2*, $P = 0.2758$; *shLacZ* versus rescue, $^{***}P = 0.0005$; *shFezf2* versus rescue, $^{**}P = 0.0078$). **d**, Example traces showing mEPSCs recorded in L5 ET cells infected with either *shLacZ-GFP* (top) or *shFezf2-GFP* (middle) or *shFezf2-mutFezf2* (bottom). Asterisks indicate the onset of mEPSC events. **e**, Quantification of mEPSC frequency (*shLacZ*, $n = 9$ cells from five mice; *shFezf2*, $n = 16$ cells from seven mice; rescue, $n = 10$ cells from four mice, one-way ANOVA, $P = 0.38$) and amplitude (*shLacZ*, $n = 9$ cells from five mice; *shFezf2*, $n = 16$ cells from seven mice; rescue, $n = 10$ cells from four mice, one-way ANOVA, $P = 0.11$). **f**, Quantification of the ratio of the charge per second of mEPSCs and mIPSCs (*shLacZ*, $n = 9$ cells from five mice; *shFezf2*, $n = 16$ cells from seven mice; rescue, $n = 10$ cells from four mice, Brown–Forsythe and Welch ANOVA, $P = 0.0064$. Dunnett's multiple comparisons tests, *shLacZ* versus shFezf2, $^{*}P = 0.019$; *shLacZ* versus rescue, $P = 0.41$; *shFezf2* versus rescue, $P = 0.13$). **g**, Confocal images showing presynaptic Syt2 puncta (yellow), NeuN (cyan) and GFP (red). Bottom-right, three-dimensional Imaris reconstruction of the soma and Syt2 puncta. Scale bar = 5 µm. **h**, Quantification of the density of Syt2 puncta onto the soma (*shLacZ*, $n = 13$ mice; *shFezf2*, $n = 15$ mice, *mutFezf2-shFezf2* (rescue), $n = 6$ mice, one-way ANOVA, $P = 0.0007$; test included data shown in Fig. 7n; Tukey's post hoc tests—*shLacZ* versus *shFezf2*, $^{*}P = 0.0305$; *shLacZ* versus rescue, $P = 0.34$; *shFezf2* versus rescue, $^{**}P = 0.0015$). Data are mean ± s.e.m. See Supplementary Table 2.

immunoprecipitation followed by sequencing (ChIP–seq) data from hippocampal neurons of mice treated with kainic acid (KA) or vehicle (Extended Data Fig. 6c–e; ref. 40). KA-treated mice, which show robust activation of pyramidal cells, showed strong FOS binding at the *Fezf2* promoter 1 h after injection (Extended Data Fig. 6f). To assess whether the absence of *Fos* reduces *Fezf2* expression, we reanalyzed published single-nucleus RNA-seq (snRNA-seq) data from *Fos*/*Fosb*/*Jun* triple knockout mice[3]. In this study, the three alleles (*Fos*$^{fl/fl}$/*Fosb*$^{fl/fl}$/*Jun*$^{fl/fl}$) were deleted in hippocampal pyramidal neurons using a Cre-dependent system, following activity induced by KA. Because *Fezf2* is enriched in the CA3 region of the hippocampus (Extended Data Fig. 6g), we focused our analysis on nuclei from CA3 (Extended Data Fig. 6h). The deletion of FOS, FOSB and JUN in hippocampal neurons led to decreased *Fezf2* expression compared with control mice (Extended Data Fig. 6i). These findings indicate that *Fezf2* expression can be directly regulated by the IEG *Fos*.

Fezf2 regulates the assembly and maintenance of inhibition onto ET neurons

FEZF2 has a critical role in the specification of L5 ET neurons during embryonic development[27–30]. We found that neuronal activity regulates the expression levels of *Fezf2* in L5 ET cells during postnatal development, suggesting that this transcription factor may have additional roles in defining important features of these cells in an activity-dependent manner, long after they have been specified. We hypothesized that FEZF2 might regulate the density of perisomatic PV^{+} inhibitory inputs received by L5 ET cells in an activity-dependent manner. To test this idea, we engineered Cre-dependent AAVs

https://doi.org/10.1038/s41593-026-02515-6

containing the coding sequence for green fluorescent protein (GFP) and a short-hairpin RNA (shRNA) sequence against *Fezf2*. As a control, we used an shRNA sequence against β-galactosidase (*LacZ*), which does not target mammalian genes[11]. We verified the efficiency of *shFezf2* to downregulate the expression of *Fezf2* in vitro and in vivo (Extended Data Fig. 7a–e). We then injected $rAAV_{retro}$-*cre* in the pons and shRNA AAVs in the S1 at P1 and prepared acute slices from these mice at P15–P17 to allow for sufficient downregulation (Fig. 4a). Recordings of mIPSCs and mEPSCs in the same cell showed that, while downregulation of *Fezf2* reduced the frequency of mIPSCs (−45%), it did not alter the frequency and amplitude of mEPSCs (Fig. 4a–e). Consistent with this, reduction of *Fezf2* expression increased the E/I charge ratio (Fig. 4f). The mIPSC phenotype was replicated by measuring pharmacologically isolated mIPSCs (−45% mIPSC frequency; Extended Data Fig. 7d,f,g).

Supporting the idea that a decrease in PV synapses is, at least in part, contributing to the reduction of mIPSCs, the density of somatic PV$^+$ basket-cell boutons contacting L5 ET cells was decreased (−18%; Fig. 4g,h). Rescue experiments using an shRNA-resistant *Fezf2* (*AAV-hSyn-HA-mutFezf2-T2A-EGFP-shFezf2*) revealed that the phenotypes were caused by the specific downregulation of the target gene rather than off-target effects (Fig. 4a–h). Interestingly, although no change in mIPSC amplitude was observed between controls and *shFezf2*, in the rescue experiments, the mIPSC amplitude was decreased, likely due to a secondary effect of prolonged *Fezf2* overexpression. These experiments demonstrate that FEZF2 is cell-autonomously required for the regulation of appropriate PV$^+$ synapses to L5 ET neurons in response to activity during development. To evaluate whether *Fezf2* mediates activity-dependent changes in inhibitory synapses, we activated neurons using hM3Dq, while simultaneously modulating the expression of *Fezf2* (Extended Data Fig. 8). While increased activity raised the frequency of mIPSCs in control cells (Extended Data Fig. 8a–e), this synaptic increase was blocked by downregulation of *Fezf2* (Extended Data Fig. 8f–j). We observed no changes in mEPSCs under any of these conditions (Extended Data Fig. 8). Altogether, our data show that FEZF2 controls the PV interneuron inputs to ET pyramidal cells in an activity-dependent manner.

Because *Fezf2* is essential for the specification of L5 ET neurons early in development, our shRNA approach to downregulate *Fezf2* postnatally—despite only achieving a 50% decrease—could still potentially alter their cell identity, partially reprogramming these cells and subsequently decreasing their perisomatic inhibition. To investigate this, we examined whether postnatal downregulation of *Fezf2* affected other key features of L5 ET pyramidal cells[41–43]. In addition to finding no changes in excitatory inputs (Fig. 4d,e), we observed no differences in intrinsic properties, axonal projections, dendritic arborization, soma size or known molecular cell-type markers between *shFezf2*-infected neurons and control cells (Fig. 5). These findings suggest that the effect of reducing *Fezf2* expression on perisomatic inhibition is not secondary to changes related to cell-type identity.

Fezf2 continues to be expressed in L5 ET neurons in adulthood[44], suggesting that it may also regulate the maintenance of perisomatic inhibition in these cells later in life. To explore this possibility, we downregulated *Fezf2* expression at the end of the PV$^+$ synapse formation period[26]. In brief, we injected a retrograde AAV encoding an inducible Cre (CreERT2) into the pontine nuclei and introduced either *shFezf2* or *shLacZ* Cre-dependent AAVs into the S1 of wild-type mice at P1. We then induced Cre-dependent recombination by administering 4-hydroxytamoxifen (4-OHT) intraperitoneally at P21 (Extended Data Fig. 7h–i) and confirmed efficient downregulation of *Fezf2* expression by P35 (Extended Data Fig. 7j,k). Our results showed that, as in early knockdown experiments, late downregulation of *Fezf2* in L5 ET neurons reduces the density of Syt2$^+$ boutons contacting the soma of these cells (−14%; Extended Data Fig. 7l,m). Altogether, our findings demonstrate that FEZF2 is an activity-dependent, cell-type-specific transcription factor that regulates the formation and maintenance of PV$^+$ perisomatic synapses onto L5 ET pyramidal cells.

FEZF2 regulates *Cdh22* expression for the assembly of perisomatic PV$^+$ inhibition

Because FEZF2 is a transcription factor, we sought to uncover other LRGs that could be more directly involved in inhibitory synapse formation. Notably, the three top-ranked genes downregulated by a reduction in the activity of L5 ET neurons, *Cdh22*, *Cntn6* and *Igsf21*, encode cell-surface molecules (Fig. 2c–f), a type of protein involved in the formation and maintenance of synapses in the central nervous system[5,45–47]. We hypothesized that one of these proteins could function downstream of FEZF2 to regulate PV$^+$ perisomatic inhibition in L5 ET cells. To test whether changes in activity could bidirectionally regulate the expression of *Cdh22* and *Cntn6*, we then increased the activity of ET pyramidal neurons using chemogenetics and observed a subsequent increase in the expression of *Cdh22* (+34%) but not *Cntn6* (Fig. 6a–d). Interestingly, activity promotes FOS binding to intronic regions of the *Cdh22* locus, but not of *Cntn6* (Extended Data Fig. 6f).

To evaluate whether CDH22 functioned downstream of FEZF2, we first assessed whether, after increasing activity, *Fos*, *Fezf2* and *Cdh22* expression followed a temporal pattern consistent with a successive activation of these genes. *Fos* RNA was immediately upregulated, showing strong expression at 1 h after CNO injection, decreasing slightly at 6 h and being almost absent after 24 h (Extended Data Fig. 4d–f). *Fezf2* expression was upregulated 6 h after CNO injection (+16%, Fig. 6e–g). *Cdh22* expression increased only between 6h and 24 h (+85%; Fig. 6e–g), demonstrating sequential upregulation of *Fos* followed by increased expression of *Fezf2* and later *Cdh22*.

Fig. 5 | Cell-type-specific features are preserved after reduction of *Fezf2* expression. a, Example traces showing membrane voltage deflections in response to hyperpolarizing current steps. Bottom, quantification of cell-type-characteristic intrinsic properties in *shFezf2* compared with controls—input resistance (*shLacZ*, $n = 15$ from seven mice; *shFezf2*, $n = 15$ from seven mice, two-tailed Student's *t*-test, $P = 0.14$), sag current relative to steady state (*shLacZ*, $n = 15$ from seven mice; *shFezf2*, $n = 15$ from seven mice, two-tailed Student's *t*-test, $P = 0.26$) and capacitance (*shLacZ*, $n = 14$ from seven mice; *shFezf2*, $n = 15$ from seven mice, Mann–Whitney test, $P = 0.81$). **b**, Tiled confocal images showing no discernible axonal projections to the corpus callosum in *shFezf2*. Scale bar = 100 µm. **c**, Experimental design of **b**. Simultaneous expression of shRNAs and GFP from the same viral particles ensures that any axonal targeting of the corpus callosum after *Fezf2* knockdown would be detectable. **d**, Example reconstructions of apical dendritic trees of *shLacZ*-infected and *shFezf2*-infected neurons. Scale bar = 50 µm. **e**, Quantification of total apical dendrite length (*shLacZ*, $n = 17$ cells from three mice; *shFezf2*, $n = 43$ cells from nine mice, two-tailed Student's *t*-test, $P = 0.55$) and number of branch points (*shLacZ*, $n = 17$ cells from three mice; *shFezf2*, $n = 43$ cells from nine mice, two-tailed Student's *t*-test, $P = 0.74$). **f**, Sholl analysis of reconstructed apical dendritic trees (*shLacZ*, $n = 17$ cells from three mice; *shFezf2*, $n = 43$ cells from nine mice, mixed-effects analysis, shRNA factor, two-sided test, $P = 0.47$). **g**, Top, single-plane confocal images of GFP-filled somata of *shLacZ* (left) and *shFezf2-infected* (right) cells. Bottom, quantification of soma size (*shLacZ*, $n = 7$ mice; *shFezf2*, $n = 8$ mice, two-tailed Student's *t*-test, $P = 0.27$) and perimeter (*shLacZ*, $n = 7$ mice; *shFezf2*, $n = 8$ mice, two-tailed Student's *t*-test, $P = 0.34$). Scale bar = 10 µm. **h**, Confocal images showing GFP (red) and CTIP2 (cyan). Scale bar = 10 µm. **i**, Quantification of the percentage of infected cells that contain CTIP2 (*shLacZ*, $n = 1{,}517$ cells from four mice; *shFezf2*, $n = 1{,}016$ cells from four mice, Chi-square test (two sided), $P = 0.16$). **j**, Confocal images showing GFP (red), Tbr1 RNA (cyan) and Lmo4 RNA (magenta). Scale bar = 5 µm. **k**, Quantification of the expression of *Tbr1* (*shLacZ*, $n = 4$ mice; *shFezf2*, $n = 4$ mice, two-tailed Student's *t*-test, $P = 0.43$) and *Lmo4* (*shLacZ*, $n = 4$ mice; *shFezf2*, $n = 4$ mice, two-tailed Welch's *t*-test, $P = 0.43$). Data are mean ± s.e.m. See Supplementary Table 2.

https://doi.org/10.1038/s41593-026-02515-6

We then investigated whether FEZF2 regulates *Cdh22* expression by expressing a Cre-dependent construct encoding HA-tagged FEZF2 and GFP in L5 ET cells (Fig. 6h) and found that overexpression of *Fezf2* increases *Cdh22* expression (+22%; Fig. 6i–k). We then examined whether activity-dependent upregulation of *Cdh22* depends on *Fezf2*. To this end, we increased neuronal activity in L5 ET cells expressing *shFezf2* and measured *Cdh22* RNA levels. These experiments revealed that the downregulation of *Fezf2* abolished the increase in *Cdh22* expression induced by neuronal activation (Fig. 6l–p). Altogether, our findings indicate that the cell-surface molecule CDH22 functions downstream of FEZF2 in L5 ET pyramidal cells in an activity-dependent manner.

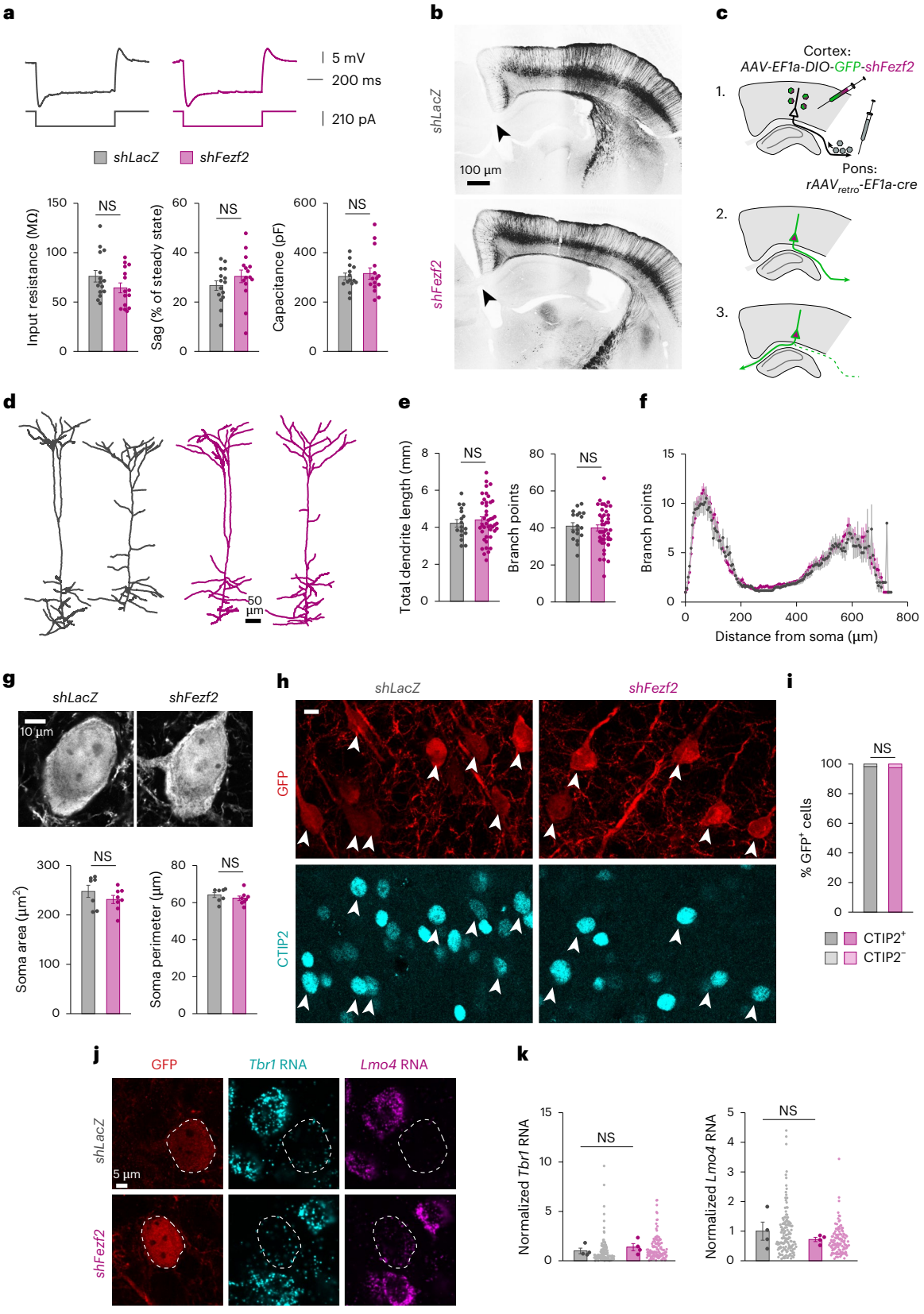

https://doi.org/10.1038/s41593-026-02515-6

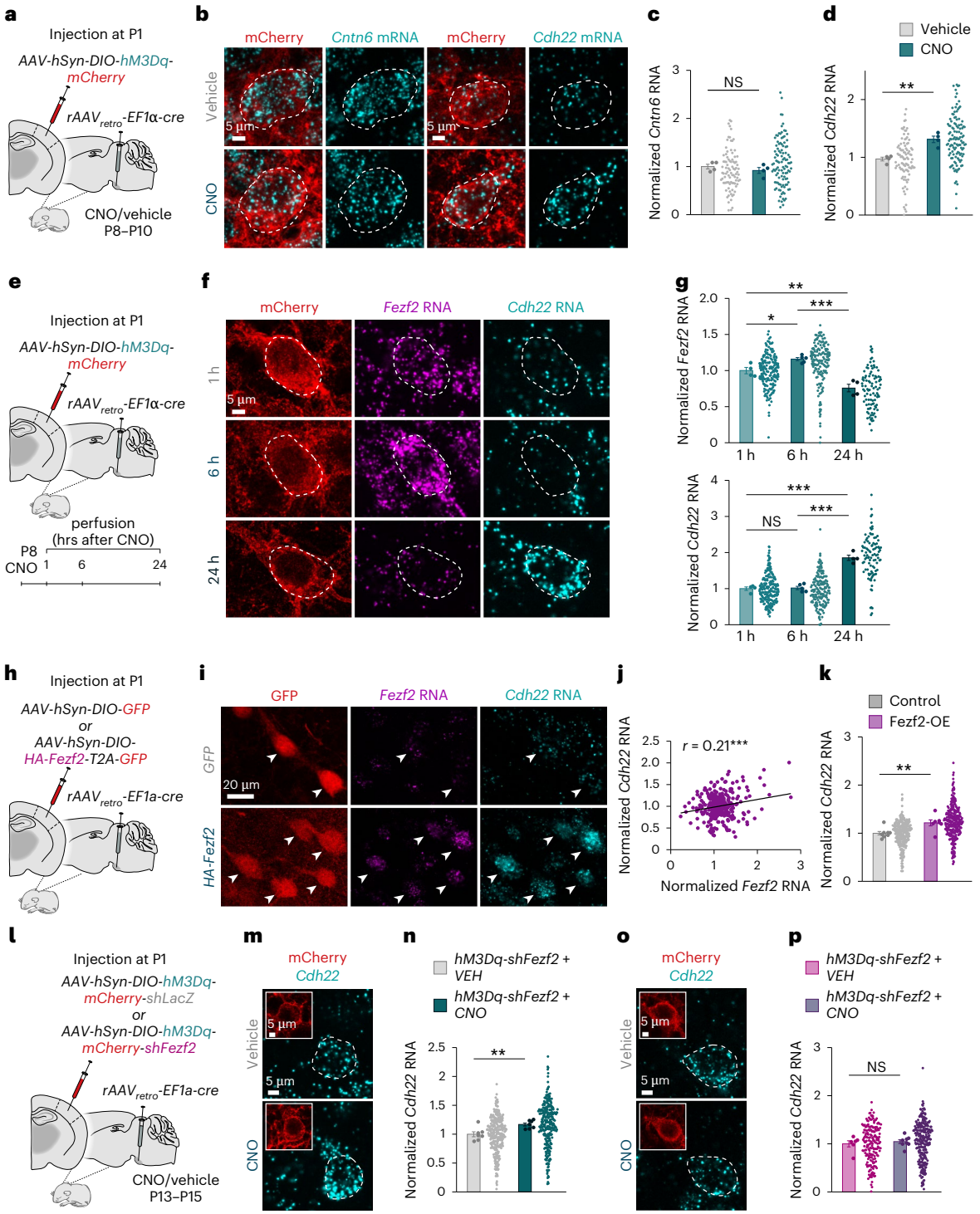

To assess whether CDH22 functions locally at perisomatic inhibitory synapses, we examined its subcellular localization. Because no antibodies reliably label CDH22, we engineered Cre-dependent AAVs expressing full-length CDH22 tagged with HA. Overexpression of tagged membrane proteins has been shown to predict endogenous protein expression[8,48]. We observed that the CDH22-HA is primarily restricted to the perisomatic plasma membrane, compatible with a role at perisomatic synapses (Extended Data Fig. 9). However, the intensity of the signal made the analysis of its synaptic localization challenging (Extended Data Fig. 9a). To overcome this limitation, we used the *Cdh22* rescue construct, containing a mutated, shRNA-resistant *Cdh22* (mutCDH22-HA) construct, which showed lower expression levels and allowed visualization of a punctate pattern at the membrane (Fig. 7a,b). Consistent with its potential role in synapse formation in L5 ET neurons, we found that exogenously expressed CDH22-HA clusters at the postsynaptic sites of PV$^+$ inputs in ET neurons (Fig. 7c–e).

To examine whether CDH22 is necessary for the development of PV$^+$ perisomatic inhibition in L5 ET neurons, we designed shRNA targeting *Cdh22* mRNA and confirmed its effectiveness both in vitro and in vivo (Extended Data Fig. 9b–d). We then conducted electrophysiological recordings in L5 ET neurons following the downregulation of *Cdh22* expression (Fig. 7f). We observed that the frequency of events was reduced in *shCdh22*-infected cells compared with *shLacz* control neurons, both for mIPSCs recorded with Cs-gluconate-based intracellular solution (−56%; Fig. 7g,h) and pharmacologically isolated mIPSCs (−32%; Extended Data Fig. 9k,i). Conversely, there were no differences

https://doi.org/10.1038/s41593-026-02515-6

Fig. 6 | Activity and *Fezf2* regulate *Cdh22* expression. a, Experimental design for increasing activity by expressing DREADDs in L5 ET cells. **b**, Confocal images showing *Cntn6* (left) or *Cdh22* (right) RNA expression (cyan) in AAV- and *rAAVretro-Cre*-infected L5 ET cells (mCherry, red). Scale bar = 5 µm. **c**, Quantification of *Cntn6* RNA signal in hM3Dq-expressing ET cells from mice injected with CNO compared with controls ($n = 4$ mice; CNO, $n = 4$ mice, two-tailed Student's *t*-test, $P = 0.35$). **d**, Quantification of *Cdh22* RNA signal in hM3Dq-expressing ET cells from mice injected with CNO compared with controls (vehicle, $n = 3$ mice; CNO, $n = 4$ mice, two-tailed Student's *t*-test, $^{**}P = 0.002$). **e**, Experimental design for increasing activity by expressing hM3Dq in L5 ET cells. Mice were perfusion fixed at 1 h, 6 h and 24 h after a single CNO injection. **f**, Confocal images showing *Fezf2* (magenta) and *Cdh22* (cyan) RNA expression in hM3Dq-expressing ET cells (mCherry, red) 1 h, 6 h and 24 h after CNO injection. Scale bar = 5 µm. **g**, Quantification of *Fezf2* (top) and *Cdh22* (bottom) RNA signal in hM3Dq-expressing ET cells at 1 h, 6 h and 24 h after CNO injection (1 h, $n = 4$ mice; 6 h, $n = 5$ mice; 24 h, $n = 4$ mice; *Fezf2*—one-way ANOVA, $P < 0.0001$; Tukey post hoc tests—1 h versus 6 h, $^{*}P = 0.0367$; 1 h versus 24 h, $^{**}P = 0.0045$; 6 h versus 24 h, $^{***}P < 0.0001$; *Cdh22*—one-way ANOVA, $P < 0.0001$; Tukey post hoc tests—1 h versus 6 h, $P = 0.97$; 1 h versus 24 h, $^{***}P < 0.0001$; 6 h versus 24 h, $^{***}P < 0.001$). **h**, Experimental design of *Fezf2* overexpression in L5 ET cells. **i**, Confocal images showing GFP (red), *Fezf2* RNA (magenta) and *Cdh22* RNA (cyan) in control and *Fezf2*-overexpressing cells. Scale bar = 20 µm **j**, Quantification of the correlation between *Fezf2* and *Cdh22* RNA signal in ET neurons overexpressing *Fezf2* ($n = 300$ cells from seven mice, $r = 0.21$, $^{***}P = 0.0003$). **k**, Quantification of *Cdh22* RNA signal in ET cells overexpressing *Fezf2* compared with controls (GFP, $n = 8$ mice; Fezf2-OE, $n = 7$ mice, two-tailed Student's *t*-test, $^{**}P = 0.0083$). **l**, Experimental design for increasing activity by expressing hM3Dq in L5 ET cells in which *Fezf2* is knocked down. **m**, Confocal images showing *Cdh22* RNA expression (cyan) in *shLacZ*-expressing and hM3Dq-expressing ET cells (mCherry, red). Scale bar = 5 µm. **n**, Quantification of *Cdh22* RNA signal in *shLacZ*-expressing and hM3Dq-expressing ET cells from mice injected with CNO compared with controls (vehicle, $n = 7$ mice; CNO, $n = 7$ mice, two-tailed Student's *t*-test, $^{**}P = 0.0055$). **o**, Confocal images showing *Cdh22* RNA expression (cyan) in *shFezf2*-expressing and hM3Dq-expressing L5 ET cells (mCherry, red). Scale bar = 5 µm. **p**, Quantification of *Cdh22* RNA signal in *shFezf2*-expressing and hM3Dq-expressing ET cells from mice injected with CNO compared with controls (vehicle, $n = 6$ mice; CNO, $n = 8$ mice, two-tailed Student's *t*-test, $P = 0.54$). Data are mean ± s.e.m. See Supplementary Table 2. QE, overexpression.

in the frequency or amplitude of mEPSCs (Fig. 7i,j), and the ratio of excitatory to inhibitory mIPSC charge per second was increased in *shCdh22*-infected cells (Fig. 7k). Consistent with these results, reducing *Cdh22* expression also lowered the density of PV$^+$ boutons contacting the soma of L5 ET neurons (−42%; Fig. 7l,m). Rescue experiments using an shRNA-resistant *Cdh22* (*AAV-hSyn-DIO-mutCdh22-HA-shCdh22*) confirmed that this phenotype was due to specific *Cdh22* downregulation, rather than off-target effects (Fig. 7l,m). In addition, overexpressing *Cdh22* restored the number of PV$^+$ boutons on ET cells diminished by *Fezf2* downregulation (Fig. 7n). Conversely, although *Cntn6* expression is regulated by *Fezf2*, lowering its expression does not reduce perisomatic inhibitory input (Extended Data Fig. 10), suggesting that it may have some other role. Altogether, our experiments revealed an activity-dependent molecular program involving FEZF2 and CDH22 that regulates the development of inhibitory connectivity between PV$^+$ interneurons and L5 ET pyramidal cells.

Discussion

In the adult cerebral cortex, neuronal networks show remarkable flexibility to cope with fluctuations in neuronal activity during ongoing environmental changes[15]. Pyramidal cells maintain their firing rates by regulating the level of inhibition they receive, which involves activity-dependent regulation of gene expression[17,22]. In this process, broadly expressed IEGs trigger the expression of effector factors in a cell-type-specific manner[22]. Our study reveals that these activity-dependent mechanisms are already at play during early postnatal development, and that in L5 ET neurons they are at least in part determined by *Fezf2*. *Fezf2* is a selector gene that specifies ET identity in the embryo[27–30]. We find that it is regulated postnatally by neuronal activity specifically in these same neurons and that activity-dependent changes in *Fezf2* expression sculpt the formation of PV$^+$ synapses onto ET pyramidal cells through the cell-surface molecule CDH22. These experiments uncovered a cell-type-specific transcription factor that establishes neuronal identity and is later repurposed, in an activity-dependent manner, to shape the wiring of the same neuron. Our findings suggest that cell-type-specific LRGs, such as FEZF2, provide cell-type specificity that activity-dependent cortical wiring requires.

Notably, our data showed that c-Fos occupies the *Fezf2* promoter and that *Fezf2* expression can be directly regulated by the IEG Fos, after robust activation with KA injections in vivo. Some of these mechanisms might be conserved in evolution, as immature human ET cells also coexpress FOS and FEZF2 (ref. 49). A limitation of our study is that we show the binding of c-Fos to the *Fezf2* promoter and that *Fezf2* expression depends on IEG *Fos* genes, using a well-established protocol of KA-induced seizures in the adult hippocampus. Although a subset of adult hippocampal pyramidal cells appears to show increased Fos

Fig. 7 | *Cdh22* controls perisomatic inhibition onto L5 ET neurons. **a**, Experimental design for visualization of exogenous CDH22-HA. **b**, Confocal image showing CDH22-HA (red) and Syt2 (cyan). Replicates quantified in **e**. Scale bar = 5 µm. **c**, Example analysis of part of the cell shown in **b**. Intensity profiles for CDH22-HA (red) and Syt2 (cyan) were measured along the outline of the soma. Peaks were detected and distances between each observed CDH22-HA peak and the nearest Syt2 peak were calculated. Peaks in both signals were then randomly distributed, maintaining the average density of peaks in each signal (shuffled peaks; bottom). Scale bar = 2 µm. **d**, Distribution of mean distances between shuffled CDH22-HA peaks and nearest shuffled Syt2 peaks in 1,000 iterations for the cell in **b**. Red line indicates actual observed value of mean distance between CDH22-HA and Syt2 peaks, with associated *z* score. **e**, The *z* scores of the distance between observed CDH22-HA and Syt2 peaks for individual cells differed significantly from 0; $n = 35$ cells from four mice, two-sided single-sample *t*-test, $^{***}P < 0.0001$. **f**, Experimental design of *Cdh22* downregulation. **g**, Example traces showing mIPSCs recorded in L5 ET cells infected with either *shLacZ* (top) or *shCdh22* (bottom) from P15–P17 mice. Asterisks indicate the onset of mIPSC events. **h**, Quantification of mIPSC frequency (*shLacZ*, $n = 24$ cells from nine mice; *shCdh22*, $n = 22$ cells from nine mice, Mann–Whitney test, $^{***}P < 0.0001$) and amplitude (*shLacZ*, $n = 24$ cells from nine mice; *shCdh22*, $n = 22$ cells from nine mice, two-tailed Student's *t*-test, $^{*}P = 0.0296$). **i**, Example traces showing mEPSCs recorded in L5 ET cells infected with either *shLacZ-GFP* (top) or *shCdh22-GFP* (bottom). Asterisks indicate the onset of mEPSC events. **j**, Quantification of mEPSC frequency (*shLacZ*, $n = 24$ cells from nine mice; *shCdh22*, $n = 22$ cells from nine mice, two-tailed Student's *t*-test, $P = 0.38$) and amplitude (*shLacZ*, $n = 24$ cells from nine mice; *shCdh22*, $n = 22$ cells from nine mice, two-tailed Student's *t*-test, $P = 0.91$). **k**, Quantification of the ratio of the charge per second of mEPSCs and mIPSCs (*shLacZ*, $n = 24$ cells from nine mice; *shCdh22*, $n = 22$ cells from nine mice, two-tailed Mann–Whitney test, $^{**}P = 0.0012$). **l**, Confocal images showing presynaptic Syt2 puncta (yellow), NeuN (cyan) and GFP (red). Bottom-right, three-dimensional Imaris reconstruction of the soma and Syt2 puncta. Scale bar = 5 µm. **m**, Quantification of the density of Syt2 puncta close to the soma (*shLacZ*, $n = 5$ mice; *shCdh22*, $n = 7$ mice, *shCdh22-mutCdh22-HA* (rescue), $n = 4$ mice, one-way ANOVA, $P = 0.0007$; Tukey post hoc tests—*shLacZ* versus *shCdh22*, $^{***}P = 0.0006$; *shLacZ* versus rescue, $P = 0.27$; *shCdh22* versus rescue, $^{*}P = 0.0273$). **n**, Quantification of the density of Syt2 puncta close to the soma (*shLacZ*, $n = 13$ mice; *shFezf2*, $n = 15$ mice, *shFezf2-mutCdh22-HA* (*Cdh22* rescue), $n = 7$ mice, one-way ANOVA, $P = 0.0007$; test included data shown in Fig. 4h; Tukey's post hoc tests—*shLacZ* versus *shFezf2*, $^{*}P = 0.0305$; *shLacZ* versus *Cdh22* rescue, $P = 0.88$; *shFezf2* versus *Cdh22* rescue, $^{*}P = 0.0161$). Data are mean ± s.e.m. See Supplementary Table 2.

https://doi.org/10.1038/s41593-026-02515-6

binding, more elaborate chromatin-binding studies will be needed to confirm this in ET pyramidal cells during development and also to determine whether other IEGs are involved. Our experiments revealed that overexpression of *Fezf2* increases the expression of *Cdh22* and *Cntn6* transcripts, suggesting that both cell-surface proteins are downstream of *Fezf2*. Consistent with this, *Fos*, *Fezf2* and *Cdh22* are upregulated sequentially upon increased neuronal activity, and activity-induced upregulation of *Cdh22* expression is prevented by reducing the levels of *Fezf2*. Further research is needed to determine whether FEZF2 regulates *Cdh22* expression by directly binding its promoter or through

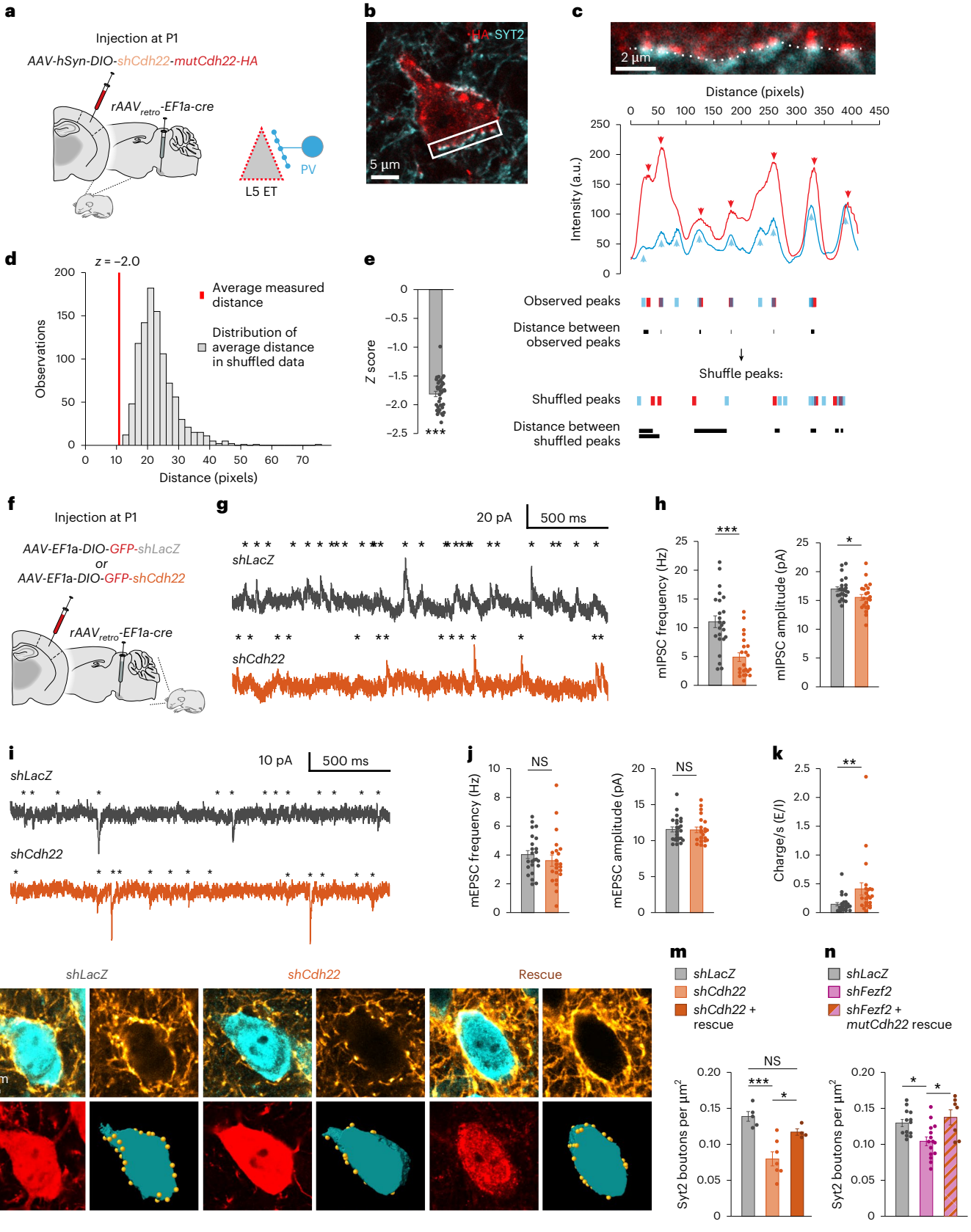

intermediate proteins. Of note, chromatin immunoprecipitation in progenitor cells from neurospheres identified FEZF2 binding sites close to the transcription start site of *Cdh22* but not *Cntn6* (ref. 30). Our experiments demonstrated that neuronal activity regulates *Cdh22* expression through FEZF2, and that *Cdh22* knockdown decreases the density of PV$^+$ perisomatic synapses contacting L5 ET pyramidal cells. The increase in both PV inputs and *Cdh22* expression mediated by activity can be prevented by reducing *Fezf2* levels. Likewise, the decrease in PV$^+$ perisomatic synapses in ET neurons expressing *shFezf2* can be rescued by overexpressing *Cdh22*. These findings show that *Cdh22* is a downstream effector of FEZF2 in the activity-dependent regulation of inhibitory synapses. While overexpression of Kir2.1 led to an increase in mEPSC frequency and amplitude, knockdown of *Fezf2* or *Cdh22* did not affect mEPSCs, suggesting that activity-dependent plasticity of excitatory and inhibitory synapses may use different molecular pathways. CDH22 can form homophilic and heterophilic interactions with other cadherin-family members[50]. Of these, *Cdh7* expression is enriched in PV$^+$ basket cells during postnatal development[11,51], suggesting a potential direct mechanism for the involvement of CDH22 in PV$^+$ basket-cell synapse formation onto ET neurons. We also observed that the downregulation of *Cntn6* does not affect the number of inhibitory inputs targeting L5 ET pyramidal cells. Thus, *Cntn6* may have a different role in shaping the maturation or connectivity of L5 ET neurons.

The excitation/inhibition (E/I) balance in the cerebral cortex is essential for the stabilization of neural circuit function[52], as well as cortical functions such as learning and memory[53,54]. To maintain an appropriate E/I balance in response to changes associated with sensory experience, pyramidal cells recruit inhibitory input in an activity-dependent manner[3,16,17]. This is mediated by the rapid initial expression of IEGs, most of which encode transcription factors that regulate a second wave of LRGs[22]. While most IEGs encode transcription factors such as FOS, JUN and NPAS4 (ref. 22), LRGs often encode molecules that are secreted or localized to the synapse[55–60]. These molecular programs generate the foundation for structural and functional modifications at the synapses. In the last decade, it has become clear that activity-regulated gene expression is not homogeneous across neuron types. Instead, while a common set of IEGs can be expressed across all neurons, the complement of LRGs that a neuron expresses in response to IEG induction often varies from one neuron type to another[58,61,62]. This cell-type specificity is hypothesized to come about through the combined action of commonly expressed activity-dependent transcription factors and cell-type-specific transcription factors that are not activity regulated at the same enhancers[63], but such factors have not been identified.

We have demonstrated that activity regulates the expression of the transcription factor *Fezf2* in ET cells but not in other pyramidal cells. To our knowledge, this is an example of a cell-type-specific transcription factor that controls the identity of the neuron and is later repurposed and regulated by activity to shape the wiring of the same neuron during development. While our data cannot exclude activity-independent functions of *Fezf2*, our findings demonstrate that *Fezf2* and *Cdh22* regulate inhibitory synapse formation and E/I balance through an activity-dependent mechanism. We have evidence that IEGs may regulate *Fezf2*. Thus, in addition to directly triggering known effector molecules like BDNF, IGF1 and SCG2 (refs. 3,63), IEGs may also regulate intermediate transcription factors that confer specificity to the wiring of specific populations of neurons, such as *Fezf2*. Interestingly, the transcription factor *Etv1/Er81* is required for the development of specific proprioceptive neuron connectivity in the spinal cord[64] and is an activity-regulated gene in PV interneurons[65]. It remains to be explored whether ETV11 has a role similar to FEZF2 in other neurons.

Fezf2 is a selector gene for L5 ET pyramidal cells, as its removal in embryos causes a loss of cell-type identity[27–30]. Interestingly, visual experience regulates upper-layer cell identity but not deep-layer cell identity in the visual cortex[66]. In addition, previous work has shown that *Fezf2* cannot reprogram upper-layer cell identity after the first postnatal week[67]. Although we cannot rule out the possibility that complete deletion of *Fezf2* in ET neurons postnatally might lead to loss of cell identity, we found that downregulating *Fezf2* expression by 50% during the postnatal period—an approach more similar to the Kir2.1 hyperpolarization experiments and likely closer to in vivo *Fezf2* expression dynamics—does not affect major cell identity features. The dual role of *Fezf2* during development is probably due to changes in the target genes it interacts with at different developmental stages. Consistent with this idea, *Fezf2* downregulation in adult mice affects a markedly different set of genes than during development[30,44]. Our findings revealed that *Fezf2* expression is regulated by neuronal activity postnatally. Other transcription factors also appear to be activity regulated during postnatal stages[55,59,68–70]. For example, *Satb1* is expressed during early development, but its expression is only influenced by activity after birth[70]. *Fezf2* may follow a similar two-stage regulatory process, being activity-independent before birth and activity dependent afterward.

It is tempting to speculate that cell-type-specific transcription factors regulated by IEGs may function as master regulators coordinating multiple transcription programs. Master regulators would differ among neurons to better fine-tune the circuitry depending on cell-type-specific demands. In this scenario, what better choice for a neuron than recycling a selector gene—an already cell-type-specific transcription factor—and using it postnatally in an activity-dependent manner? Future investigations should aim to elucidate whether other neurons use cell-type-specific activity-regulated transcription factors or whether this is a unique feature of ET pyramidal cells.

Online content

Any methods, additional references, Nature Portfolio reporting summaries, source data, extended data, supplementary information, acknowledgements, peer review information; details of author contributions and competing interests; and statements of data and code availability are available at https://doi.org/10.1038/s41593-026-02515-6.

References

1. Lim, L., Mi, D., Llorca, A. & Marín, O. Development and functional diversification of cortical interneurons. *Neuron* **100**, 294–313 (2018).
2. Fishell, G. & Kepecs, A. Interneuron types as attractors and controllers. *Annu. Rev. Neurosci.* **43**, 1–30 (2020).
3. Yap, E. L. et al. Bidirectional perisomatic inhibitory plasticity of *a Fos* neuronal network. *Nature* **590**, 115–121 (2020).
4. Favuzzi, E. & Rico, B. Molecular diversity underlying cortical excitatory and inhibitory synapse development. *Curr. Opin. Neurobiol.* **53**, 8–15 (2018).
5. Sanes, J. R. & Zipursky, S. L. Synaptic specificity, recognition molecules, and assembly of neural circuits. *Cell* **181**, 536–556 (2020).
6. Poulopoulos, A. et al. Neuroligin 2 drives postsynaptic assembly at perisomatic inhibitory synapses through gephyrin and collybistin. *Neuron* **63**, 628–642 (2009).
7. Fazzari, P. et al. Control of cortical GABA circuitry development by Nrg1 and ErbB4 signalling. *Nature* **464**, 1376–1380 (2010).
8. Exposito-Alonso, D. et al. Subcellular sorting of neuregulins controls the assembly of excitatory-inhibitory cortical circuits. *Elife* **9**, e57000 (2020).
9. Tanabe, Y. et al. IgSF21 promotes differentiation of inhibitory synapses via binding to neurexin2α. *Nat. Commun.* **8**, 408 (2017).
10. Chattopadhyaya, B. et al. Experience and activity-dependent maturation of perisomatic GABAergic innervation in primary visual cortex during a postnatal critical period. *J. Neurosci.* **24**, 9598–9611 (2004).
11. Favuzzi, E. et al. Distinct molecular programs regulate synapse specificity in cortical inhibitory circuits. *Science* **363**, 413–417 (2019).

12. Gour, A. et al. Postnatal connectomic development of inhibition in mouse barrel cortex. *Science* **371**, eabb4534 (2021).
13. Hensch, T. K. Critical period plasticity in local cortical circuits. *Nat. Rev. Neurosci.* **6**, 877–888 (2005).
14. Butt, S. J., Stacey, J. A., Teramoto, Y. & Vagnoni, C. A role for GABAergic interneuron diversity in circuit development and plasticity of the neonatal cerebral cortex. *Curr. Opin. Neurobiol.* **43**, 149–155 (2017).
15. Turrigiano, G. G. & Nelson, S. B. Homeostatic plasticity in the developing nervous system. *Nat. Rev. Neurosci.* **5**, 97–107 (2004).
16. Bloodgood, B. L., Sharma, N., Browne, H. A., Trepman, A. Z. & Greenberg, M. E. The activity-dependent transcription factor NPAS4 regulates domain-specific inhibition. *Nature* **503**, 121–125 (2013).
17. Xue, M., Atallah, B. V. & Scanziani, M. Equalizing excitation-inhibition ratios across visual cortical neurons. *Nature* **511**, 596–600 (2014).
18. Pan-Vazquez, A., Wefelmeyer, W., Gonzalez Sabater, V., Neves, G. & Burrone, J. Activity-dependent plasticity of axo-axonic synapses at the axon initial segment. *Neuron* **106**, 265–276 (2020).
19. Hinojosa, A. J., Deogracias, R. & Rico, B. The microtubule regulator NEK7 coordinates the wiring of cortical parvalbumin interneurons. *Cell Rep.* **24**, 1231–1242 (2018).
20. Kroon, T., van Hugte, E., van Linge, L., Mansvelder, H. D. & Meredith, R. M. Early postnatal development of pyramidal neurons across layers of the mouse medial prefrontal cortex. *Sci. Rep.* **9**, 5037 (2019).
21. Lin, Y. et al. Activity-dependent regulation of inhibitory synapse development by Npas4. *Nature* **455**, 1198–1204 (2008).
22. Yap, E.-L. & Greenberg, M. E. Activity-regulated transcription: bridging the gap between neural activity and behavior. *Neuron* **100**, 330–348 (2018).
23. Hattox, A. M. & Nelson, S. B. Layer V neurons in mouse cortex projecting to different targets have distinct physiological properties. *J. Neurophysiol.* **98**, 3330–3340 (2007).
24. Takahashi, N. et al. Active dendritic currents gate descending cortical outputs in perception. *Nat. Neurosci.* **23**, 1277–1285 (2020).
25. De Kock, C. P. J., Bruno, R. M., Spors, H. & Sakmann, B. Layer- and cell-type-specific suprathreshold stimulus representation in rat primary somatosensory cortex. *J. Physiol.* **581**, 139–154 (2007).
26. Jézéquel, J. et al. Cadherins orchestrate specific patterns of perisomatic inhibition onto distinct pyramidal cell populations. *Nat. Commun.* **16**, 4481 (2025).
27. Chen, J.-G., Rasin, M.-R., Kwan, K. Y. & Sestan, N. Zfp312 is required for subcortical axonal projections and dendritic morphology of deep-layer pyramidal neurons of the cerebral cortex. *Proc. Natl Acad. Sci. USA* **102**, 17792–17797 (2005).
28. Chen, B., Schaevitz, L. R. & McConnell, S. K. Fezl regulates the differentiation and axon targeting of layer 5 subcortical projection neurons in cerebral cortex. *Proc. Natl Acad. Sci. USA* **102**, 17184–17189 (2005).
29. Molyneaux, B. J., Arlotta, P., Hirata, T., Hibi, M. & Macklis, J. D. *Fezl* is required for the birth and specification of corticospinal motor neurons. *Neuron* **47**, 817–831 (2005).
30. Lodato, S. et al. Gene co-regulation by *Fezf2* selects neurotransmitter identity and connectivity of corticospinal neurons. *Nat. Neurosci.* **17**, 1046–1054 (2014).
31. De Boer, T. P., Houtman, M. J. C., Compier, M. & van der Heyden, M. A. G. The mammalian $K_{IR}2.x$ inward rectifier ion channel family: expression pattern and pathophysiology. *Acta Physiol. (Oxf.)* **199**, 243–256 (2010).
32. Nagy-Pál, P. et al. Structural organization of perisomatic inhibition in the mouse medial prefrontal cortex. *J. Neurosci.* **43**, 6972–6987 (2023).
33. Liu, X., Dimidschstein, J., Fishell, G. & Carter, A. G. Hippocampal inputs engage CCK+ interneurons to mediate endocannabinoid-modulated feed-forward inhibition in the prefrontal cortex. *Elife* **9**, e55267 (2020).
34. Sommeijer, J.-P. & Levelt, C. N. Synaptotagmin-2 is a reliable marker for parvalbumin positive inhibitory boutons in the mouse visual cortex. *PLoS ONE* **7**, e35323 (2012).
35. Nectow, A. R. et al. Rapid molecular profiling of defined cell types using viral TRAP. *Cell Rep.* **19**, 655–667 (2017).
36. Leone, D. P. et al. Satb2 regulates the differentiation of both callosal and subcerebral projection neurons in the developing cerebral cortex. *Cereb. Cortex* **25**, 3406–3419 (2015).
37. Gerfen, C. R., Paletzki, R. & Heintz, N. GENSAT BAC *cre*-recombinase driver lines to study the functional organization of cerebral cortical and basal ganglia circuits. *Neuron* **80**, 1368–1383 (2013).
38. Eckler, M. J. & Chen, B. Fez family transcription factors: controlling neurogenesis and cell fate in the developing mammalian nervous system. *Bioessays* **36**, 788–797 (2014).
39. Hirata, T. et al. Zinc-finger genes *Fez* and *Fez*-like function in the establishment of diencephalon subdivisions. *Development* **133**, 3993–4004 (2006).
40. Alaiz-Noya, M. et al. Neuronal type-specific modulation of cognition and AP-1 signaling by early-life rearing conditions. *Nat. Commun.* **16**, 9710 (2025).
41. Han, W. et al. TBR1 directly represses *Fezf2* to control the laminar origin and development of the corticospinal tract. *Proc. Natl Acad. Sci. USA* **108**, 3041–3046 (2011).
42. McKenna, W. L. et al. *Tbr1* and *Fezf2* regulate alternate corticofugal neuronal identities during neocortical development. *J. Neurosci.* **31**, 549–564 (2011).
43. Arlotta, P. et al. Neuronal subtype-specific genes that control corticospinal motor neuron development in vivo. *Neuron* **45**, 207–221 (2005).
44. Clare, A. J., Wicky, H. E., Empson, R. M. & Hughes, S. M. RNA-sequencing analysis reveals a regulatory role for transcription factor *Fezf2* in the mature motor cortex. *Front. Mol. Neurosci.* **10**, 283 (2017).
45. Südhof, T. C. Towards an understanding of synapse formation. *Neuron* **100**, 276–293 (2018).
46. De Wit, J. & Ghosh, A. Specification of synaptic connectivity by cell surface interactions. *Nat. Rev. Neurosci.* **17**, 22–35 (2016).
47. Shen, K. & Scheiffele, P. Genetics and cell biology of building specific synaptic connectivity. *Annu. Rev. Neurosci.* **33**, 473–507 (2010).
48. Favuzzi, E. et al. Activity-dependent gating of parvalbumin interneuron function by the perineuronal net protein Brevican. *Neuron* **95**, 639–655 (2017).
49. Kwan, K. Y. et al. Species-dependent posttranscriptional regulation of *NOS1* by FMRP in the developing cerebral cortex. *Cell* **149**, 899–911 (2012).
50. Brasch, J. et al. Homophilic and heterophilic interactions of type II cadherins identify specificity groups underlying cell-adhesive behavior. *Cell Rep.* **23**, 1840–1852 (2018).
51. Furlanis, E., Traunmüller, L., Fucile, G. & Scheiffele, P. Landscape of ribosome-engaged transcript isoforms reveals extensive neuronal-cell-class-specific alternative splicing programs. *Nat. Neurosci.* **22**, 1709–1717 (2019).
52. Ma, Z., Turrigiano, G. G., Wessel, R. & Hengen, K. B. Cortical circuit dynamics are homeostatically tuned to criticality in vivo. *Neuron* **104**, 655–664 (2019).
53. Huang, Z. J. et al. BDNF regulates the maturation of inhibition and the critical period of plasticity in mouse visual cortex. *Cell* **98**, 739–755 (1999).

54. Fagiolini, M. et al. Specific GABAA circuits for visual cortical plasticity. *Science* **303**, 1681–1683 (2004).
55. Flavell, S. W. et al. Activity-dependent regulation of MEF2 transcription factors suppresses excitatory synapse number. *Science* **311**, 1008–1012 (2006).
56. Hong, E. J., McCord, A. E. & Greenberg, M. E. A biological function for the neuronal activity-dependent component of *Bdnf* transcription in the development of cortical inhibition. *Neuron* **60**, 610–624 (2008).
57. Chang, M. C. et al. Narp regulates homeostatic scaling of excitatory synapses on parvalbumin-expressing interneurons. *Nat. Neurosci.* **13**, 1090–1097 (2010).
58. Mardinly, A. R. et al. Sensory experience regulates cortical inhibition by inducing IGF1 in VIP neurons. *Nature* **531**, 371–375 (2016).
59. Rajkovich, K. E. et al. Experience-dependent and differential regulation of local and long-range excitatory neocortical circuits by postsynaptic *Mef2c*. *Neuron* **93**, 48–56 (2017).
60. Diering, G. H. et al. Homer1a drives homeostatic scaling-down of excitatory synapses during sleep. *Science* **355**, 511–515 (2017).
61. Spiegel, I. et al. Npas4 regulates excitatory-inhibitory balance within neural circuits through cell-type-specific gene programs. *Cell* **157**, 1216–1229 (2014).
62. Spiegel, I. Experience-regulated molecular mechanisms in cortical GABAergic interneurons: from cellular functions to control over circuit plasticity. *Curr. Opin. Neurobiol.* **67**, 145–154 (2021).
63. Roethler, O. et al. Single genomic enhancers drive experience-dependent GABAergic plasticity to maintain sensory processing in the adult cortex. *Neuron* **111**, 2693–2708 (2023).
64. Arber, S., Ladle, D. R., Lin, J. H., Frank, E. & Jessell, T. M. ETS gene *Er81* controls the formation of functional connections between group Ia sensory afferents and motor neurons. *Cell* **101**, 485–498 (2000).
65. Dehorter, N. et al. Tuning of fast-spiking interneuron properties by an activity-dependent transcriptional switch. *Science* **349**, 1216–1220 (2015).
66. Cheng, S. et al. Vision-dependent specification of cell types and function in the developing cortex. *Cell* **185**, 311–327 (2022).
67. Rouaux, C. & Arlotta, P. Direct lineage reprogramming of post-mitotic callosal neurons into corticofugal neurons in vivo. *Nat. Cell Biol.* **15**, 214–221 (2013).
68. Sandmann, T. et al. A temporal map of transcription factor activity: mef2 directly regulates target genes at all stages of muscle development. *Dev. Cell* **10**, 797–807 (2006).
69. Andzelm, M. M. et al. MEF2D drives photoreceptor development through a genome-wide competition for tissue-specific enhancers. *Neuron* **86**, 247–263 (2015).
70. Close, J. et al. Satb1 is an activity-modulated transcription factor required for the terminal differentiation and connectivity of medial ganglionic eminence-derived cortical interneurons. *J. Neurosci.* **32**, 17690–17705 (2012).

Publisher's note Springer Nature remains neutral with regard to jurisdictional claims in published maps and institutional affiliations.

Open Access This article is licensed under a Creative Commons Attribution 4.0 International License, which permits use, sharing, adaptation, distribution and reproduction in any medium or format, as long as you give appropriate credit to the original author(s) and the source, provide a link to the Creative Commons licence, and indicate if changes were made. The images or other third party material in this article are included in the article's Creative Commons licence, unless indicated otherwise in a credit line to the material. If material is not included in the article's Creative Commons licence and your intended use is not permitted by statutory regulation or exceeds the permitted use, you will need to obtain permission directly from the copyright holder. To view a copy of this licence, visit http://creativecommons.org/licenses/by/4.0/.

© Crown 2026

Methods

Animals

All animal procedures were approved by the ethical committee (King's College London) and conducted in accordance with European regulations and under license from the UK Home Office following the Animals (Scientific Procedures) Act 1986 (Project Licenses: PD025E9BC, PP3627598). Both male and female mice were used. In all experiments, control and experimental groups contained similar numbers of male and female mice. Controls were always littermates of experimental animals. Postweaning, animals were housed in groups of up to five littermates and maintained under standard, temperature-controlled laboratory conditions. Mice were kept on a 12-h light/12-h dark cycle and received water and food ad libitum. Experiments were performed with experimental and control mice from the same litter, with littermates randomly assigned to experimental groups while balancing sex distributions across groups. Unless otherwise indicated, viral injections were performed on P1 and experiments were performed on P15 (perfusions) or P15–P17 (electrophysiology). Data collection and analysis were performed blindly to the conditions of the experiment. Wild-type animals were C57BL/6J (Charles River Laboratories). *Rbp4^{cre} and Tlx3^{cre}* (ref. 37) mice were obtained from the Mutant Mouse Resource and Research Center (MMRRC) at UC Davis (RRID: MMRRC_037128-UCD and RRID: MMRRC_041158-UCD) and maintained in a C57BL/6J background.

CNO treatment

CNO (Tocris Bioscience, 4936) was dissolved in 0.5% dimethyl sulfoxide (DMSO; Sigma-Aldrich, D0418) in 0.9% saline and stored at −20 °C. Vehicle control of 0.5% DMSO in 0.9% saline was used. Mice were treated with CNO for 48 h starting at P8—two injections per day (morning, between 8 and 9:30 a.m. and evening, between 6 and 8 p.m.) for a total of five injections. Animals were then perfused starting 2 h after the final injection on P10.

To verify the function of hM3Dq and CNO, animals received a single injection of CNO or vehicle and were perfused 2 h later. Immunohistochemistry was performed to assess the expression of c-Fos.

4-OHT

Animals expressing inducible Cre (CreERT2) received a single injection of 4-OHT (Sigma-Aldrich, H6278) on P21. On the day of injection, 4-OHT was dissolved in ethanol at 55 °C (100 mg ml^{-1}) and further diluted in sunflower seed oil (Sigma-Aldrich, S5007) to a final concentration of 10 mg ml^{-1}. Then, 4-OHT was administered through intraperitoneal injection at 50 mg kg^{-1}. Vehicle was prepared in the same manner.

KA treatment

Two-month-old C57BL/6J mice were treated with PBS (saline) of KA (two consecutive intraperitoneal injections separated by 30 min at 10 mg kg^{-1}). One hour after the first kainate injection, mice with level 4 epileptic seizures were killed, with subsequent dissection of their hippocampi for subsequent ChIP–seq.

Plasmid design

The coding sequences for Kir2.1-T2A-tdTomato and mutKir2.1-T2A-tdTomato (gifts from M. Scanziani; Addgene, 60661 and 60644) were subcloned into an hSyn-DIO backbone. *Kir2.1-T2A-Rpl10a-HA* and *mutKir2.1-T2A-Rpl10a-HA* inserts were constructed by GeneArt (Invitrogen) and subcloned into an hSyn-DIO backbone.

The coding sequences of *Fezf2* (NM_080433.3), *Cdh22* (NM_174988.3) and *Cntn6* (NM_017383.3), containing an HA-tag at either the N terminus (*Fezf2* and *Cntn6*) or C terminus (*Cdh22*), followed by a T2A peptide sequence and GFP, were produced and subcloned into a pcDNA 3.1(+) vector by GeneArt (Invitrogen). *HA-Fezf2-T2A-GFP* was subsequently subcloned into an hSyn-DIO backbone for viral production.

Design of shRNA sequences and shRNA-resistant proteins

Using *pAAV-EF1a-DIO-mCherry* described before, the coding sequence for mCherry was replaced with the coding sequence for GFP. The ssDNA primers to generate the shRNAs were either obtained using the BLOCK-it RNAi web tool (Thermo Fisher Scientific) or designed by hand and were as follows:

shFezf2-1 (forward: CTA GGC GGC TCT CTC TAC TAC TTC ACC TGA CCC ATG AAG TAG TAG AGA GAG CCG CTT TTT G, reverse: AAT TCA AAA AGC GGC TCT CTC TAC TAC TTC ATG GGT CAG GTG AAG TAG TAG AGA GAG CCG C); *shFezf2-2* (forward: CTA GGG TGT TCA ATG CTC ACT ATA ACC TGA CCC ATT ATA GTG AGC ATT GAA CAC CTT TTT G, reverse: AAT TCA AAA AGG TGT TCA ATG CTC ACT ATA ATG GGT CAG GTT ATA GTG AGC ATT GAA CAC C); *shFezf2-3* (forward: CTA GGC TGC TCA GTT ACT CGG AGT TCC TGA CCC AAA CTC CGA GTA ACT GAG CAG CTT TTT G, reverse: AAT TCA AAA AGC TGC TCA GTT ACT CGG AGT TTG GGT CAG GAA CTC CGA GTA ACT GAG CAG C); *shFezf2-4* (forward: CTA GGC TAG ACC GTT TGT GTG CAA ACC TGA CCC ATT TGC ACA CAA ACG GTC TAG CTT TTT G, reverse: AAT TCA AAA AGC TAG ACC GTT TGT GTG CAA ATG GGT CAG GTT TGC ACA CAA ACG GTC TAG C); *shFezf2-5* (forward: CTA GGA GTC AAG AGC CAC AGC AAA CCC TGA CCC AGT TTG CTG TGG CTC TTG ACT CTT TTT G, reverse: AAT TCA AAA AGA GTC AAG AGC CAC AGC AAA CTG GGT CAG GGT TTG CTG TGG CTC TTG ACT C); *shCdh22-6* (forward: CTA GGC AGA CGA CCC TAC TTA CAC GCC TGA CCC ACG TGT AAG TAG GGT CGT CTG CTT TTT G, reverse: AAT TCA AAA AGC AGA CGA CCC TAC TTA CAC GTG GGT CAG GCG TGT AAG TAG GGT CGT CTG C); *shCdh22-7* (forward: CTA GGG ACA ATG TGA TCA AAT AAC GCC TGA CCC ACG TTA TTT GAT CAC ATT GTC CTT TTT G, reverse: AAT TCA AAA AGG ACA ATG TGA TCA AAT AAC GTG GGT CAG GCG TTA TTT GAT CAC ATT GTC C); *shCdh22-8* (forward: CTA GGG CTG GCA CAA CAT TAC TAC GCC TGA CCC ACG TAG TAA TGT TGT GCC AGC CTT TTT G, reverse: AAT TCA AAA AGG CTG GCA CAA CAT TAC TAC GTG GGT CAG GCG TAG TAA TGT TGT GCC AGC C); *shCntn6-6* (forward: CTA GGG AGC ACA TCT CTA GTA CAC GCC TGA CCC ACG TGT ACT AGA GAT GTG CTC CTT TTT G, reverse: AAT TCA AAA AGG AGC ACA TCT CTA GTA CAC GTG GGT CAG GCG TGT ACT AGA GAT GTG CTC C); *shCntn6-7* (forward: CTA GGA AAT CCA AAT CCT TCG TAC GCC TGA CCC ACG TAC GAA GGA TTT GGA TTT CTT TTT G, reverse: AAT TCA AAA AGA AAT CCA AAT CCT TCG TAC GTG GGT CAG GCG TAC GAA GGA TTT GGA TTT C). Custom oligos were synthesized by Sigma-Aldrich. We used an *shLacZ* sequence as control, and the shRNAs were cloned into a backbone plasmid as described before[11].

To create Cre-dependent vectors encoding both hM3Dq-mCherry and Fezf2 shRNAs, we used a previously described vector *pAAV 8-hSyn-DIO-hM3D(Gq)-mCherry-shScg2-CWB* (a gift from O. Marin; Addgene, 223659)[71] and replaced the shScg2 sequence with shFezf2-1 and shFezf2-2, resulting in *pAAV-hSyn-DIO-hM3Dq-mCherry-shFezf2*. The control vector *pAAV-hSyn-DIO-hM3D(Gq)-mCherry-shLacZ-CWB* was a gift from O. Marin (Addgene, 223660).

To create shRNA-resistant *Fezf2*, parts of the full-length HA-tagged cDNA (see plasmid design above) were amplified by PCR using the following primers: *mutFezf2 FW1* (GTC TTT CCA CTG GGT TAA TTA ATC ACT TGT ACA GCT CGT CCA), *mutFezf2 RV1* (**GGT CTT TAA CGC CCA TTA CAA** CCT CAC CCG CCA CAT GCC TG), *mutFezf2 FW2* (**TTG TAA TGG GCG TTA AAG** ACC TTG CCG CAC ACT TCG CAG GT), *mutFezf2 RV2* (**TCA GGA AGC CTG TAT TAT TTT A**AC TAC CTG GAC TCC ACC GCT), *mutFezf2 FW3* (**AAA ATA ATA CAG GCT TCC TGA** GGC AGG CAG CCC CAC A), *mutFezf2 RV3* (TTA TAC GAA GTT ATC GCG GCG CGC CAT GTA CCC ATA CGA TGT TCC). The sequences in bold are synonymous with the target sequences of the *Fezf2* shRNAs, such that the bold sequences of *RV1* and *FW2* form a single mutated target sequence, as do the bold sequences of *RV2* and *FW3*. hM3Dq-mCherry was removed from both versions of *AAV-hSyn-DIO-hM3D(Gq)-mCherry-shFezf2-CWB* using digestion with restriction enzymes PacI and AscI (New England Biolabs). Gibson assembly was then performed using the resulting open backbone and the three PCR fragments and NEBuilder HiFi DNA

Assembly Master Mix (New England Biolabs). For shRNA-resistant Cdh22, a part of the *Cdh22* coding sequence containing a mutated version of the shRNA target sequence (AGA TAA CGT CAT AAA GTA) was ordered from GeneArt (Thermo Fisher Scientific). Each mutated shRNA target site contained at least six synonymous mutations.

In vitro validation of shRNA sequences

To assess the in vitro efficacy of shRNA by western blot, Cre-expressing human embryonic kidney (HEK; Ambion, SC004-BSD) cells were transfected with plasmids expressing cDNA and either *shLacZ* or the shRNA against the target gene. Thus, 48–72 h post-transfection, HEK293T cells were rinsed with 1× ice-cold PBS. Samples were homogenized in lysis buffer containing 25 mM Tris–HCl, pH 8, 50 mM NaCl, 1% Triton X-100, 0.5% sodium deoxycholate, 0.001% SDS and protease inhibitor cocktail (Complete, Mini). Three replicates were assessed for each shRNA sequence tested. Samples were resolved by SDS–PAGE and transferred onto PVDF membranes. Membranes were blocked with blocking solution consisting of 5% Blotting-Grade Blocker (Bio-Rad, 1706404) in TBST (20 mM Tris–HCl, pH 7.5, 150 mM NaCl and 0.1% Tween 20) for 1 h and incubated with mouse anti-HA (Invitrogen, 26183; 1:500) in blocking solution overnight at 4 °C. After washing 3 × 10 min in TBST, membranes were incubated with goat antimouse HRP (Invitrogen, 31444; 1:5,000) in blocking solution for 1 h at room temperature, followed by 3 × 10 min washes in TBST. Protein levels were visualized by chemiluminescence using either Immobilon Chemiluminescent HRP substrate ECL (MilliporeSigma, WBKLS0500) or SuperSignal West Femto Maximum Sensitivity Substrate (Thermo Fisher Scientific, 34095), depending on signal intensity. Blots were visualized using a LI-COR Odyssey Fc imaging system. Then, blots were washed in TBST and incubated with mouse anti-β-actin HRP (Sigma-Aldrich, A3854; 1:20,000) in blocking solution for 1 h at room temperature. Actin signal was visualized using SuperSignal West Pico Chemiluminescent substrate ECL (Thermo Fisher Scientific, 34577). For each sample, HA-signal intensity was normalized to the actin signal. The resulting value for each sample was then normalized to the *shLacZ* value within the same replicate. For *Fezf2*, shRNAs 1 and 2 were chosen. shRNA virus was made by cotransfecting both plasmids. For *Cdh22* and *Cntn6*, robust downregulation was only observed for one sequence. Therefore, only that sequence (*Cdh22-7* and *Cntn6-6*) was selected for viral production.

Virus production

For the in-house production of AAVs, HEK293FT cells (Thermo Fisher Scientific) were cultured in DMEM supplemented with 10% FBS, 2 mM glutamine, penicillin (50 units per ml^{-1}), streptomycin (50 g ml^{-1}) 200 mM HEPES (Thermo Fisher Scientific) and Gibco MEM nonessential amino acids. The cultures were incubated at 37 °C in a humidified atmosphere containing 5% CO_2. HEK293T cells were transfected using polyethylenimine (PEI; Sigma-Aldrich) at a 1:4 DNA:PEI ratio or Lipofectamine 2000 (Thermo Fisher Scientific). HEK293FT cells were seeded on 15-cm plates and cotransfected with packaging plasmids AAV-ITR-2 genomic vectors (7.5 µg), AAV-Cap8 vector pDP8 (30 µg; PlasmidFactory GmbH pF478) or AAV-Cap DJ Rep-Cap vector (30 µg; Cell Biolabs, VPK-420-DJ) using PEI (Sigma-Aldrich) at a ratio 1:4 (DNA:PEI). At 72 h post-transfection, supernatants were incubated with ammonium sulfate (65 g/200 ml supernatant) for 30 min on ice and centrifuged for 45 min at 4,000 rpm at 4 °C. Transfected cells were collected and lysed (150 mM NaCl, 50 mM Tris, pH 8.5), followed by three freeze-thaw cycles and Benzonase treatment (50 U ml^{-1}; Sigma-Aldrich) for 1 h at 37 °C. Filtered AAVs (0.8 µm and 0.45 µm mixed cellulose ester filters) from supernatants and lysates were run on an iodixanol gradient by ultracentrifugation (Vti50 rotor; Beckman Coulter) at 50,000 rpm for 1 h at 12 °C. The 40% iodixanol fraction containing the AAVs was collected, concentrated using 100-kDa molecular weight cutoff filters (Centricon Plus-20 and Centricon Plus-2; Merck), aliquoted and stored at −80 °C. The number of genomic copies was determined by qPCR using the following primers against the WPRE (forward: GGC ACT GAC AAT TCC GTG GT and reverse: CGC TGG ATT GAG GGC CGAA).

Homemade viruses used in this study were as follows: *AAV-hSyn-DIO-tdTomato* (3.58 × 10^{13} vg ml^{-1}), *AAV-hSyn-DIO-Kir2.1-T2A-tdTomato* (63 × 10^{13} vg ml^{-1}), *AAV-hSyn-DIO-mutKir2.1-T2A-tdTomato* (4.69 × 10^{13} vg ml^{-1}), *AAV-hSyn-DIO-HA-Fezf2-T2A-EGFP* (9.72 × 10^{11} vg ml^{-1}), *AAV-EF1a-DIO-EGFP-shLacZ* (8.00 × 10^{11} vg ml^{-1}), *AAV-EF1a-DIO-EGFP-shFezf2* (2.53 × 10^{12} vg ml^{-1}), *AAV-EF1a-DIO-EGFP-shCdh22* (9.07 × 10^{12} vg ml^{-1}), *AAV-EF1a-DIO-EGFP-shCntn6* (1.30 × 10^{13} vg ml^{-1}), *AAV-hSyn-DIO-EGFP-shLacZ* (1.32 × 10^{13} vg ml^{-1}), *AAV-hSyn-DIO-EGFP-shFezf2* (2.19 × 10^{13} vg ml^{-1}), *AAV-hSyn-DIO-HA-mutFezf2-T2A-EGFP-shFezf2* (2.70 × 10^{13} vg ml^{-1}), *AAV-hSyn-DIO-EGFP-shCdh22* (9.07 × 10^{12} vg ml^{-1}), *AAV-hSyn-DIO-Cdh22-HA* (4.10 × 10^{13} vg ml^{-1}), *AAV-hSyn-DIO-mutCdh22-HA-shCdh22* (1.98 × 10^{13} vg ml^{-1}), *pAAV-hSyn-DIO-hM3D(Gq)-mCherry-shLacZ-CWB* (1.13 × 10^{13} vg ml^{-1}), *AAV-hSyn-DIO-hM3D(Gq)-mCherry-shFezf2-CWB* (4.80 × 10^{12} vg ml^{-1}), *AAV-hSyn-DIO-mutCdh22-HA-shFezf2* (6.69 × 10^{12} vg ml^{-1}). The serotype of all viruses is *AAV8*.

Commercial viruses

The following commercial viruses were produced by Addgene: *rAAVretro-EF1a-Cre* (2.1 × 10^{13} vg ml^{-1}, 55636-AAVrg, a gift from K. Deisseroth), *AAV8-hSyn-DIO-hM3D(Gq)-mCherry* (1.8 × 10^{13} vg ml^{-1}, 44361-AAV8, a gift from B. Roth), *AAV8-hSyn-DIO-GFP* (2.3 × 10^{13} vg ml^{-1}, 50457-AAV8, a gift from B. Roth) and *AAV8-hSyn-DIO-EGFP* (2.3 × 10^{13} vg ml^{-1}, 50457-AAV8, a gift from B. Roth). *rAAVretro-hSyn-CreERT2* was obtained from the Viral Vector Facility of the University of Zurich (7.9 × 10^{12} vg ml^{-1}; v549).

Viral injections

P1 pups were anesthetized with isoflurane and mounted on a stereotactic frame (Stoelting). To target ET pyramidal neurons in wild-type animals, we used an intersectional strategy. *rAAV2retro-EF1a-cre* was injected in the pontine nuclei (anteroposterior = −1.2 mm, mediolateral = 0.3, dorsoventral = 4.2 and 4.0 mm from lambda; 150 nl per depth). For experiments involving inducible Cre, *rAAVretro-hSyn-creERT2* was injected instead. In the same animals, relevant Cre-dependent AAVs were injected in the ipsilateral S1 at a depth of 0.3 mm (single injection = 300 nl). For *Fezf2* overexpression experiments, AAVs were injected at P3. For analysis of dendritic morphology, *rAAV2retro-EF1a-cre* was diluted 1:3 and injections were targeted more medially (mediolateral = 0.15) to achieve a sparser infection in S1. For experiments using Cre lines, the virus was only injected into S1. Injection speed was 200 nl min^{-1} for all injections.

Luciferase assays

We generated a luciferase reporter vector by cloning the promoter region of the *Fezf2* gene into a *pGL4.11* plasmid (Promega) by Gibson assembly (New England Biolabs) using forward: CCA GAA CAT TTC TCT GGC CTT GGG CGG TGT GAA AAT ATT CTT CT and reverse: ACA GTA CCG GAT TGC CAA GCG GCG CGC CAA GCT G primers. Vectors for the expression of Fos (OMu22131D), Jun (OMu19159D) and Egr1 (OMu21683D) were obtained from GenScript. HEK293T cell lines were maintained in DMEM supplemented with L-glutamine, 10% FBS (Sigma-Aldrich) and 1% penicillin–streptomycin (Invitrogen). Cells were allowed to grow at 37 °C with 5% CO_2. HEK293T cells were seeded on 12-well plates and transfected (FuGENE HD, Promega) the next day with the luciferase reporter vectors (100 ng), the expression vectors (100 ng each) and the pRL-TK plasmid to express Renilla as an internal control (2 ng). After 16 h, cells were washed with PBS, and luciferase assays were performed in triplicate using the Rapid Detection Firefly Luciferase Activity assay system (Promega), following the manufacturer's instructions, with a CLARIOstar (BMG LABTECH) plate reader. Firefly luciferase activities were normalized based on the Renilla luciferase activity in each well.

In vitro electrophysiology

For all experiments, an experimental animal and an age-matched—and, where possible, sex-matched—littermate control was used for electrophysiology on the same day. Mice were deeply anesthetized with an overdose of sodium pentobarbital and transcardially perfused with 10 ml ice-cold slicing solution containing 87 mM NaCl, 75 mM sucrose, 26 mM $NaHCO_3$, 11 mM glucose, 7 mM $MgCl_2$, 2.5 mM KCl, 1.25 mM NaH_2PO_4 and 0.5 mM $CaCl_2$, oxygenated with 95% O_2 and 5% CO_2. The brain was quickly removed, and the injected hemisphere was glued to a cutting platform before being submerged in ice-cold slicing solution. Then, 300-µm-thick coronal slices containing S1 were cut using a vibratome (Leica, VT1200S) and incubated for 45–60 min at 32 °C, and subsequently at room temperature in the same solution. All salts were purchased from Sigma-Aldrich. Slices were transferred to the recording setup and superfused with recording artificial cerebrospinal fluid containing 124 mM NaCl, 1.25 mM NaH_2PO_4, 3 mM KCl, 26 mM $NaHCO_3$, 10 mM glucose, 2 mM $CaCl_2$ and 1 mM $MgCl_2$, which was oxygenated with 95% O_2 and 5% CO_2 and heated to 34 °C. Pipettes (3–5 MΩ) were made from borosilicate glass capillaries using a PC-10 pipette puller (P10; Narishige) and filled with intracellular solution containing 70 mM K-gluconate, 70 mM KCl, 10 mM HEPES, 4 mM Mg-ATP, 4 mM K2-phosphocreatine and 0.4 mM GTP, adjusted with KOH to pH 7.3 (±290 mOsm), or 125 mM Cs-gluconate, 5 mM CsCl, 4 mM NaCl, 10 mM HEPES, 0.2 mM EGTA, 2 mM K2-phosphocreatine, 2 mM Mg-ATP, 0.3 mM GTP, adjusted with KOH to pH 7.3 (±290 mOsm). Where applicable, 1% neurobiotin (Vector Laboratories) was added to the intracellular solution.

Recordings were made using a MultiClamp 700B amplifier (Molecular Devices). The signal was passed through a Hum Bug Noise Eliminator (Digitimer), sampled at 50 kHz (intrinsic properties) or 10 kHz (synaptic currents) and filtered at 3 kHz using a Digidata 1440A (Molecular Devices). Cells were excluded if the access resistance (Ra) exceeded 30 MΩ. Resting membrane potential (V_m) was measured in current-clamp mode for 5–10 s immediately after breaking in. Intrinsic properties were measured by applying a series of negative or positive current injections while maintaining a baseline Vm of −70 mV, at a step size of 25 pA. Active and passive properties were analyzed in MATLAB (MathWorks) using custom scripts. Input resistance was calculated as the linear slope of the current-voltage (I–V) relationship of the last 200 ms of all negative stimuli. Voltage sag was measured during the current step in which the peak voltage deflection was nearest to −90 mV, and was calculated as the percentage change between the peak of the response and the average voltage deflection of the last 200 ms of the same step. Rheobase was determined as the average first current injection to elicit an action potential across three series of current steps at a step size of 2 pA. Isolated mIPSCs recordings were performed at a holding potential of −76 mV in the presence of 1 µM tetrodotoxin (HB1035) 10 µM 2,3-dioxo-6-nitro-1,2,3,4-tetrahydrobenzo(f)quinoxaline-7-sulfonamide (NBQX, HB0443) and 50 µM D-(−)-2-amino-5-phosphonopentanoic acid (D-APV, HB0225), all of which were purchased from Hello Bio. mEPSCs and mIPSCs were measured from the same cells using cesium-based intracellular recording at holding potentials of −65 mV (mEPSCs) or +10 mV (mIPSCs) in the presence of 1 µM tetrodotoxin. mPSCs and mIPSCs were analyzed using Mini Analysis (SynaptoSoft).

Histology

Immunohistochemistry. Animals were deeply anesthetized with sodium pentobarbital by intraperitoneal injection and transcardially perfused with 0.9% saline followed by 4% paraformaldehyde (PFA) in PBS. Dissected brains were postfixed for 2 h at 4 °C in 4% PFA and cryoprotected in successive solutions of 15% and 30% sucrose (Sigma-Aldrich, S0389) in PBS. Sections of 40-µm thick containing S1 were cut using a sliding microtome (Leica, SM2010 R) and stored in ethylene glycol (30% ethylene glycol (Merck, 324558), 30% glycerol (Merck, G5516) in PBS) at −20 °C. For analysis of dendritic morphology, 350-µm-thick sections were cut. Free-floating sections were permeabilized with 0.25% Triton X-100 (Sigma-Aldrich, T8787) in PBS for 4× 15 min at room temperature (20–22 °C) and incubated for 2 h at room temperature in a solution containing 0.3% Triton X-100, 5% BSA (Sigma-Aldrich, A8806) and 10% normal goat serum and/or normal donkey serum, corresponding to the secondary antibodies used. Sections were then incubated overnight at 4 °C with primary antibodies in 0.3% Triton X-100, 2% BSA and 5% normal serum. Sections were washed 3× 10 min in PBS and incubated with secondary antibodies in 0.3% Triton X-100, 2% BSA and 5% serum for 2 h at room temperature. The following primary and secondary antibodies were used: mouse anti-NeuN (Sigma-Aldrich, MAB377; 1:500), rabbit anti-NeuN (MilliporeSigma, ABN78; 1:500), goat anti-mCherry (Antibodies-Online, ABIN1440057; 1:500), rabbit anti-DsRed (Clontech, 632496; 1:500), chicken anti-GFP (Aves Lab, GFP-1020; 1:1,000), mouse IgG2a anti-Syt2 (ZFIN, ZDB-ATB-081002-25; 1:250), mouse IgG1 anti-HA (BioLegend, 901502; 1:330), rat anti-HA (Roche (Sigma-Aldrich), 11867423001; 1:500), rat anti-CTIP2 (Abcam, ab18465; 1:500), rabbit anti-CFOS (SySy, AbE457; 1:500), goat antimouse IgG1 488 (Invitrogen, A-21121; 1:500), goat antichicken 488 (Invitrogen, A-11039; 1:500), donkey antirabbit 488 (Invitrogen, A-21206; 1:500), donkey antirabbit 555 (Invitrogen, A-31572; 1:500), donkey antigoat 555 (Invitrogen, A-21432; 1:500), goat antimouse IgG1-555 (Invitrogen, A-21127; 1:500), goat antirat 555 (Invitrogen, A-21434; 1:500) and goat antimouse IgG2a 647 (Invitrogen, A-21241; 1:500).

For the physiological validation of the function of *AAV-hSyn-DIO-Kir2.1-RPL10a*, cells were filled with neurobiotin during recording, and slices were subsequently fixed in PFA for 1 h at room temperature. Slices were incubated with 1:500 Streptavidin 488 (Thermo Fisher Scientific) in PBS containing 0.25% Triton for 24 h at 4 °C. Immunohistochemistry was then performed as described above using mouse IgG1 anti-HA and donkey antimouse IgG1-555.

smFISH. Animals were perfused as previously described. Brains were dissected and postfixed overnight in 4% PFA at 4 °C, followed by cryoprotection in 15% and 30% sucrose in RNase-free PBS at 4 °C. Here 30-µm-thick sections were cut and stored in RNase-free ethylene glycol solution at −70 °C. Sections were mounted on RNase-free SuperFrost Plus slides (Epredia, J1800AMNZ) and dehydrated using successive steps of 50%, 70% and 100% ethanol.

smFISH was performed using the RNAscope Multiplex Fluorescent Assay (v2) protocol (Advanced Cell Diagnostics; ACDBio, 323110) according to the manufacturer's instructions. *Fezf2* (ACDBio, 313301 and 313301-C2), *Cdh22* (ACDBio, 573541-C3), *Cntn6* (ACDBio, 836461), Tbr1 (ACDBio, 413301) and Lmo4 (ACDBio, 485491-C2) RNA was visualized using Opal 570 (Akoya Biosciences, FP1488001KT) and Opal 650 (Akoya Biosciences, FP1496001KT). Immunohistochemistry was then performed to visualize infected neurons. Slide-mounted sections were incubated in blocking buffer containing 10% normal goat serum for 30 min at room temperature, and incubated with primary antibodies chicken anti-GFP (Aves Lab, GFP-1020; 1:500) and chicken anti-GFP (Abcam, ab13970; 1:500) overnight at 4 °C. After washing, sections were incubated with goat antichicken Alexa Fluor 488 (Molecular Probes, A-11039) for 2 h at room temperature.

Image acquisition and analysis. Except where noted, all images were acquired using an inverted Leica TCS SP8 confocal microscope and LAS X software. For analysis of perisomatic boutons, *z* stacks were acquired using a ×100 numerical aperture (NA) 1.44 oil immersion objective at a voxel size (*xyz*) of 0.05 × 0.05 × 0.2 µm maintaining the same laser power, photomultiplier gain, pinhole and detection filter settings for all animals within an experiment and analyzed with Imaris (v7.5.2) software. Somata were manually reconstructed from NeuN signal using the Surface function. The detection threshold for Syt2 puncta was adjusted

for staining intensity per animal and Syt2 puncta were automatically detected using the Spots function. The number of Syt2 puncta close to the reconstructed soma was quantified using the 'Find spots close to surface' tool (ImarisXT extension) with a distance threshold of 0.4 µm.

For analysis of smFISH, single-plane images were acquired on an inverted Leica TCS SP8 confocal microscope using a ×63 NA 1.4 oil immersion objective at a pixel size (*xy*) of 0.09 × 0.09 µm. Images were analyzed using custom MATLAB (MathWorks) scripts[72]. The regions of interest (ROIs) covering the soma of infected cells were manually delineated using the fluorescence reporter signal, and RNA signal was measured for each infected cell as the surface of the RNA signal within the ROI divided by the total surface of the ROI, expressed as a percentage. Because RNAscope signal quality can vary significantly between animals and even within sections, for each image, the value of each ROI was normalized to the brightest uninfected cell in the image. All data within each experiment were then normalized to the average value of the control group to make for an easier comparison of the magnitude of changes in expression levels. The one exception to this is the data shown in Fig. 3m. As the majority of values in this dataset were zero, the data were normalized to the average value of all control cells after excluding all values of zero. For both quantification of synaptic boutons and smFISH, a minimum of 15 cells were analyzed per animal, except the data shown in Fig. 3m, where one animal contained only seven cells. The average value per animal was used for all statistical analyses.

To determine whether recorded and neurobiotin-filled cells were positive for HA, cells were imaged using a ZEISS ApoTome microscope with a ×63 NA 1.4 objective. Only cells with strong HA signal were included in subsequent analysis of electrophysiological recordings.

For visualization of c-Fos, as well as for visualization of tdTomato and GFP in CreERT2 control experiments, low-magnification confocal images were obtained using a ×10 NA 0.3 dry objective. c-Fos-expressing cells were quantified using the Cell Counter plugin in Fiji[73].

For visualization of axonal projections, single-plane confocal images were obtained using a ×10 NA 0.3 dry objective at pixel size (*xy*) 3 × 3 µm and stitched in LAS X.

For analysis of dendritic morphology, confocal images were obtained using a ×20 NA 0.5 dry objective at voxel size (*xyz*) 0.19 × 0.19 × 1 µm. The morphology of the apical dendritic tree was reconstructed and analyzed using semi-automated tracing in the SNT plugin for Fiji[74].

For analysis of colocalization of CDH22-HA and Syt2, single-plane confocal images were obtained using a ×63 NA 1.4 oil immersion objective at a pixel size (*xy*) of 0.05 × 0.05 µm. We used a custom script in MATLAB (MathWorks) to extract intensity profiles of CDH22-HA and Syt2 along the outline of the soma with the 'improfile' function. Peaks were detected using the findpeaks function with MinPeakProminence 3 and MinPeakDistance 20, and the distances between each CDH22-HA peak and the closest Syt2 peak were calculated. Subsequently, for each cell, shuffled data were produced by randomly generating 'peak' positions while maintaining the total length of the profile and the number of peaks in each channel. The average distance between each CDH22-HA position and the closest Syt2 position was calculated for each of 1,000 iterations, creating the expected distribution of distances between CDH22-HA and Syt2 if localization of these proteins was uncorrelated. The observed mean distance for each cell was then compared with this distribution, generating a *z* score for that value.

RNA-seq

Ribosome-associated RNA isolation. Mice were deeply anesthetized with an overdose of sodium pentobarbital. The infected cortex was rapidly dissected in ice-cold RNase-free PBS. Lower layers of S1 were dissected out and immediately homogenized in ice-cold lysis buffer (50 mM Tris–HCl, pH 7.5, 100 mM KCl, 12 mM $MgCl_2$, 1 mg ml^{-1} heparin (Sigma-Aldrich), complete EDTA-free protease inhibitors (Sigma-Aldrich), 200 U ml^{-1} RNasin (Promega), 100 µg ml^{-1} cycloheximide and 1 mM dithiothreitol (Sigma-Aldrich)). Tissue from two to three brains were pooled per sample. Samples were centrifuged at 2,000*g* for 10 min at 4 °C, and IGEPAL CA-630 (Sigma-Aldrich) was added to the samples to a final concentration of 1%. Samples were then centrifuged at 13,000*g* for 10 min at 4 °C. The supernatant was added to 100 µl of anti-HA magnetic beads (Pierce, 88837) for 3–4 h at 4 °C with gentle rotation. After incubation, beads were washed thrice in ice-cold washing buffer (300 mM KCl, 1% IGEPAL CA-630, 50 mM Tris–HCl, pH 7.5, 12 mM $MgCl_2$, 1 mM dithiothreitol and 100 µg ml^{-1} cycloheximide) and eluted in 350 µl of RLT Plus buffer (RNeasy Plus Micro kit, Qiagen) supplemented with 2-mercaptoethanol (Bio-Rad).

RNA purification, library preparation and sequencing. Purification of immunoprecipitated RNA was performed using the RNeasy Plus Micro kit (Qiagen) following the manufacturer's protocol. The quality of immunoprecipitated RNA was verified on a 2100 Bioanalyzer instrument (Agilent Technologies) using an RNA 6000 Pico Chip. All RNA samples had RNA integrity number values of 9.8 or higher. Three biological replicates were analyzed for each genotype. Library preparation and RNA-seq experiments were performed by the Genomics Unit of the Centre for Genomic Regulation. Libraries were prepared using the NEBNext Poly(A) mRNA Magnetic Isolation Module (New England Biolabs, 7490) and the NEBNext Ultra II Directional RNA Library Prep Kit for Illumina (New England Biolabs, 7760) according to the manufacturer's protocol. Libraries were then sequenced in paired-end mode using an Illumina HiSeq 2500 platform to a minimum of 100 million mapped reads per sample.

RNA-seq analysis. Bioinformatic analyses were carried out by GenoSplice. Briefly, data quality was assessed using FastQC and RSeQC[75]. Reads were mapped using STAR_2.4.0 (ref. 76) to the reference genome mm10. Counts were obtained through FAST DB (v2018_1), gene annotations (GenoSplice) and normalization using DESeq2 (ref. 77). One sample (mutKir1) did not cluster sufficiently and was excluded from further differential gene analysis and selection of target genes. GO analysis was performed using WebGestalt[78] with the terms biological process, cellular component and molecular function, as well as the KEGG and Reactome pathway databases. GO terms were considered to be significantly enriched at a false discovery rate <0.05.

To select gene targets, DEGs within the following PANTHER GO terms were considered: 'cell adhesion molecule' (PC00069), 'scaffold/adaptor protein' (PC00226) and 'C2H2 zinc-finger transcription factor' (PC00248). Genes were then ranked using three criteria. First, genes were scored according to the expression FC between Kir2.1 and mutKir2.1. Second, because low-count genes are often unreliable, genes were ranked according to their expression levels in mutKir2.1 controls. Third, to bias toward ET-specific genes, genes were scored according to the differences in expression levels between ET cells and IT cells using snRNA-seq data from the Allen Brain Institute database[79]. These criteria were converted into a single rank score by calculating *z* scores for each criterion and averaging the absolute *z* score of criterion 1 and the *z* scores of criteria 2 and 3. Rankings for all criteria and the final rank score are shown in Fig. 2c.

ChIP–seq analysis

ChIP–seq was performed on whole hippocampi of mice treated with KA or saline. For each condition, three biological replicates were generated, each derived from an individual mouse. A Dounce homogenizer was used to dissociate hippocampal tissue suspended in ice-cold hypotonic NEB fixing buffer containing 250 mM sucrose, 25 mM KCl, 5 mM $MgCl_2$, 20 mM HEPES-KOH (pH 7.8), 0.5% IGEPAL CA-630, 0.2 mM spermine, 0.5 mM spermidine, 1× protease inhibitor and 1.1% PFA. The homogenate was incubated at room temperature for 15 min followed by incubation with 0.125 M glycine for 5 min to stop the fixation and was washed twice by centrifugation with ice-cold NEB buffer without

PFA. The pellet of nuclei was suspended in 400 µl of RIPA lysis buffer (1% IGEPAL CA-630, 0.1 SDS, 0.5% sodium deoxycholate, PBS 1×; pH 8) before sonication in a Sonifier digital SFX 250 (Branson) for nine 15-s on/30-s off cycles. After 15 min of centrifugation at 17,000*g*, the supernatant containing isolated chromatin was collected. Samples were diluted in 4,000 µl of ChIP dilution buffer (0.01% SDS, 1.1% Triton X-100, 1.2 mM EDTA, 16.7 mM Tris–HCl, 167 mM NaCl; pH 8) and incubated overnight at 4 °C with the α-Fos monoclonal antibody (rabbit; Thermo Fisher Scientific, T.142.5). The next day the chromatin was incubated 3 h with 60 µl of slurry Dynabeads coated to Protein G (Invitrogen) at 4 °C. Beads were thoroughly rinsed at 4 °C as follows: two washes in RIPA-150 buffer, three washes in RIPA-500 buffer (50 mM Tris–HCl, 500 mM NaCl, 1 mM EDTA, 0.1% SDS, 1% Triton X-100, 0.1% sodium deoxycholate; pH 8), two washes in RIPA LiCl buffer (50 mM Tris–HCl, 1 mM EDTA, 1% NP-40, 0.7%, sodium deosycholate, 500 mM $LiCl_2$) and two final washes in TE buffer (10 mM Tris–HCl, pH 8.0, 1 mM EDTA; pH 8.0), for 5 min each. Samples were resuspended in 200 µl Elution buffer (1% SDS, 0.1 M $NaHCO_3$) and treated with 1 µl of 10 mg ml^{-1} RNase A (Fermentas) overnight at 65 °C with agitation for crosslink reversion. Samples were treated with 2 µl of 20 mg ml^{-1} proteinase K (Thermo Fisher Scientific) for 5 h at 55 °C with agitation. Finally, DNA precipitation was performed by phenol-chloroform-isoamyl alcohol (Sigma-Aldrich). As a control, a parallel input sample (without antibody) was processed to assess background signal. Sequencing (50 bp single end) was performed using a HiSeq 2500 sequencer. Raw reads were trimmed with trim_galore (v0.6.4_dev)[80] and aligned to the mm10 genome using Bowtie 2 (v2.3.4.3)[81]. Reads with mapq > 30 were retained using SAMtools (v1.9)[82]. Peak calling was performed with MACS2 (v2.1.1.20160309)[83] using default parameters. Differential binding analysis was performed with the DiffBind package (v3.12)[84] using the following parameters: minOverlap = 2 and summits = FALSE for count calculation and minMembers = 2 for contrast generation. Profile plots were generated using deepTools (v3.5.0)[85] and visualized with Integrative Genome Viewer (v2.17.4)[86].

snRNA-seq analysis

For the reanalysis of snRNA-seq data, processed expression matrices were downloaded from GSE158843 (ref. 3) and analyzed in R (v4.5; R Core Team, 2021) using Seurat (v5.4.0)[87]. Sample matrices were assigned metadata, including the original sample identifier and whether the hippocampal hemisphere had been virally injected with Cre. Control samples and Cre^+ samples were merged separately and assessed for viral expression to exclude Cre^+ cells in the control and to exclude Cre^- cells in the Cre^+ samples. Matrices were merged, and cells were then preprocessed for RNA quantity, number of RNA species and mitochondrial reads. RNA from merged matrices were then normalized, queried for variable features and scaled and centered. Principal component analysis was performed for 100 principal components (PCs) that were then tested for significance of contribution through JackStraw testing. Of those 100 PCs, 67 were found to be significant when compared with a randomized shuffle. Thus, when performing *k*-nearest neighbors, we included those 67 PCs for dimensionality reduction. Default Leiden clustering was then performed using the Annoy algorithm, followed by additional uniform manifold approximation and projection (UMAP) reduction of PC space using the first 67 PC dimensions. Matrices were finally merged using default Harmony algorithm[88] to correct PCs for sample-dependent variance, and samples were reprocessed for *k*-nearest neighbors, Leiden clustering and UMAP reduction. Harmonized clusters were assigned cell types by first determining DEGs of each harmonized cluster using a Model-based Analysis of Single-cell Transcriptomics[89] to iteratively compare each cluster to all other clusters. DEGs were thresholded by requiring a minimum of 25% of cells in the cluster to express a 0.25 log_2(FC) increase compared with all other cells. We then assessed the list of DEGs using markers from the literature for all cell types, for example, CA1 (Pou3f1, Satb2), CA3 (Grik4)[90] and DG (Prox1)[91]. All cell identities were corroborated with the Allen Brain Mouse Cell Type Atlas[92]. We then performed Wilcoxon rank-sum test with Bonferroni multiple comparisons correction to perform differential gene expression between FFJ-WT and FFJ-KO nuclei using default 'FindMarkers' function. Plots were generated using scCustomize on Zenodo (v3.2.4)[93] and SeuratExtend (v1.2.1)[94].

Statistical analyses

All statistical tests were performed in Prism 10 (GraphPad). Outliers were identified using the ROUT method, with $Q = 1$. Normality of data was assessed using Kolmogorov–Smirnov tests. Normally distributed data were analyzed using a Student's *t*-test in the case of equal variances between groups and a Welch's *t*-test in the case of unequal variance (>2-fold difference in s.d. between groups). For nonparametric data, a Mann–Whitney *U* test was used. For data containing three experimental groups, a one-way analysis of variance (ANOVA) followed by Tukey's post hoc tests was used, or a Brown–Forsythe ANOVA followed by Dunnett's multiple comparisons tests if the assumption of sphericity was not met. The synaptic densities shown in Figs. 4h and 7n were analyzed using a single one-way ANOVA, as they share control groups. For these figures, rescue experiments were performed after the initial knockdown experiment was completed. When performing the rescue experiments, some animals were injected with shLacZ and shFezf2 to verify that baseline Syt2 density values for these groups were comparable to the original dataset. The distribution of these is shown in Extended Data Fig. 9g. The luciferase assay was analyzed using a two-way ANOVA followed by Fisher's LSD test. Nonparametric data were analyzed using a Mann–Whitney *U* test. For in vitro validation of shRNA sequences, each sequence was compared with *shLacZ* using a *t*-test and Bonferroni correction was applied. For analysis of the correlation of RNA signal values in the *Fezf2* overexpression experiments, Pearson correlation was used. To assess the Fraction of $CTIP^+$/GFP^+ cells, a chi-square test was used. A mixed-effects analysis was used to assess the effect of the experimental group on Sholl analysis values. *P* values of <0.05 were considered statistically significant. All data are presented as mean ± s.e.m. All statistical analyses are shown in the Supplementary Table 2. No statistical methods were used to predetermine sample sizes, but our sample sizes are similar to those reported in previous publications[11,26,95].

Reporting summary

Further information on research design is available in the Nature Portfolio Reporting Summary linked to this article.

Data availability

Sequencing data have been deposited at the National Center for Biotechnology Information BioProjects Gene Expression Omnibus and are accessible through Gene Expression Omnibus Series accessions GSE247075 and GSE285372. The data used and generated in this study are openly available from King's College London research data public repository KORDS at https://doi.org/10.18742/32736761. All constructs generated in this study will be shared by the lead contact upon request. Source data are provided with this paper.

Code availability

All the analyses were performed using existing published code (Methods), which is available from the corresponding author upon request.

References

71. Selten, M. et al. Regulation of PV interneuron plasticity by neuropeptide-encoding genes. *Nature* **643**, 173–181 (2025).
72. Moissidis, M. et al. A postnatal molecular switch drives activity-dependent maturation of parvalbumin interneurons. *Cell* **188**, 5555–5575 (2025).

73. Schindelin, J. et al. Fiji: an open-source platform for biological-image analysis. *Nat. Methods* **9**, 676–682 (2012).
74. Arshadi, C., Günther, U., Eddison, M., Harrington, K. I. S. & Ferreira, T. A. SNT: a unifying toolbox for quantification of neuronal anatomy. *Nat. Methods* **18**, 374–377 (2021).
75. Wang, L., Wang, S. & Li, W. RSeQC: quality control of RNA-seq experiments. *Bioinformatics* **28**, 2184–2185 (2012).
76. Dobin, A. et al. STAR: ultrafast universal RNA-seq aligner. *Bioinformatics* **29**, 15–21 (2013).
77. Love, M. I., Huber, W. & Anders, S. Moderated estimation of fold change and dispersion for RNA-seq data with DESeq2. *Genome Biol.* **15**, 550–550 (2014).
78. Liao, Y., Wang, J., Jaehnig, E. J., Shi, Z. & Zhang, B. WebGestalt 2019: gene set analysis toolkit with revamped UIs and APIs. *Nucleic Acids Res.* **47**, W199–W205 (2019).
79. Yao, Z. et al. A taxonomy of transcriptomic cell types across the isocortex and hippocampal formation. *Cell* **184**, 3222–3241 (2021).
80. Krueger, F. Trim Galore! *Babraham Bioinformatics* https://www.bioinformatics.babraham.ac.uk/projects/trim_galore (2015).
81. Langmead, B. & Salzberg, S. L. Fast gapped-read alignment with Bowtie 2. *Nat. Methods* **9**, 357–359 (2012).
82. Li, H. et al. The sequence alignment/map format and SAMtools. *Bioinformatics* **25**, 2078–2079 (2009).
83. Zhang, Y. et al. Model-based analysis of ChIP–seq (MACS). *Genome Biol.* **9**, R137 (2008).
84. Ramírez, F. et al. deepTools2: a next generation web server for deep-sequencing data analysis. *Nucleic Acids Res.* **44**, W160–W165 (2016).
85. Ross-Innes, C. S. et al. Differential oestrogen receptor binding is associated with clinical outcome in breast cancer. *Nature* **481**, 389–393 (2012).
86. Thorvaldsdóttir, H., Robinson, J. T. & Mesirov, J. P. Integrative Genomics Viewer (IGV): high-performance genomics data visualization and exploration. *Brief. Bioinformatics* **14**, 178–192 (2013).
87. Hao, Y. et al. Dictionary learning for integrative, multimodal and scalable single-cell analysis. *Nat. Biotechnol.* **42**, 293–304 (2024).
88. Korsunsky, I. et al. Fast, sensitive and accurate integration of single-cell data with Harmony. *Nat. Methods* **16**, 1289–1296 (2019).
89. Finak, G. et al. MAST: a flexible statistical framework for assessing transcriptional changes and characterizing heterogeneity in single-cell RNA sequencing data. *Genome Biol.* **16**, 278 (2015).
90. Tole, S., Christian, C. & Grove, E. A. Early specification and autonomous development of cortical fields in the mouse hippocampus. *Development* **124**, 4959–4970 (1997).
91. Lavado, A., Lagutin, O. V., Chow, L. M. L., Baker, S. J. & Oliver, G. Prox1 is required for granule cell maturation and intermediate progenitor maintenance during brain neurogenesis. *PLoS Biol* **8**, e1000460 (2010).
92. Tasic, B. et al. Adult mouse cortical cell taxonomy revealed by single cell transcriptomics. *Nat. Neurosci.* **19**, 335–346 (2016).
93. Marsh, S. et al. samuel-marsh/scCustomize: release 3.2.4. *Zenodo* https://doi.org/10.5281/zenodo.17900382 (2025).
94. Hua, Y., Weng, L., Zhao, F. & Rambow, F. SeuratExtend: streamlining single-cell RNA-seq analysis through an integrated and intuitive framework. *Gigascience* **14**, giaf076 (2025).
95. Bernard, C. et al. Cortical wiring by synapse type-specific control of local protein synthesis. *Science* **378**, eabm7466 (2022).

Acknowledgements

The authors are thankful to L. Doglio, F. Sanchez-Roman, S. Sanalidou, X. Hu and T. Garces (King's College London) for technical assistance and lab support, and to I. Andrew for mouse management (King's College London). The authors thank the Centre for Genomic Regulation Genomics Core Facility of Barcelona for conducting RNA sequencing. Finally, the authors are grateful to O. Marín, L. Andreae, M. Selten, J. Jézéquel and G. Condomitti (King's College London) for critical reading of the manuscript and to all members of the Rico and Marin laboratories for stimulating discussions and ideas.

Author contributions

T.K. and B.R. conceived and designed the study. T.K. performed most of the experiments and analyses. S.S. and H.Y. performed additional experiments and analyses. T.K. designed and produced the molecular tools, with the help of T.G. and P.M. T.G. and P.M. helped with the in vitro experiments and the AAV virus production. N.A. conducted electrophysiological recordings. R.A., Y.D.-C. and N.F. performed the luciferase experiments and analyses. S.N., B.d.B. and A.B. provided and analyzed the ChIP–seq data. K.D. generated the UMAP visualization of snRNA-seq for triple conditional mouse lines. S.S., T.G. and P.M. helped with the tissue preparation and immunohistochemistry. T.K. and B.R. wrote the manuscript.

Funding

This project was supported by grants from Wellcome Trust (202758/Z/16/Z), Wellcome Discovery (307203/Z/23/Z) and the European Union's Horizon 2020 research and innovation programme (the results leading to this publication have received funding from the Innovative Medicines Initiative 2 Joint Undertaking under grant agreement 777394 for the project AIMS-2-TRIALS. This Joint Undertaking receives support from the European Union's Horizon 2020 research and innovation programme and EFPIA and AUTISM SPEAKS, Autistica, SFARI to B.R.). The funders had no role in study design, data collection and analysis, decision to publish or preparation of the manuscript.

Competing interests

The authors declare no competing interests.

Additional information

Extended data is available for this paper at https://doi.org/10.1038/s41593-026-02515-6.

Supplementary information The online version contains supplementary material available at https://doi.org/10.1038/s41593-026-02515-6.

Correspondence and requests for materials should be addressed to Beatriz Rico.

Peer review information *Nature Neuroscience* thanks the anonymous reviewer(s) for their contribution to the peer review of this work.

Reprints and permissions information is available at www.nature.com/reprints.

https://doi.org/10.1038/s41593-026-02515-6

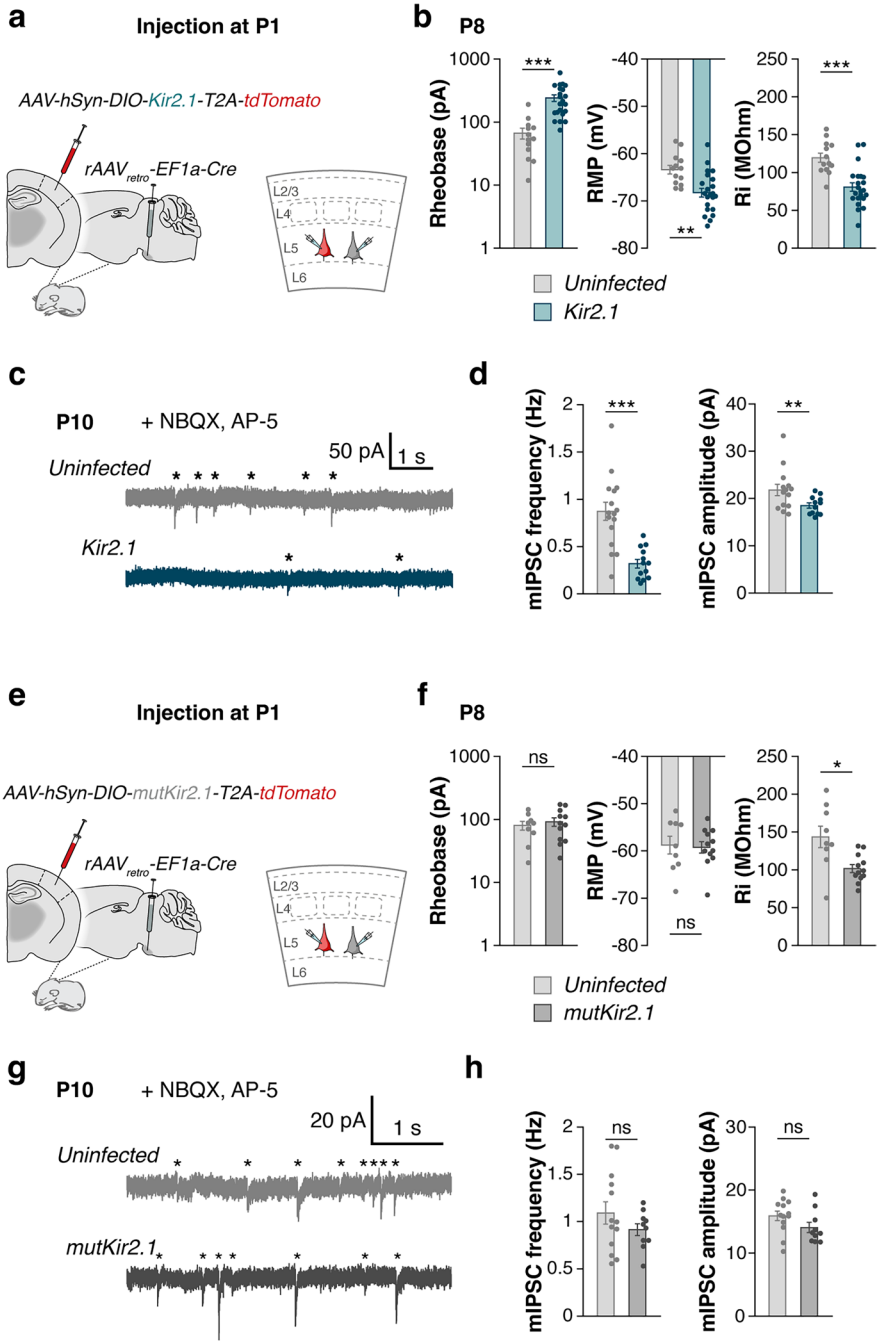

Extended Data Fig. 1 | Expression of Kir2.1 decreases excitability of L5 ET cells. a, Experimental design for decreasing activity by expressing Kir2.1. Uninfected L5 ET cells were identified by their large soma and pronounced sag current, characteristic of these neurons. **b**, Quantification of rheobase, resting membrane potential (RMP) and input resistance (Ri) between Kir2.1-expressing cells and neighboring uninfected cells (uninfected $n = 13$ cells from 6 mice, Kir2.1 $n = 22$ cells from 7 mice. Rheobase, two-tailed Welch's t-test, $^{***}P < 0.0001$; RMP, two-tailed Student's t-test, $^{**}P = 0.0013$; Ri, two-tailed Student's t-test, $^{***}P < 0.0001$). **c**, Example traces of pharmacologically isolated mIPSCs recorded from uninfected and Kir2.1-expressing cells. Asterisks indicate the onset of mIPSC events. **d**, Quantification of mIPSC frequency (uninfected, $n = 16$ cells from 6 mice; Kir2.1, $n = 13$ cells from 6 mice, two-tailed Welch's t-test, $^{***}P < 0.0001$) and amplitude (uninfected, $n = 15$ cells from 6 mice; Kir2.1, $n = 12$ cells from 6 mice, two-tailed Welch's t-test, $^{**}P = 0.0092$). **e**, Experimental design for control experiments using mutKir2.1. **f**, Quantification of rheobase, RMP and Ri between mutKir2.1-expressing cells and neighboring uninfected cells (uninfected, $n = 9$ cells from 4 mice, mutKir2.1, $n = 12$ cells from 4 mice. Rheobase, two-tailed Student's t-test, $P = 0.58$; RMP, two-tailed Student's t-test, $P = 0.83$; Ri, two-tailed Student's t-test, $^{*}P = 0.0199$). **g**, Example traces of pharmacologically isolated mIPSCs recorded from uninfected and mutKir2.1-expressing cells. Asterisks indicate the onset of mIPSC events. **h**, Quantification of mIPSC frequency (uninfected, $n = 13$ cells from 7 mice; mutKir2.1, $n = 10$ cells from 4 mice, two-tailed Welch's t-test, $P = 0.21$) and amplitude (uninfected, $n = 13$ cells from 7 mice; mutKir2.1, $n = 10$ cells from 3 mice, two-tailed Student's t-test, $P = 0.11$). Data are mean ± s.e.m. ns, not significant. See Supplementary Table 2.

https://doi.org/10.1038/s41593-026-02515-6

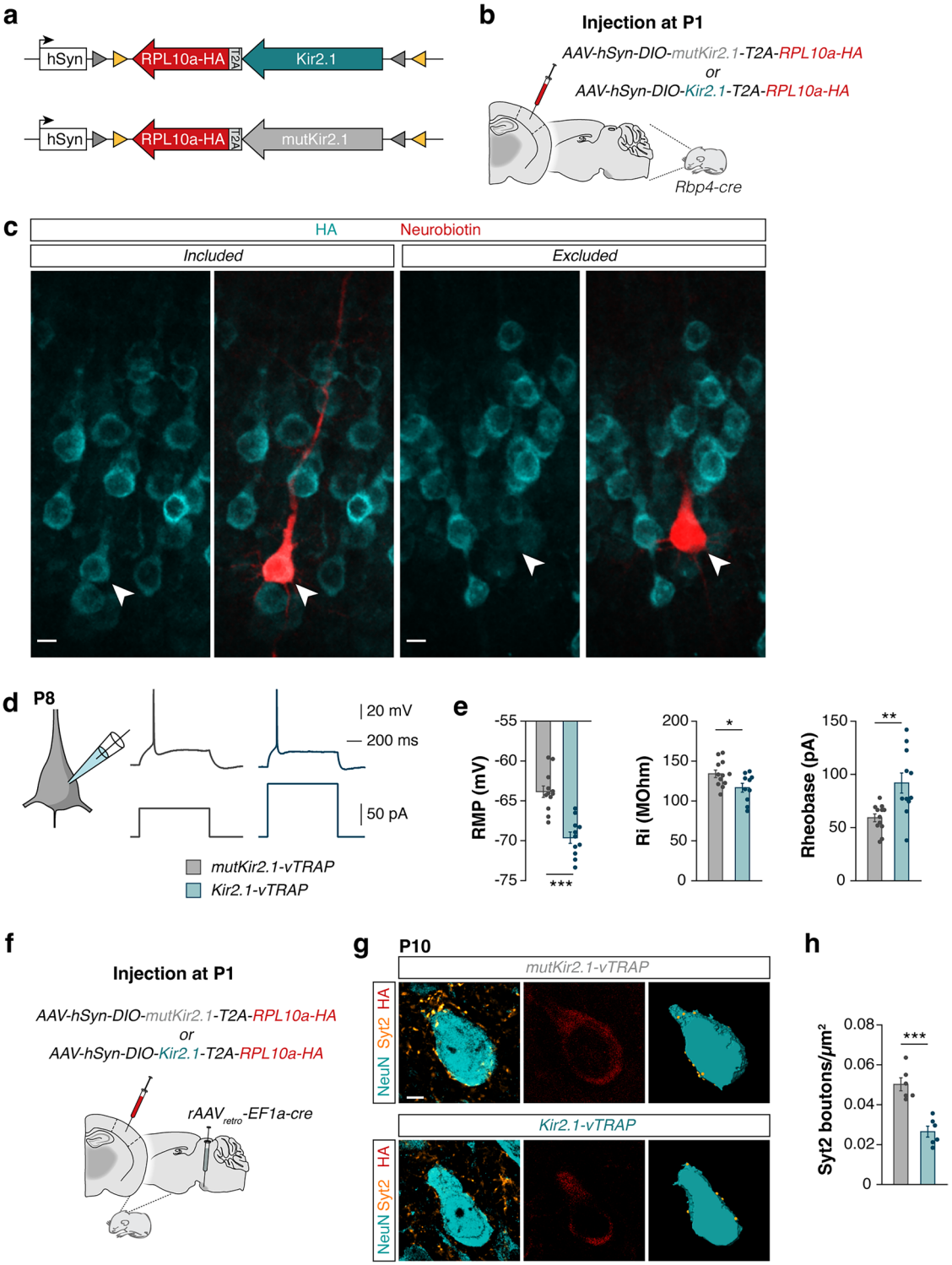

Extended Data Fig. 2 | Kir2.1-vTRAP is functional and decreases the density of perisomatic Sty2⁺ boutons. a, Schematic representation of the Cre-dependent Kir2.1-T2A-Rpl10a-HA (Kir-vTRAP) construct. **b**, Experimental design. **c**, Apotome images showing immunohistochemical staining against HA and fluorophore-conjugated streptavidin staining of neurobiotin in infected (left) and uninfected (right) recorded cells (arrowheads). Performed for each cell quantified in **e**. **d**, Example traces of the first current injection to elicit an action potential in mutKir2.1-vTRAP and Kir2.1-vTRAP-infected cells. **e**, Quantification of resting membrane potential (RMP; mutKir2.1-vTRAP, $n = 12$ cells from 2 mice; Kir2.1-vTRAP, $n = 11$ cells from 2 mice, two-tailed Student's t-test, $^{***}P < 0.0001$), input resistance (Ri; mutKir2.1-vTRAP, $n = 12$ cells from 2 mice; Kir2.1-vTRAP, $n = 10$ cells from two mice, two-tailed Student's t-test, $^{*}P = 0.0262$) and rheobase (mutKir2.1-vTRAP, $n = 12$ cells from 2 mice; Kir2.1-vTRAP, $n = 11$ cells from 2 mice, two-tailed Welch's t-test, $^{**}P = 0.0066$). **f**, Experimental design. **g**, Single-plane confocal images showing presynaptic Syt2 puncta (yellow), NeuN (cyan) and HA (red). Right panel: three-dimensional Imaris reconstruction of the soma and Syt2 puncta. **h**, Quantification of the density of Syt2 puncta close to the somata of cell infected with mutKir2.1-vTRAP or Kir2.1-vTRAP (mutKir2.1-vTRAP, $n = 6$ mice; Kir2.1-vTRAP, $n = 6$ mice, two-tailed Student's t-test, $^{***}P = 0.0002$). Data are mean ± s.e.m., ns, not significant. Scale bars, 10 µm (**c**), 5 µm (**g**). See Supplementary Table 2.

https://doi.org/10.1038/s41593-026-02515-6

a

Samples	# Reads	% Uniquely mapped	# Detected genes	% mRNA	% Junctions
MutKir_2	131 263 260	90.06	13 350	81.68	54
MutKir_3	134 705 587	89.97	13 165	79.39	53
Kir_1	126 129 797	90.18	13 717	81.35	51
Kir_2	133 510 083	89.93	13 446	81.71	53
Kir_3	133 401 340	91.74	13,414	80.58	52

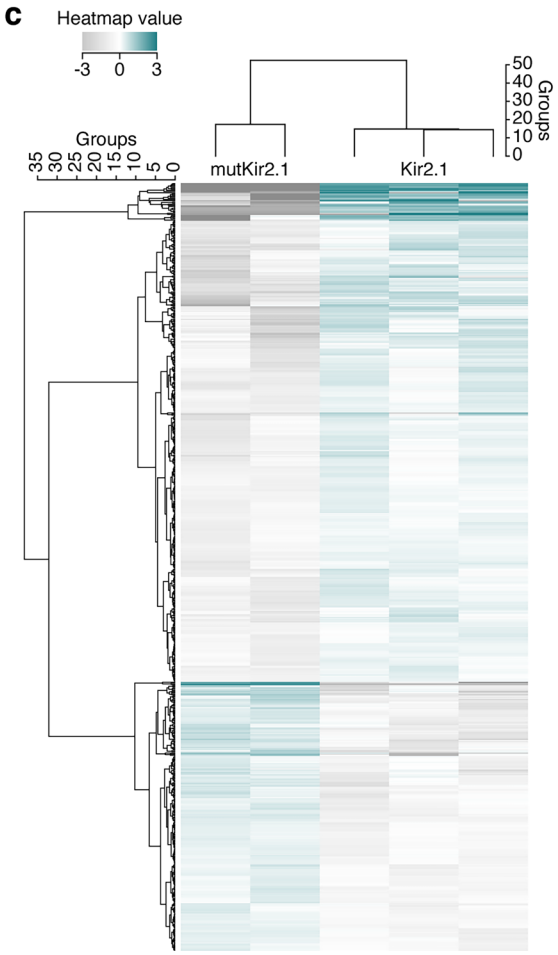

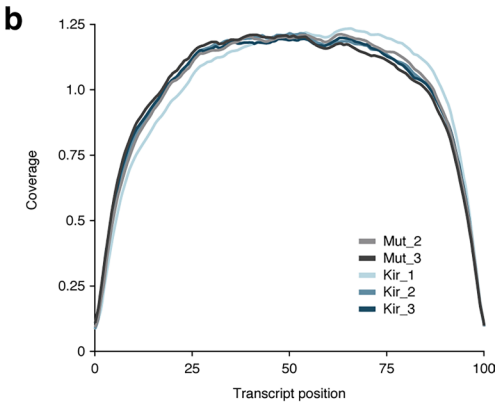

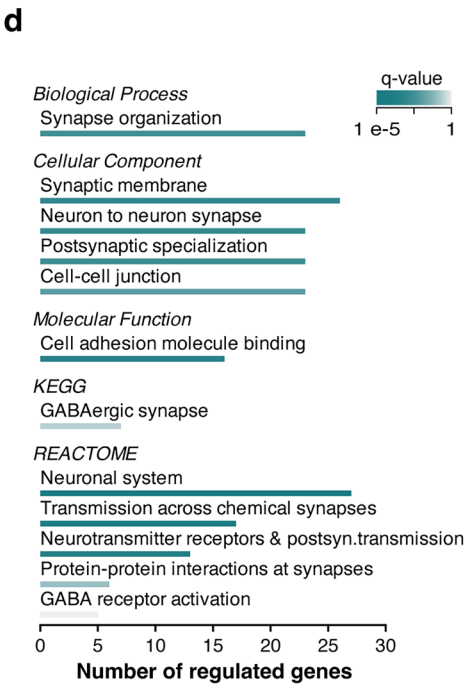

Extended Data Fig. 3 | RNA sequencing quality control and analysis. a, FastQC analysis of RNA sequencing data for each replicate, showing the total number of reads, the percentage of reads uniquely mapped to the reference genome, the number of detected genes, the percentage of mRNA and the percentage of reads mapped to exon-exon junctions. **b**, 5′ to 3′ coverage plot showing the percentage of read bases across the transcript length. **c**, Heatmaps showing DESeq2-normalized counts from each replicate of DEGs. **d**, Selected GO terms significantly enriched in the dataset of differentially regulated genes in ET neurons expressing Kir2.1 compared with mutKir2.1 controls. Headers indicate GO domain/database. Color indicates the *q*-value, and the length of the bar indicates the number of regulated genes within the GO term.

https://doi.org/10.1038/s41593-026-02515-6

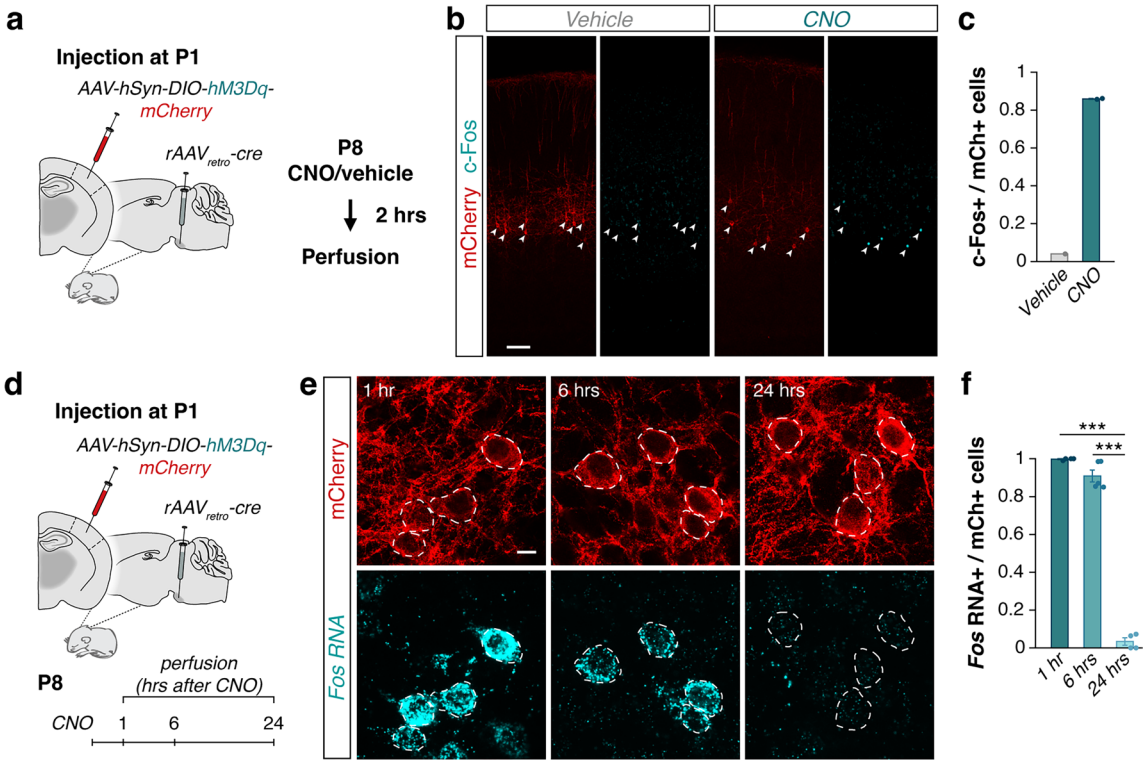

Extended Data Fig. 4 | Validation of hM3Dq function. a, Experimental setup. Mice were perfused 2 h after a single injection of CNO or vehicle. **b**, Confocal images showing hM3Dq-expressing cells (arrowheads; mCherry, red) and CFOS (cyan). **c**, Quantification of the fraction of hM3D1-expressing cells expressing CFOS after injection of CNO (86%, 2 mice) or vehicle (4%, 1 mouse). **d**, Experimental design for increasing activity with DREADDs in L5 ET cells. Mice were perfusion fixed at 1, 6 and 24 h after a single CNO injection. **e**, Confocal images showing *Fos* RNA expression (cyan) in hM3Dq-expressing L5 ET cells (mCherry, red) 1 h, 6 h and 24 h after CNO injection. **f**, Quantification of the proportion of hM3Dq-expressing cells that contain above-background levels of *Fos* RNA (1 h, 99.8%, n = 4 mice; 6 h, 91.0%, n = 5 mice; 24 h, 3.4%, n = 4 mice, Welch ANOVA, two-sided, $^{***}P < 0.0001$, Dunnett's post hoc tests, 1 h versus 6 h, $P = 0.12$; 1 h versus 24 h, $^{***}P < 0.0001$; 6 h versus 24 h, $^{***}P < 0.0001$). Data are mean ± s.e.m. Scale bars, 5 µm (**b** and **e**). See Supplementary Table 2.

https://doi.org/10.1038/s41593-026-02515-6

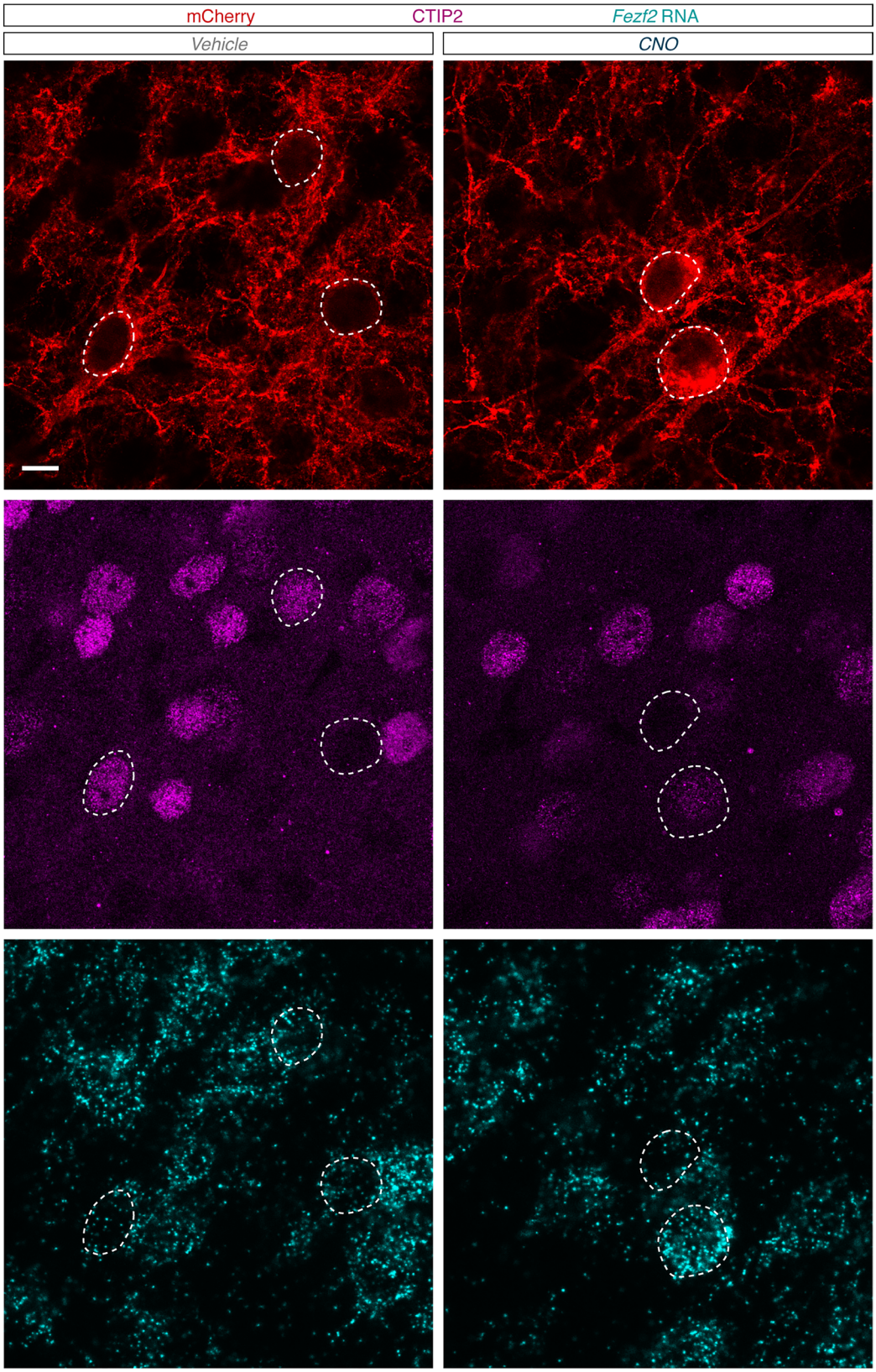

Extended Data Fig. 5 | *Fezf2* is regulated by activity specifically in CTIP2 + L5 neurons. Example low-magnification confocal images showing *Fezf2* RNA levels in CTIP2^{+} and CTIP2^{-} L5 ET cells, relating to Fig. 3g–i. 7 replicates in each group; quantified in Fig. 3h,i. Scale bar, 10 µm.

https://doi.org/10.1038/s41593-026-02515-6

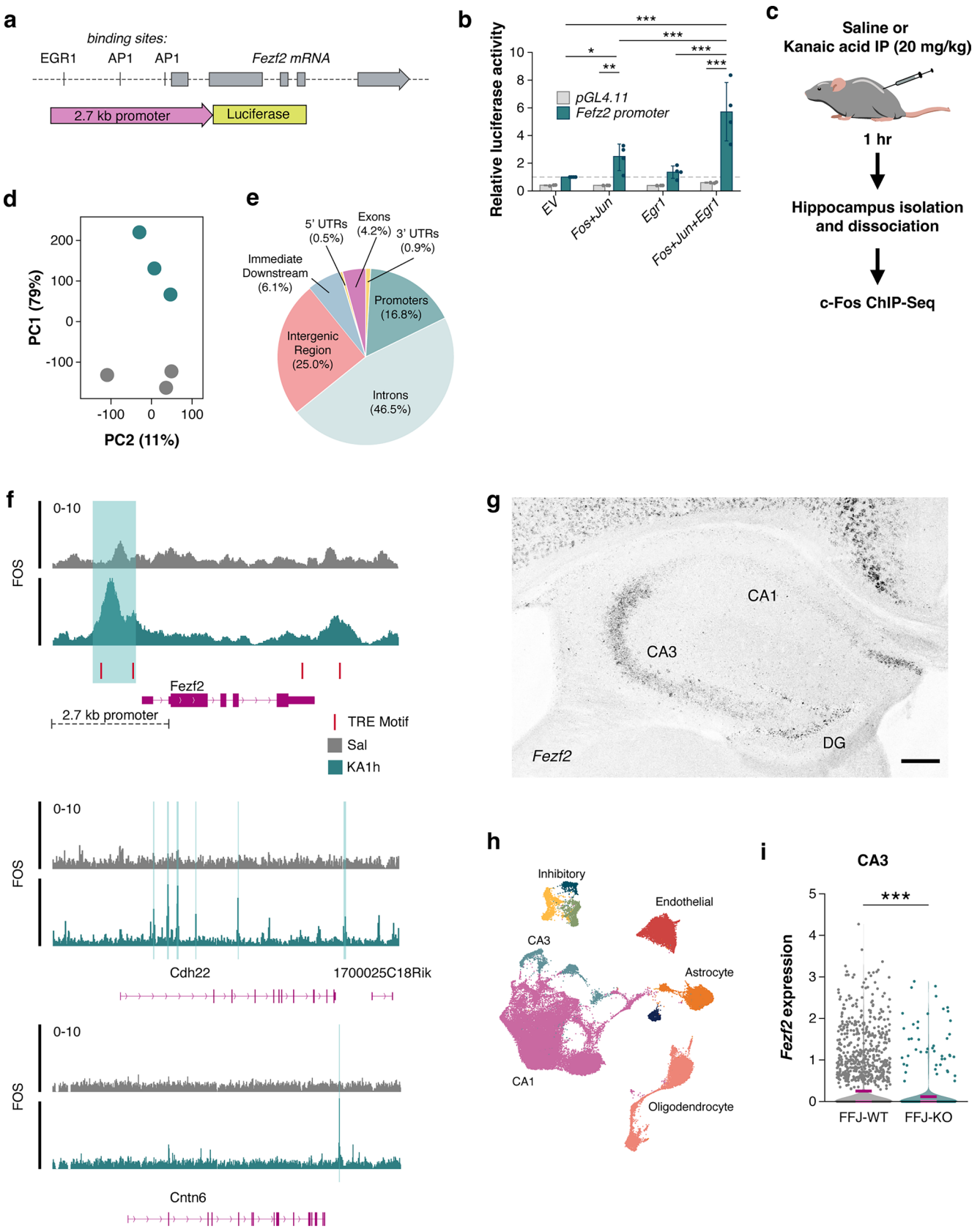

Extended Data Fig. 6 | See next page for caption.

https://doi.org/10.1038/s41593-026-02515-6

Extended Data Fig. 6 | c-Fos binds to the *Fezf2* promoter region in vivo and activates gene expression. a, Schematic showing the 2.7 kb *Fezf2* promoter region containing two putative AP-1 and one putative EGR1 binding sites. **b**, Analysis of the activation of *Fezf2* promoter by c-Fos, Jun and EGR1 in HEK293T cells. Values are normalized to the empty vector/*Fezf2* promoter group. $n = 3$ replicates for all pGL4.11 groups and 4 replicates for all *Fezf2* promoter groups. Two-way ANOVA: promoter, $P < 0.0001$; transcription factor, $P = 0.0002$; interaction, $P = 0.0007$. Tukey post hoc tests**:** comparing *pGL4.11* versus *Fezf2*: Fos + Jun, $^{**}P = 0.0091$; Fos + Jun + Egr1, $^{***}P < 0.0001$. Comparing within *Fezf2*: EV versus Fos + Jun, $^{*}P = 0.0389$; EV versus Fos + Jun + Egr1, $^{***}P < 0.0001$; Fos + Jun versus Fos + Jun + Egr1, $^{***}P < 0.0001$; Egr1 versus Fos + Jun + Egr1, $^{***}P < 0.0001$. All other comparisons are not significant. EV: TF expression empty vector. Data are mean ± s.e.m. **c**, Experimental setup. Mice were injected with KA to elicit strong neuronal activation. One hour after injection, hippocampi were dissected and nuclei isolated, and ChIP–seq was performed. **d**, Principal component analysis (PCA) clearly separated KA- and saline-treated replicates, confirming biological reproducibility. **e**, Genome-wide, FOS binding was enriched at intronic regions (46.5%) and intergenic regions (25%), with approximately 17% of peaks located at promoters. **f**, ChIP–seq analysis shows that Fos binds the *Fezf2* promoter region upon neuronal activity, while *Cdh22* shows intronic binding sites and *Cntn6* shows no binding within the locus or promoter region itself (shaded areas, *Fezf2*: chr14: 12345952–12346943, nosummit: fold = 1.47, summit: fold = 2.196; *Cdh22*: chr2: 165215244–165216019, fold = 1.05; chr2: 165206982–165208118, fold = 1.75; chr2: 165201491–165202613, fold = 1.28; chr2: 165191268–165191813, fold = 2.08; chr2: 165166964–165167585, fold = 2.04; chr2: 165105535–165107038, fold = 1.05; *Cntn6*: chr6: 104890045–104891957, fold = 2.37. mm10; vehicle, $n = 3$ mice; KA, $n = 3$ mice; FDR < 0.001). **g**, *Fezf2* RNAscope signal showing expression of *Fezf2* enriched in the CA3 region of the hippocampus (1 replicate). **h**, UMAP visualization of nuclei from control and Cre^{+} triple conditional knockout mouse line *Fos*$^{fl/fl}$;*Fosb*$^{fl/fl}$;*Junb*$^{fl/fl}$ (FFJ-WT and FFJ-KO, respectively) snRNA-seq with cell type information. **i**, Violin plot showing expression of *Fezf2* in control (FFJ-WT) and Cre^{+} (FFJ-KO) nuclei from CA3 (FFJ-WT, $n = 2405$ cells from 3 mice; $n =$ FFJ-KO, 552 cells from 3 mice; Bonferroni-corrected Mann–Whitney *U* test, two-sided, ***P < 0.0001). Magenta bar shows the mean, light pink bar shows the median. TRE, TPA response element motif; Sal, saline; KA1h 1 h after KA injection. See Supplementary Table 2. Scale bar, 200 µm (**g**).

https://doi.org/10.1038/s41593-026-02515-6

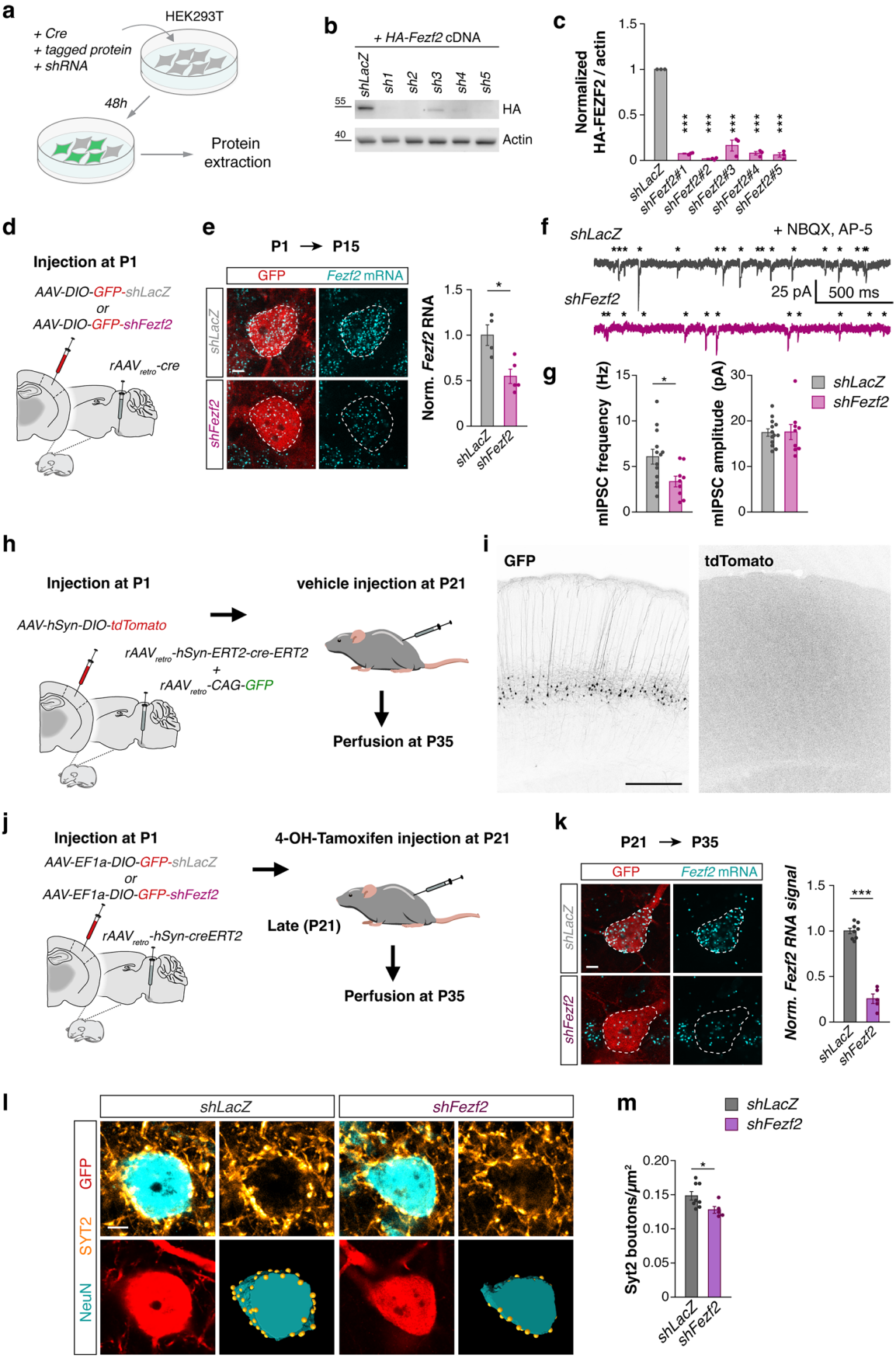

Extended Data Fig. 7 | See next page for caption.

https://doi.org/10.1038/s41593-026-02515-6

Extended Data Fig. 7 | Validation of *Fezf2* shRNA sequences and synaptic assessment of early and late *Fezf2* knockdown. a, Experimental setup for in vitro testing of shRNA sequences. **b**, Western blot of HA-tagged FEZF2 purified from HEK cells transfected with *HA-Fezf2* cDNA and plasmids encoding either *shLacZ* or one of five shRNAs against *Fezf2*. **c**, Quantification of protein signal normalized to actin, relative to controls transfected with *shLacZ* (n = 3 wells per sequence, Bonferroni-corrected two-tailed Student's *t*-test versus shLacZ: shFezf2#1, ***$P < 0.0001$; shFezf2#2, ***$P < 0.0001$; shFezf2#3, ***$P = 0.0002$; shFezf2#4, ***$P < 0.0001$; shFezf2#5, ***$P < 0.0001$). **d**, Experimental design for knockdown of *Fezf2* expression in L5 ET cells. **e**, Left, confocal images showing *Fezf2* RNAscope signal (cyan) and GFP (red) signal in the *Fezf2* knockdown. Right, quantification of *Fezf2* RNAscope signal in the *Fezf2* knockdown compared with controls (*shLacZ*, $n = 4$ mice; *shFezf2*, $n = 5$ mice, two-tailed Student's *t*-test, *$P = 0.0113$). **f**, Example traces showing pharmacologically isolated mIPSCs recorded in L5 ET cells infected with either *shLacZ-GFP* (top) or *shFezf2-GFP* (bottom). Asterisks indicate the onset of mIPSC events. **g**, Quantification of mIPSC frequency (*shLacZ*, $n = 13$ cells from 5 mice; *shFezf2*, $n = 9$ cells from 4 mice, two-tailed Student's *t*-test, *$P = 0.0223$) and amplitude (*shLacZ*, $n = 13$ cells from 5 mice; *shFezf2*, $n = 9$ cells from 4 mice, two-tailed Student's *t*-test, $P = 0.94$). **h**, Experimental setup. *rAAV$_{retro}$-hSyn-ERT2-cre-ERT2* was injected into the pontine nuclei at P1, together with rAAV$_{retro}$-CAG-GFP (ratio GFP:Cre 1:5) to control for accurate targeting of injections. A Cre-dependent AAV expressing tdTomato was injected into the cerebral cortex. Vehicle was injected intraperitonially at P21. Mice were perfusion fixed at P35, and expression of tdTomato and GFP was assessed. **i**, Confocal images showing GFP and tdTomato. In all 3 mice assessed, a strong GFP signal was observed, indicating correct targeting of the pontine nuclei, and no tdTomato signal was detected. **j**, Experimental design for knockdown of Fezf2 expression from P21 onwards. **k**, Left, confocal images showing *Fezf2* RNAscope signal (cyan) and tdTomato (red) signal in the *Fezf2* knockdown from P21 to P35. The dotted line indicates the outline of the soma, drawn from tdTomato signal. Right, quantification of *Fezf2* RNAscope signal in the *Fezf2* knockdown from P21 to P35 compared with controls (*shLacZ*, $n = 8$ mice; *shFezf2*, $n = 5$ mice, two-tailed Student's *t*-test, ***$P < 0.0001$). **l**, Single-plane confocal images showing presynaptic Syt2 puncta (yellow), NeuN (cyan) and GFP (red). Bottom right, 3-dimensional Imaris reconstruction of the soma and Syt2 puncta. **m**, Quantification of the density of Syt2 puncta onto the soma (*shLacZ*, $n = 8$ mice; *shFezf2*, $n = 5$ mice, two-tailed Student's *t*-test, *$P = 0.0432$). Data are mean ± s.e.m. See Supplementary Table 2. Scale bars, 5 µm (**e**, **k** and **l**).

https://doi.org/10.1038/s41593-026-02515-6

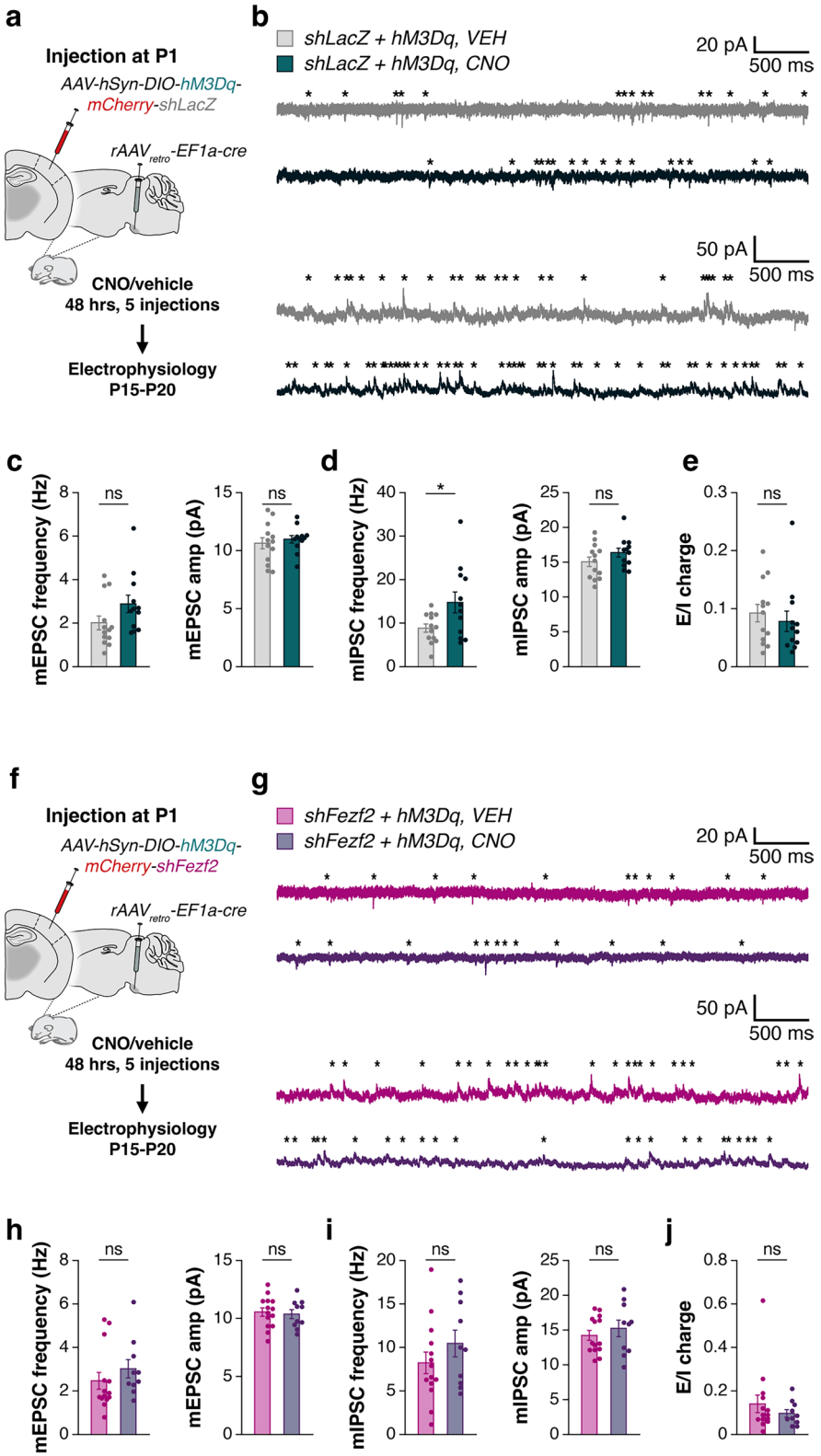

Extended Data Fig. 8 | See next page for caption.

https://doi.org/10.1038/s41593-026-02515-6

Extended Data Fig. 8 | Knockdown of *Fezf2* expression precludes the activity-dependent increase in inhibitory inputs. a, Experimental design. **b**, Example traces showing mEPSCs (top) and mIPSCs (bottom) recorded from L5 ET cells expressing hM3Dq and *shLacZ* from P15-20 mice injected five times with either vehicle (gray) or CNO (dark teal) across 48 h immediately before recording. Asterisks indicate the onset of miniature events. **c**, Quantification of mEPSC frequency (vehicle, $n = 13$ cells from 9 mice; CNO, $n = 12$ cells from 7 mice, two-tailed Student's t-test, $P = 0.10$) and amplitude (vehicle, $n = 13$ cells from 9 mice; CNO, $n = 12$ cells from 7 mice, two-tailed Student's t-test, $P = 0.57$). **d**, Quantification of mIPSC frequency (vehicle, $n = 13$ cells from 9 mice; CNO, $n = 12$ cells from 7 mice, two-tailed Welch's t-test, $^*P = 0.038$) and amplitude (vehicle, $n = 13$ cells from 9 mice; CNO, $n = 12$ cells from 7 mice, two-tailed Student's t-test, $P = 0.18$). **e**, Quantification of the ratio of the charge per second of mEPSCs and mIPSCs (vehicle, $n = 13$ cells from 9 mice; CNO, $n = 12$ cells from 7 mice, two-tailed Student's t-test, $P = 0.55$). **f**, Experimental design. **g**, Example traces showing mEPSCs (top) and mIPSCs (bottom) recorded from L5 ET cells expressing hM3Dq and *shFezf2* from P15-20 mice injected five times with either vehicle (magenta) or CNO (purple) across 48 h immediately before recording. Asterisks indicate the onset of miniature events. **h**, Quantification of mEPSC frequency (vehicle, $n = 14$ cells from 5 mice; CNO, $n = 10$ cells from 5 mice, two-tailed Student's t-test, $P = 0.35$) and amplitude (vehicle, $n = 14$ cells from 5 mice; CNO, $n = 10$ cells from 5 mice, two-tailed Student's t-test, $P = 0.75$). **i**, Quantification of mIPSC frequency (vehicle, $n = 14$ cells from 5 mice; CNO, $n = 10$ cells from 5 mice, two-tailed Student's t-test, $P = 0.26$) and amplitude (vehicle, $n = 14$ cells from 5 mice; CNO, $n = 10$ cells from 5 mice, two-tailed Student's t-test, $P = 0.44$). **j**, Quantification of the ratio of the charge per second of mEPSCs and mIPSCs (vehicle, $n = 14$ cells from 5 mice; CNO, $n = 10$ cells from 5 mice, two-tailed Welch's t-test, $P = 0.33$). See Supplementary Table 2.

https://doi.org/10.1038/s41593-026-02515-6

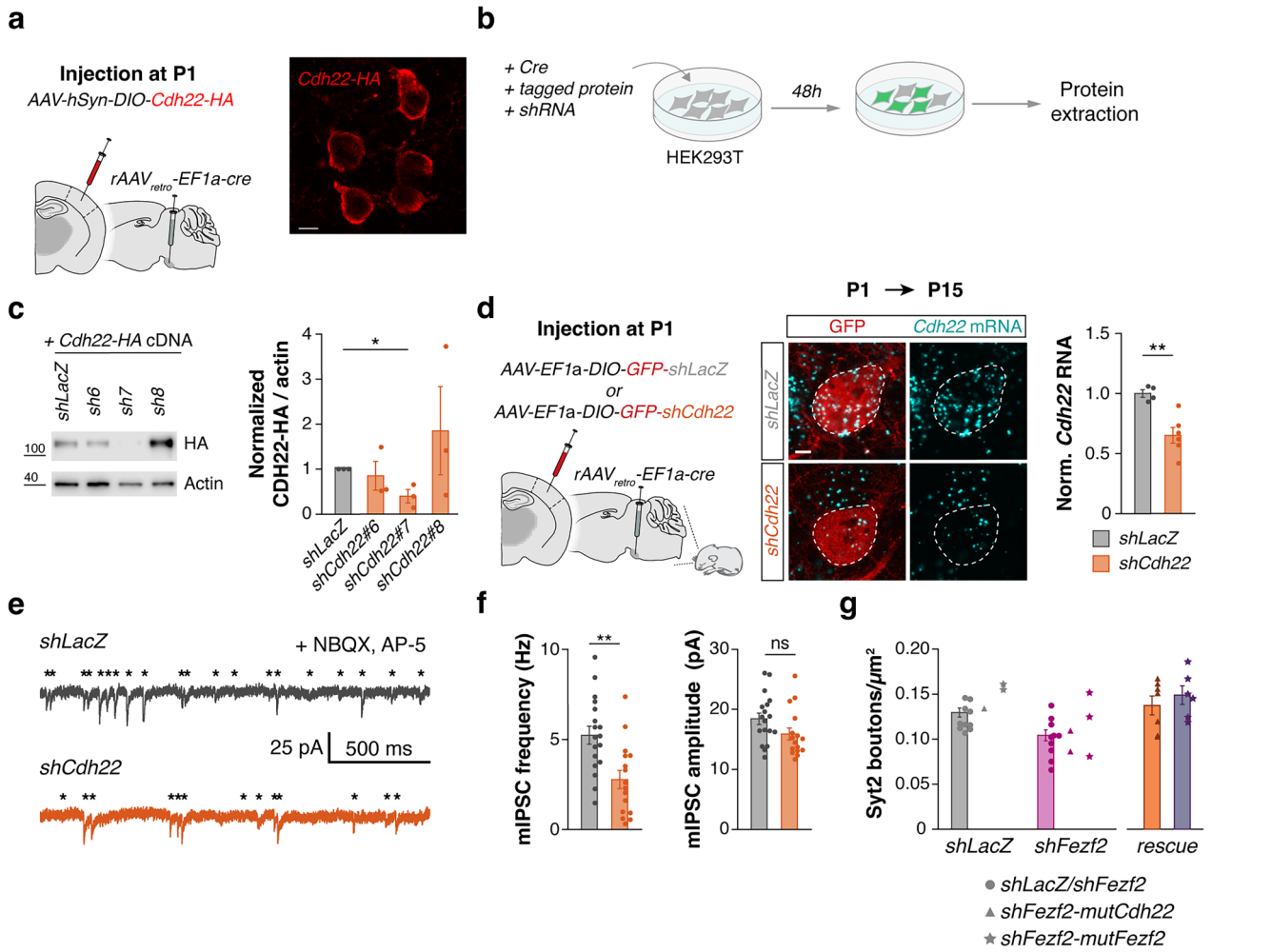

Extended Data Fig. 9 | Validation of *Cdh22* shRNA sequences and confirmation of the synaptic phenotype upon *Cdh22* downregulation. a, Overexpression of *Cdh22*-HA via infection with *AAV-hSyn-DIO-Cdh22-HA* leads to diffuse HA-signal at the plasma membrane, which is restricted to soma and proximal dendrites (2 replicates). Left, experimental design. Right, confocal images showing HA immunohistochemistry signal (red). **b**, Experimental setup for in vitro testing of shRNA sequences. **c**, Left, western blot of HA-tagged CDH22-HA purified from HEK cells transfected with *Cdh22-HA* cDNA and plasmids encoding either *shLacZ* or one of five shRNAs against *Cdh22*. Right, quantification of protein signal normalized to actin, relative to controls transfected with *shLacZ* (n = 3 wells per sequence, Bonferroni-corrected two-tailed Student's *t*-test versus shLacZ: shCdh22#6, $P = 0.67$; shCdh22#6, $^{*}P = 0.0155$; shCdh22#6, $P = 0.43$). **d**, Left, experimental design. Middle, confocal images showing *Cdh22* RNAscope signal (cyan) and tdTomato (red) signal in the *Cdh22* knockdown. The dotted line indicates the outline of the soma, drawn from tdTomato signal. Scale bar = 5 µm. Right, quantification of *Cdh22* RNAscope signal in the *Cdh22* knockdown compared with controls (*shLacZ*, $n = 4$ mice; *shCdh22*, $n = 6$ mice, two-tailed Welch's *t*-test, $^{**}P = 0.002$). The dotted line indicates the outline of the soma, drawn from tdTomato signal. **e**, Example traces showing pharmacologically isolated mIPSCs recorded in L5 ET cells infected with either *shLacZ* (top) or *shCdh22* (bottom) from P15-17 mice. Asterisks indicate the onset of mIPSC events. **f**, Quantification of mIPSC frequency (*shLacZ*, $n = 18$ cells from 9 mice; *shCdh22*, $n = 16$ cells from 7 mice, Mann–Whitney *U* test, two-sided, $^{**}P = 0.0015$) and amplitude (*shLacZ*, $n = 18$ cells from 9 mice; *shCdh22*, $n = 16$ cells from 7 mice, two-tailed Student's *t*-test, $P = 0.08$). **g**, Representation of data from Figs. 4h and 7n. Colors indicate experimental groups, shape (circles, triangles and stars) indicates the experiment from which the data were derived. See Methods for details. Data are mean ± s.e.m., ns, not significant. See Supplementary Table 2. Scale bars, 10 µm (**a**), 5 µm (**d**).

https://doi.org/10.1038/s41593-026-02515-6

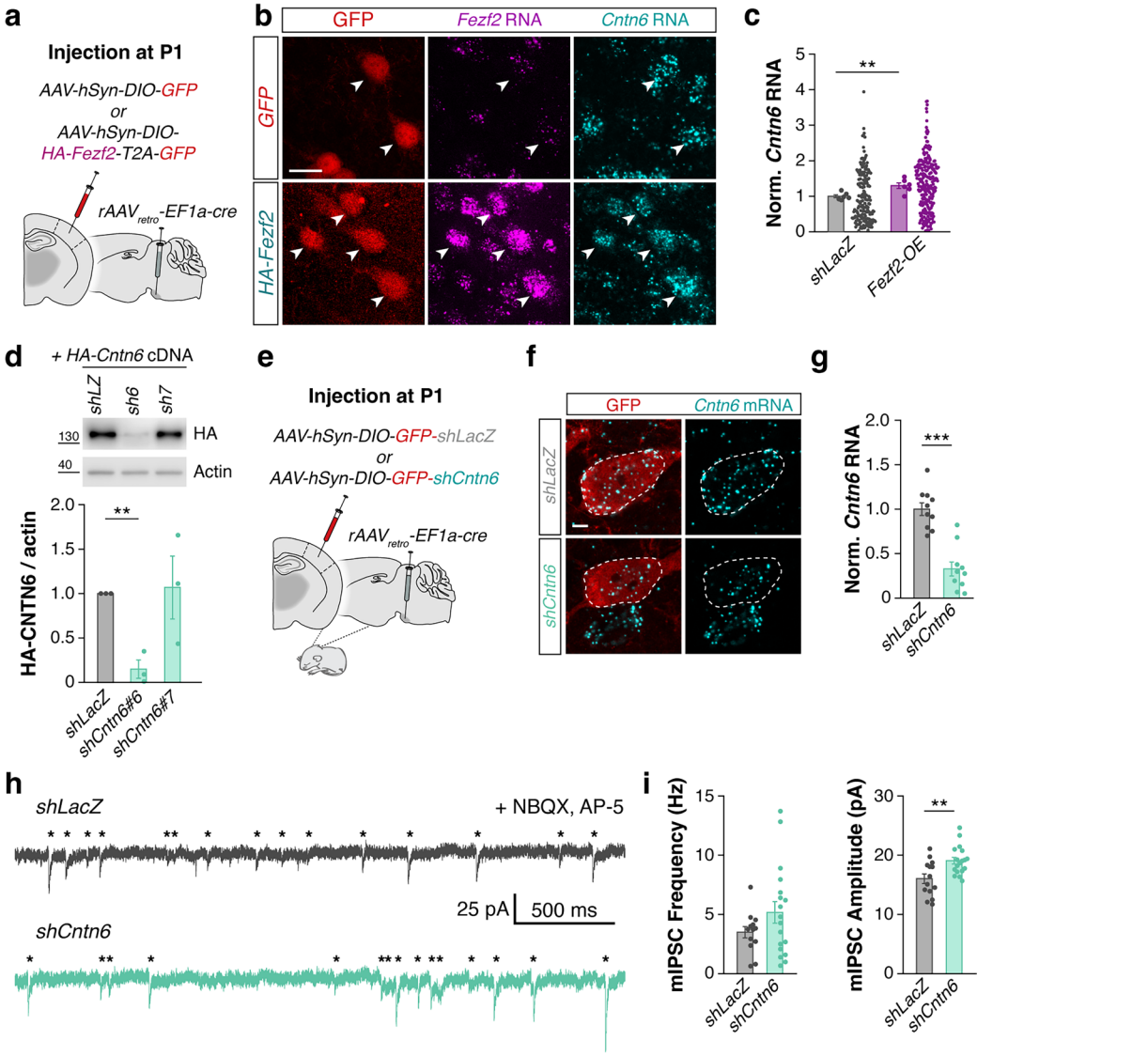

Extended Data Fig. 10 | *Cntn6* does not regulate inhibition downstream of *Fezf2*. **a**, Experimental design of *Fezf2* overexpression. **b**, Confocal images showing GFP reporter (red), *Fezf2* RNA (magenta) and *Cntn6* RNA (cyan signal) in *Fezf2*-overexpressing and GFP-expressing control cells. **c**, Quantification of *Cntn6* RNA signal in ET cells overexpressing *Fezf2* compared with controls (GFP, $n = 6$ mice; Fezf2-overexpression, $n = 6$ mice, two-tailed Student's t-test, $^{**}P = 0.0072$). **d**, In vitro testing of shRNA sequences. Top, western blot of HA-tagged Cntn6 purified from HEK cells transfected with Cntn6-HA cDNA and plasmids encoding *shLacZ* or one of two shRNAs against Cntn6. Bottom, quantification of protein signal normalized to actin, relative to controls transfected with *shLacZ* (n = 3 wells per sequence, Bonferroni-corrected two-tailed Student's t-test versus shLacZ: shCntn6#6, $^{**}P = 0.0012$; shCntn6#7, $P = 0.86$). **e**, Experimental design of *Cntn6* downregulation in L5 ET cells. **f**, Confocal images showing *Cntn6* RNA (cyan) and GFP (red). **g**, Quantification of the downregulation of *Cntn6* between *shCntn6* and controls (*shLacZ*, $n = 10$ mice; *shCntn6*, $n = 10$ mice. $^{***}P = 0.0002$). **h**, Example traces showing pharmacologically isolated mIPSCs recorded in ET-PNs infected with either *shLacZ* (top) or *shCntn6* (bottom) from P15-17 mice. Asterisks indicate the onset of mIPSC events. **i**, Quantification of mIPSC frequency (*shLacZ*, $n = 13$ cells from 9 mice; *shCntn6*, $n = 18$ cells from 9 mice, two-tailed Student's t-test, p = 0.12) and amplitude (*shLacZ*, $n = 14$ cells from 9 mice; *shCntn6*, $n = 18$ cells from 9 mice, two-tailed Student's t-test, $^{**}P = 0.0035$). Dotted lines indicate the outlines of somata drawn from mCherry or GFP signal. Data are mean ± s.e.m., ns, not significant. See Supplementary Table 2. Scale bars, 20 µm (**b**), 5 µm (**f**).

nature portfolio

Corresponding author(s): Beatriz Rico

Last updated by author(s): Sep 12, 2026

Reporting Summary

Nature Portfolio wishes to improve the reproducibility of the work that we publish. This form provides structure for consistency and transparency in reporting. For further information on Nature Portfolio policies, see our Editorial Policies and the Editorial Policy Checklist.

Statistics

For all statistical analyses, confirm that the following items are present in the figure legend, table legend, main text, or Methods section.

n/a	Confirmed
☐	☒ The exact sample size (*n*) for each experimental group/condition, given as a discrete number and unit of measurement
☐	☒ A statement on whether measurements were taken from distinct samples or whether the same sample was measured repeatedly
☐	☒ The statistical test(s) used AND whether they are one- or two-sided *Only common tests should be described solely by name; describe more complex techniques in the Methods section.*
☐	☒ A description of all covariates tested
☐	☒ A description of any assumptions or corrections, such as tests of normality and adjustment for multiple comparisons
☐	☒ A full description of the statistical parameters including central tendency (e.g. means) or other basic estimates (e.g. regression coefficient) AND variation (e.g. standard deviation) or associated estimates of uncertainty (e.g. confidence intervals)
☐	☒ For null hypothesis testing, the test statistic (e.g. *F*, *t*, *r*) with confidence intervals, effect sizes, degrees of freedom and *P* value noted *Give P values as exact values whenever suitable.*
☒	☐ For Bayesian analysis, information on the choice of priors and Markov chain Monte Carlo settings
☒	☐ For hierarchical and complex designs, identification of the appropriate level for tests and full reporting of outcomes
☐	☒ Estimates of effect sizes (e.g. Cohen's *d*, Pearson's *r*), indicating how they were calculated

Our web collection on statistics for biologists contains articles on many of the points above.

Software and code

Policy information about availability of computer code

Data collection

Image Studio Lite LI-COR BioSciences (RRID: SCR_01421)
LAS AF Leica Microsystems (RRID: SCR_013673)
Zeiss ZEN Digital Imaging for Light Microscopy (RRID:SCR_013672)
Molecular Devices pClamp (RRID:SCR_011323)
Multiclamp 700B Commander

Data analysis

Image analysis:
MATLAB MathWorks (RRID:SCR_001622)
Imaris 7.5.2 Bitplane (RRID: SCR_007370)
Fiji (RRID:SCR_002285)

Transcriptomics:

VTRAP transcriptomics
RStudio (RRID:SCR_000432)
R/Bioconductor package DESeq2 R DESeq2 (RRID:SCR_015687)
R/Bioconductor package ClusterProfiler R ClusterProfiler (RRID:SCR_016884)
org.Mm.eg.db org.Mm.eg.db (RRID:SCR_023488)

Single cell transcriptomics:
R/Seurat RRID:SCR_016341

R/SeuratExtend RRID:SCR_026143
R/scCustomize RRID:SCR_024675
R/tidyverse RRID:SCR_019186
R/MAST RRID:SCR_016340

Electrophysiology:
MATLAB MathWorks (RRID:SCR_001622)
SynaptoSoft Mini Analysis Program (RRID:SCR_002184)

Statistical analysis:
GraphPad Prism 10 (RRID:SCR_002798)

All quantification methods using custom scripts are described in Method Details.

For manuscripts utilizing custom algorithms or software that are central to the research but not yet described in published literature, software must be made available to editors and reviewers. We strongly encourage code deposition in a community repository (e.g. GitHub). See the Nature Portfolio guidelines for submitting code & software for further information.

Data

Policy information about availability of data

All manuscripts must include a data availability statement. This statement should provide the following information, where applicable:

- Accession codes, unique identifiers, or web links for publicly available datasets
- A description of any restrictions on data availability
- For clinical datasets or third party data, please ensure that the statement adheres to our policy

All transcriptomic data used will be made publicly available via the Gene Expression Omnibus upon acceptance.

Research involving human participants, their data, or biological material

Policy information about studies with human participants or human data. See also policy information about sex, gender (identity/presentation), and sexual orientation and race, ethnicity and racism.

Reporting on sex and gender	N/A
Reporting on race, ethnicity, or other socially relevant groupings	N/A
Population characteristics	N/A
Recruitment	N/A
Ethics oversight	N/A

Note that full information on the approval of the study protocol must also be provided in the manuscript.

Field-specific reporting

Please select the one below that is the best fit for your research. If you are not sure, read the appropriate sections before making your selection.

☒ Life sciences ☐ Behavioural & social sciences ☐ Ecological, evolutionary & environmental sciences

For a reference copy of the document with all sections, see nature.com/documents/nr-reporting-summary-flat.pdf

Life sciences study design

All studies must disclose on these points even when the disclosure is negative.

Sample size	No statistical method was used to predetermine sample size. Sample sizes were determined empirically according to our previous experiences and the review of similar experiments in literature (Kroon et a., 2019; Favuzzi et al., 2019).
Data exclusions	Statistical outliers were identified using the ROUT Method with Q = 5% (GraphPad 10), and were excluded from the original dataset.
Replication	3 biological replicates per condition were used for RNASeq; one control replicate was discarded during analysis. In order to ensure reproducibility, we provided detailed methods and reported the number of mice and neurons included in each dataset. Experimental and control animals were always littermates. For electrophysiology, slices were obtained from experimental and control littermates simultaneously to reduce any variation introduced by solutions, fluctuations in temperature and time of day. For snRNAseq published data Vehicle injected wildtype mouse hippocampus, n = 3; KA injected Cre+ mouse hippocampus, n = 3 (Yap et al., 2020).

Randomization	Both male and female animals were randomly allocated to experimental groups.
Blinding	Data collection and analysis were performed blind to experimental groups, although for some experiments (e.g. Fezf2 overexpression) blinding was not effective due to the phenotype being readily observable during data collection.

Reporting for specific materials, systems and methods

We require information from authors about some types of materials, experimental systems and methods used in many studies. Here, indicate whether each material, system or method listed is relevant to your study. If you are not sure if a list item applies to your research, read the appropriate section before selecting a response.

Materials & experimental systems

n/a	Involved in the study
☐	☒ Antibodies
☐	☒ Eukaryotic cell lines
☒	☐ Palaeontology and archaeology
☐	☒ Animals and other organisms
☒	☐ Clinical data
☒	☐ Dual use research of concern
☒	☐ Plants

Methods

n/a	Involved in the study
☐	☒ ChIP-seq
☒	☐ Flow cytometry
☒	☐ MRI-based neuroimaging

Antibodies

Antibodies used

Primary antibodies
Mouse anti-NeuN, 1:500 - Sigma-Aldrich MAB377
Rabbit anti-NeuN, 1:500 - Millipore ABN78
Goat anti-mCherry, 1:500 - Antibodies-Online ABIN1440057
Rabbit anti-DsRed, 1:500 - Clontech 632496
Mouse IgG2a anti-Syt2, 1:250 - ZFIN ZDB-ATB-081002-25
Chicken anti-GFP, 1:1000 - Aves Lab GFP-1020
Chicken anti-GFP , 1:1000- Abcam #ab13970
Mouse IgG1 anti-HA, 1:330 - BioLegend #901502
Rabbit anti-CFOS, 1:500 - SySy #AbE 457
Rat anti-HA , 1:500- Roche (Sigma) #11867423001
Rat anti-CTIP2, 1:500 - Abcam #ab18465

Secondary antibodies (all 1:500)

Goat anti-mouse IgG1 488 - Molecular Probes A-21121
Goat anti-chicken 488 - Molecular Probes A-11039
Goat Anti-Rat 555 - Invitrogen #A-21434
Donkey anti-rabbit 488 - Invitrogen #A-21206
Donkey anti-rabbit 555 - Molecular Probes A-31572
Donkey anti-goat 555 - Molecular Probes A-21432
Goat anti-mouse IgG1 555 - Invitrogen #A-21127
Goat anti-mouse IgG2a 647 - Molecular Probes A-21241

Validation

All antibodies were validated by the companies we obtained them from prior to purchase. Additionally, the antibodies have been validated in previous published work (del Pino et al., 2017; Favuzzi et al., 2019; Exposito-Alonso et al., 2020; Bernard et al., 2022; Jezequel et al., 2025).

Eukaryotic cell lines

Policy information about cell lines and Sex and Gender in Research

Cell line source(s)	HEK293FT (female line)) - ThermoScientific # R70007 Cre-expressing HEK293 (female line), Ambion #SC004-BSD
Authentication	None of the cell lines used were authenticated
Mycoplasma contamination	The cell lines were not tested for mycoplasma contamination
Commonly misidentified lines (See ICLAC register)	*Name any commonly misidentified cell lines used in the study and provide a rationale for their use.*

Animals and other research organisms

Policy information about studies involving animals; ARRIVE guidelines recommended for reporting animal research, and Sex and Gender in Research

Laboratory animals	C57BL/6J, Charles River 000664; RRID: IMSR_JAX:000664 Tlx3-Cre (C57BL/6J background), Rico lab (Gerfen, Paletzki, & Heintz, 2013) Rbp4-Cre (C57BL/6J background), Rico lab (Gerfen, Paletzki, & Heintz, 2013) Tlx3-Cre and Rbp4-Cre were maintained in a C57BL/6 background (Charles River Laboratories). After weaning, animals were housed in groups of up to five littermates and maintained under standard, temperature controlled, laboratory conditions. Mice were kept on a 12:12 light/dark cycle and received water and food ad libitum.
Wild animals	The study did not involve wild animals.
Reporting on sex	Both male and female animals were used, results are not displayed according to sex.
Field-collected samples	The study did not involve samples collected from the field.
Ethics oversight	All animal procedures were approved by the ethical committee (King's College London) and conducted in accordance with European regulations, and Home Office personal and project licenses under the UK Animals (Scientific Procedures) 1986 Act. Project Licenses: PD025E9BC, PP3627598

Note that full information on the approval of the study protocol must also be provided in the manuscript.

Plants

Seed stocks	*Report on the source of all seed stocks or other plant material used. If applicable, state the seed stock centre and catalogue number. If plant specimens were collected from the field, describe the collection location, date and sampling procedures.*
Novel plant genotypes	*Describe the methods by which all novel plant genotypes were produced. This includes those generated by transgenic approaches, gene editing, chemical/radiation-based mutagenesis and hybridization. For transgenic lines, describe the transformation method, the number of independent lines analyzed and the generation upon which experiments were performed. For gene-edited lines, describe the editor used, the endogenous sequence targeted for editing, the targeting guide RNA sequence (if applicable) and how the editor was applied.*
Authentication	*Describe any authentication procedures for each seed stock used or novel genotype generated. Describe any experiments used to assess the effect of a mutation and, where applicable, how potential secondary effects (e.g. second site T-DNA insertions, mosiacism, off-target gene editing) were examined.*

ChIP-seq

Data deposition

☒ Confirm that both raw and final processed data have been deposited in a public database such as GEO.

☒ Confirm that you have deposited or provided access to graph files (e.g. BED files) for the called peaks.

Data access links *May remain private before publication.*	https://www.ncbi.nlm.nih.gov/geo/query/acc.cgi?acc=GSE285372
Files in database submission	GSM8701404 Fos_SAL_1,ChIP GSM8701405 Fos_SAL_2,ChIP GSM8701406 Fos_SAL_3,ChIP GSM8701407 Fos_KA_1,ChIP GSM8701408 Fos_KA_2,ChIP GSM8701409 Fos_KA_3,ChIP GSM8701410 Fos,Input GSE285372_Fos_KA_merged.bam.RPGC.bw GSE285372_Fos_Saline_merged.bam.RPGC.bw GSE285372_RAW.tar (TAR of BW, NARROWPEAK) GSE158843_Fos/FosB/Jun
Genome browser session (e.g. UCSC)	*Provide a link to an anonymized genome browser session for "Initial submission" and "Revised version" documents only, to enable peer review. Write "no longer applicable" for "Final submission" documents.*

Methodology

Replicates	Vehicle, 3 mice; KA, 3 mice.

Sequencing depth	ChIP-seq samples were sequenced in Illumina HiSeq2500 in a single-end 50 bp length configuration. All samples showed >90% reads with high quality mapping to mm10
Antibodies	Rabbit monoclonal α-Fos (Thermo Scientific T.142.5)
Peak calling parameters	Reads were mapped with Bowtie2 to mm10 genome index. Peak calling was done with MACS2 with default parameters including the input sample.
Data quality	Only peaks with and FDR < 1e-5 were used
Software	Samtools (v1.9), Bedtools (v2.26.0), DeepTools (v3.5.0), Bowtie2 (v2.3.4.3), MACS2 (v2), DiffBind (v3.12), R v4.5, Seurat v5.4.0, scCustomize v3.2.4, SeuratExtend v1.2.1, tidyverse v1.3.0, MAST v1.36.0